# NASA TECHNICAL
# REPORT

# NUMERICAL SOLUTION OF THE EQUATIONS FOR COMPRESSIBLE LAMINAR, TRANSITIONAL, AND TURBULENT BOUNDARY LAYERS AND COMPARISONS WITH EXPERIMENTAL DATA

*by Julius E. Harris*

*Langley Research Center*
*Hampton, Va. 23365*

| 1. Report No. NASA TR R-368 | 2. Government Accession No. | 3. Recipient's Catalog No. |
|---|---|---|
| 4. Title and Subtitle NUMERICAL SOLUTION OF THE EQUATIONS FOR COMPRESSIBLE LAMINAR, TRANSITIONAL, AND TURBULENT BOUNDARY LAYERS AND COMPARISONS WITH EXPERIMENTAL DATA | | 5. Report Date August 1971 |
| | | 6. Performing Organization Code |
| 7. Author(s) Julius E. Harris | | 8. Performing Organization Report No. L-7660 |
| 9. Performing Organization Name and Address NASA Langley Research Center Hampton, Va. 23365 | | 10. Work Unit No. 136-13-01 |
| | | 11. Contract or Grant No. |
| 12. Sponsoring Agency Name and Address National Aeronautics and Space Administration Washington, D.C. 20546 | | 13. Type of Report and Period Covered Technical Report |
| | | 14. Sponsoring Agency Code |

15. Supplementary Notes
    The information presented herein is based in part upon a thesis entitled "Numerical Solution of the Compressible Laminar, Transitional, and Turbulent Boundary Layer Equations With Comparisons to Experimental Data" submitted in partial fulfillment of the requirements for the degree of Doctor of Philosophy in Aerospace Engineering, Virginia Polytechnic Institute and State University, Blacksburg, Virginia, May 1970.

16. Abstract

    A numerical method for solving the equations for laminar, transitional, and turbulent compressible boundary layers for either planar or axisymmetric flows is presented. The fully developed turbulent region is treated by replacing the Reynolds stress terms with an eddy viscosity model. The mean properties of the transitional boundary layer are calculated by multiplying the eddy viscosity by an intermittency function based on the statistical production and growth of the turbulent spots. A specifiable turbulent Prandtl number relates the turbulent flux of heat to the eddy viscosity. A three-point implicit finite-difference scheme is used to solve the system of equations. The momentum and energy equations are solved simultaneously without iteration. Numerous test cases are compared with experimental data for supersonic and hypersonic flows; these cases include flows with both favorable and mildly unfavorable pressure gradient histories, mass flux at the wall, and transverse curvature.

| 17. Key Words (Suggested by Author(s)) Laminar, transitional, and turbulent boundary layers Numerical solution Compressible boundary layers | 18. Distribution Statement Unclassified – Unlimited |
|---|---|

| 19. Security Classif. (of this report) Unclassified | 20. Security Classif. (of this page) Unclassified | 21. No. of Pages 84 | 22. Price* $3.00 |
|---|---|---|---|

# NUMERICAL SOLUTION OF THE EQUATIONS
## FOR COMPRESSIBLE LAMINAR, TRANSITIONAL, AND
## TURBULENT BOUNDARY LAYERS AND COMPARISONS
## WITH EXPERIMENTAL DATA*

By Julius E. Harris
Langley Research Center

## SUMMARY

A numerical method for solving the system of equations which govern the mean flow properties of laminar, transitional, and turbulent compressible boundary layers for either planar or axisymmetric flows is presented. The turbulent boundary layer is treated by a two-layer concept with appropriate eddy viscosity models used for each layer to replace the Reynolds stress term. A specifiable static turbulent Prandtl number relates the turbulent heat flux term to the Reynolds stress. The mean properties in the transitional boundary layer are calculated by multiplying the eddy viscosity by an intermittency function based on the statistical production and growth of the turbulent spots. The numerical method used to solve the system of equations is a three-point implicit finite-difference scheme. The momentum and energy equations are solved simultaneously without iteration.

A number of test cases are compared with experimental data for supersonic and hypersonic flows over planar and axisymmetric geometries. These test cases include laminar, transitional, and turbulent boundary-layer flows with both favorable and unfavorable pressure-gradient histories. Mass flux at the wall and transverse curvature effects are considered. The results show that the system of equations and the numerical technique provide accurate predictions for laminar, transitional, and turbulent compressible boundary-layer flows.

---

# INTRODUCTION

The boundary-layer concept first introduced by Prandtl (ref. 1) in 1904 divides the flow field over an arbitrary surface into two distinct regions; an inviscid outer region in which solutions to the Euler equations describe the flow-field characteristics, and a viscous inner region where the classical boundary-layer equations apply. The boundary-layer region may be further categorized as to type, namely, laminar, transitional, and turbulent.

The laminar boundary layer has received considerable attention over the past 60 years. Reviews of early methods are presented in references 2 to 4. A review of similar and local similarity solutions is presented in reference 5. In the early part of the past decade, the complete nonsimilar laminar equations were solved to a high degree of accuracy by finite-difference techniques. (See Blottner, ref. 6.)

The mean flow within the transition region has not been studied as extensively as either the location of transition or the characteristics of the fully developed turbulent boundary layer. There have been many experimental studies where the heat transfer at the wall was measured, but these studies reveal little of the flow structure away from the wall. A few experimental studies have been made in which the instantaneous behavior of the transitional boundary layer was reported for both incompressible (refs. 7 to 9) and compressible flows (ref. 10) but more detailed work is still required. The available transitional region data, although limited in extent, does allow workable models of the mean flow structure in the transition region to be formulated and applied tentatively to compressible flow systems. These crude models are generally based on the transport models for fully developed turbulent flows modified by some intermittency distribution. Reviews of transition and the transitional region have recently been presented by Săvulescu (ref. 11) and Morkovin (ref. 12). (See, also, ref. 13.)

Compressible turbulent boundary-layer flows have received accelerated study over the past decade. At first most of the work was experimental, the main objective being development of empirical or semiempirical correlation techniques. Little effort was devoted to obtaining numerical solutions of the equations for turbulent boundary layers until a few years ago. The principal difficulties were associated with modeling the turbulent transport terms as well as developing techniques for obtaining solutions on existing digital computer systems. Even today, because of the limited understanding of these turbulent transport processes, completely general solutions of the mean turbulent boundary-layer equations are not possible. However, by modeling the turbulent transport terms through eddy viscosity or mixing-length concepts, it is possible to solve the system of equations directly. Reviews of recent analytical advances are contained in

reference 14 for incompressible flow. (See ref. 15 for compilation of incompressible data.) Similar material for compressible flows is presented in references 16 and 17.

A number of papers have been presented over the past decade in which attempts have been made to connect the three boundary-layer flow regions (laminar, transitional, and turbulent) so that one system of equations could be used to describe compressible boundary-layer flows. Persh (ref. 18) appears to be one of the first to develop reasonably accurate solutions for the transitional region. Persh used an empirical correlation of velocity profile data together with the streamwise momentum equation to predict the characteristics of transitional flow; although limited in application, it did present a method with which the laminar and turbulent regions could be tied together. Weber (ref. 19) used mixing-length theory and an intermittency factor based on the probability equation of Emmons (ref. 20) to calculate velocity profiles which were in fair agreement with existing experimental data. (See also Masaki and Yakura (ref. 21).) Martellucci, Rie, and Sontowski (ref. 22) were among the first to define an effective viscosity model for laminar, transitional, and turbulent compressible boundary-layer flows. (See also, Harris (ref. 23), Adams (ref. 24), and Kuhn (ref. 25)). Fish and McDonald (ref. 26) have developed a solution technique in which the mixing length at each streamwise station is governed by an integral solution of the turbulent kinetic energy equation with the free-stream turbulence intensity used as a boundary condition. The most significant feature of the Fish-McDonald technique is that the transition location and the extent of the transitional flow are not required as inputs to the solution. The method has currently been applied only to incompressible boundary-layer flows. (See also, Glushko (ref. 27) and Donaldson (ref. 28)).

The present paper presents a system of equations that are applicable to laminar, transitional, and turbulent compressible boundary layers and a numerical technique for obtaining accurate solutions of the system for either planar or axisymmetric perfect gas flows. The numerical technique is similar to that first developed by Flügge-Lotz and Blottner (ref. 29) and later improved by Davis and Flügge-Lotz (ref. 30). The momentum and energy equations remain coupled and are solved simultaneously in the transformed plane without iteration. (Difference relations and coefficients for the difference equations are developed in appendixes A and B, respectively.) The procedure is very efficient for parabolic systems where only two governing equations are required; however, as the number of equations increases beyond two, the method becomes increasingly inefficient because of the digital computer storage requirements. (See ref. 6.) The numerical technique yields accurate results for compressible laminar, transitional, and turbulent boundary layers with pressure gradients, heat transfer, and mass transfer at the wall. The method treats the fully developed turbulent region by replacing the Reynolds stress terms with an eddy viscosity model. A specifiable static turbulent Prandtl number function relates the turbulent flux of heat to the eddy viscosity model. The mean

3

properties of the transitional boundary layer are calculated by multiplying the eddy viscosity by an intermittency function based on the statistical production and growth of the turbulent spots. The eddy viscosity model is based upon existing experimental data.

## SYMBOLS

| | |
|---|---|
| A | damping function (eq. (38)) |
| $A_n^{(1)}, B_n^{(1)}, C_n^{(1)},$ $D_n^{(1)}, E_n^{(1)}, F_n^{(1)}, G_n^{(1)}$ | coefficients in difference equation (66) and defined by equations (B3) to (B9) |
| $A_n^{(2)}, B_n^{(2)}, C_n^{(2)},$ $D_n^{(2)}, E_n^{(2)}, F_n^{(2)}, G_n^{(2)}$ | coefficients in difference equation (67) and defined by equations (B10) to (B16) |
| $C_f$ | skin-friction coefficient, $\dfrac{\tau_w}{\left(\frac{1}{2}\rho u^2\right)_e}$ |
| $C_{m1}, C'_{m1}$ | defined in equations (B45) and (B46) |
| $C_p$ | specific heat at constant pressure |
| c | length defined in figure 13(a) |
| $\overline{E}_{m1}, \hat{E}_{m1}$ | defined in equations (B36) and (B37) |
| $\hat{E}_Y$ | defined in equation (B39) |
| F | velocity ratio, $\dfrac{u}{u_e}$ |
| $\tilde{F}$ | mass injection parameter, $\dfrac{(\rho v)_w}{(\rho u)_e}$ |
| $F_{m1}$ | defined in equation (B29) |
| $F_{m2}$ | defined in equation (B32) |
| $F_Y$ | defined in equation (B40) |

4

| G | a typical quantity in boundary layer |
|---|---|
| H | a typical quantity in boundary layer (see appendix A) |
| $H_1, H_2, H_3, \ldots, H_{11}, H_{12}$ | coefficients defined by equations (B17) to (B28) |
| h | heat-transfer coefficient |
| i | index used in grid-point notation (eq. (64)) |
| j | flow index; $j = 0$ planar flow, $j = 1$ axisymmetric flow |
| K | grid-point-spacing parameter (eq. (64)) |
| $K_1$ | constant in eddy viscosity model (eq. (36)) |
| $K_2$ | constant in eddy viscosity model (eq. (41)) |
| $K_l$ | thermal conductivity |
| $K_T$ | eddy conductivity (eq. (9)) |
| L | reference length |
| $L_{m1}, L'_{m1}$ | defined in equations (B34) and (B35) |
| $l$ | defined in equations (28) |
| $\bar{l}$ | mixing length (eq. (36)) |
| M | Mach number |
| m | grid-point index (fig. 7) |
| N | number of grid points at each x-station (fig. 7) |
| $N_{Pr}$ | Prandtl number, $\dfrac{C_p \mu}{K_l}$ |
| $N_{Pr,t}$ | static turbulent Prandtl number (eq. (10)) |

$N_{St}$      Stanton number, $\dfrac{h}{C_p \rho u}$

n      index defined in figure 7

P      coefficient in correlation equation (55)

p      pressure

Q      coefficient in correlation equation (55)

q      heat-transfer rate

R      coefficient in correlation equation (55)

$R_e$      unit Reynolds number, $\dfrac{u_e}{\nu_e}$

$R_{e,x}$      Reynolds number based on x, $\dfrac{u_e x}{\nu_e}$

$R_{e,x_{t,i}}$      Reynolds number at transition, $\dfrac{u_e}{\nu_e} x_{t,i}$

$R_{e,\Delta x_t}$      Reynolds number based on transition extent, $\dfrac{u_e}{\nu_e}\left(x_{t,f} - x_{t,i}\right)$

$R_{e,\delta_t^*}$      transition Reynolds number based on displacement thickness, $\dfrac{u_e}{\nu_e}\delta_t^*$

$R_{e,\theta}$      Reynolds number based on momentum thickness, $\left(\dfrac{u_e}{\nu_e}\right)\theta$

$R_{\infty,d}$      free-stream Reynolds number based on diameter, $\dfrac{u_\infty d}{\nu_\infty}$

r      radial coordinate (fig. 1)

$r_f$      recovery factor (eq. (75))

$r_n$      nose radius

$r_o$      body radius (fig. 1)

S      Sutherland viscosity constant ($198.6^\circ$ R ($110.3^\circ$ K))

T      static temperature

$T_{m1}, T_{m2}$ defined in equations (B30) and (B33)

$T_Y$ defined in equation (B41)

$t$ transverse curvature term (eqs. (21))

$u$ velocity component in x-direction (fig. 1)

$u^+$ law-of-wall coordinate, $\dfrac{u}{u_\tau}$

$u_\tau$ friction velocity, $\sqrt{\tau_w / \rho}$

$V$ transformed normal velocity component (eq. (24))

$V_{m1}$ defined in equation (B31)

$v$ velocity component in y-direction

$\tilde{v}$ velocity component defined by equation (7)

$X_1, X_2, X_3, X_4, X_5$ functions of grid-point spacing defined by equations (A4) to (A8)

$x$ boundary-layer coordinate tangent to surface

$x_{t,f}$ end of transition

$x_{t,i}$ beginning of transition

$Y_1, Y_2, Y_3, Y_4, Y_5, Y_6$ functions of grid-point spacing defined by equations (A12) to (A17)

$Y_7, Y_8, Y_9, Y_{10}$ functions defined by equations (70)

$y$ boundary-layer coordinate normal to surface

$y^+$ law of wall coordinate, $\dfrac{y u_\tau}{\nu}$

$y_m$ defined in figure 4

$Z$ body coordinate (fig. 1)

$\alpha$ defined in equations (28)

$\dot{\beta}$          defined in equations (28)

$\Gamma$          streamwise intermittency distribution (eq. (57))

$\gamma$          ratio of specific heats

$\bar{\gamma}$          transverse intermittency distribution (eq. (44))

$\Delta x$          grid-point spacing in physical plane

$\Delta x_t$          transition extent, $x_{t,f} - x_{t,i}$

$\Delta \xi, \Delta \eta$          grid-point spacing in transformed plane (see fig. 7)

$\delta$          boundary-layer thickness

$\delta^*$          displacement thickness

$\delta^*_{inc}$          incompressible displacement thickness

$\epsilon$          eddy viscosity

$\bar{\epsilon}$          eddy viscosity function defined in equation (15)

$\bar{\epsilon}_{av}$          defined in equation (74)

$\hat{\epsilon}$          eddy viscosity function defined in equation (16)

$\eta$          transformed normal boundary-layer coordinate

$\Theta$          static temperature ratio (eqs. (23))

$\theta$          momentum thickness

$\lambda$          defined in equation (59)

$\mu$          molecular viscosity

$\nu$          kinematic viscosity, $\dfrac{\mu}{\rho}$

8

| | |
|---|---|
| $\bar{\nu}$ | average kinematic viscosity |
| $\xi$ | transformed streamwise boundary-layer coordinate |
| $\bar{\xi}$ | defined in equation (58) |
| $\Pi, \Pi_1, \Pi_2$ | functions defined in equations (48) to (50) |
| $\rho$ | density |
| $\tau$ | shear stress |
| $\phi$ | angle between local tangent to surface and center line of body (see fig. 1) |
| $\chi$ | vorticity Reynolds number (eq. (54)) |
| $\chi_{max}$ | maximum local value of $\chi$ (fig. 5) |
| $(\chi_{max})_{cr}$ | value of $\chi_{max}$ at transition (stability index) |
| $\Omega$ | functional relation (see eq. (62)) |

Subscripts:

| | |
|---|---|
| e | edge value or based on edge conditions |
| i | inner region of turbulent layer |
| m | mesh point in $\xi$-direction (see fig. 7) |
| max | maximum value |
| min | minimum value |
| n | mesh point in $\eta$-direction (see fig. 7) |
| o | outer region of turbulent layer |
| s$l$ | sublayer edge |

| sp | stagnation point |
| --- | --- |
| t | total condition |
| u | uniform or average value |
| w | wall value |
| $\infty$ | free stream |

Superscripts:

| j | flow index |
| --- | --- |
| ' | fluctuating component |
| — | time average value |

Other notation:

| TVC | transverse curvature |
| --- | --- |

A coordinate used as a subscript means partial differential with respect to the coordinate. (See eq. (A1).)

## EQUATIONS FOR THE LAMINAR, TRANSITIONAL, AND TURBULENT COMPRESSIBLE BOUNDARY LAYER

This section presents the governing equations for the compressible boundary layer together with the required boundary conditions. The eddy viscosity and eddy conductivity models used to represent the apparent turbulent shear and heat-flux terms appearing in the mean turbulent boundary-layer equations are discussed.

### Physical Plane

Geometry and notation.- The orthogonal coordinate system is presented in figure 1. The boundary-layer coordinate system is denoted by X and Y which are tangent to and normal to the surface, respectively. The origin of both the boundary-layer coordinate axes system X,Y and the body coordinate axes system Z,R is located at the stagnation point for blunt bodies as shown in figure 1 or at the leading edge for sharp-tipped bodies.

10
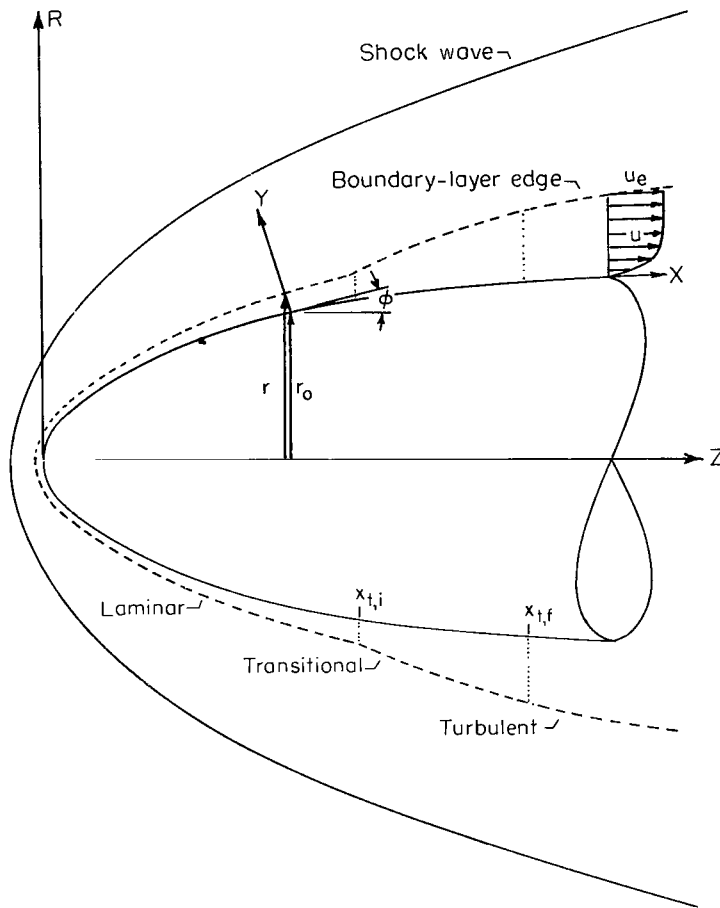
Figure 1.- Coordinate system and notation.

The velocity components  u  and  v  are oriented in the X- and Y-direction, respectively. Transverse curvature terms are retained because of their importance in the development of boundary-layer flows over slender bodies of revolution where the boundary-layer thickness may become of the order of the body radius  $r_0$.  The angle  $\phi$  is the angle between the  Z  axis and local tangent evaluated at (x,0).  The coordinates  $\left(x_{t,i},0\right)$  and  $\left(x_{t,f},0\right)$  represent the location at which transition is initiated and completed, respectively.

Differential equations.- The flow of a compressible, viscous, heat conducting fluid is mathematically described by the continuity, Navier-Stokes, and energy equations together with an equation of state, a heat conductivity law, and a viscosity law.  For flows at large Reynolds number, Prandtl (ref. 1) has shown that the Navier-Stokes and energy equations can be simplified to a form now recognized as the classical boundary-layer equations.  These equations may be written as follows:

Continuity:

$$\frac{\partial}{\partial x}\left(r^j \rho u\right) + \frac{\partial}{\partial y}\left(r^j \rho v\right) = 0 \tag{1}$$

Momentum:

$$\rho\left(u\,\frac{\partial u}{\partial x} + v\,\frac{\partial u}{\partial y}\right) = -\frac{dp}{dx} + \frac{1}{r^j}\frac{\partial}{\partial y}\left[r^j\left(\mu\,\frac{\partial u}{\partial y}\right)\right] \tag{2}$$

Energy:

$$\rho\left[u\,\frac{\partial}{\partial x}(C_p T) + v\,\frac{\partial}{\partial y}(C_p T)\right] = u\,\frac{dp}{dx} + \frac{1}{r^j}\frac{\partial}{\partial y}\left[\frac{r^j K_\ell}{C_p}\frac{\partial}{\partial y}(C_p T)\right] + \mu\left(\frac{\partial u}{\partial y}\right)^2 \tag{3}$$

Osborne Reynolds (ref. 31) in 1883 was the first to observe and study the phenomena of transition from laminar to turbulent flow. Reynolds assumed that the instantaneous fluid velocity satisfied the Navier-Stokes equations and that the instantaneous velocity could be separated into mean and fluctuating components. The result of his early work was a set of Reynolds equations which differed from the Navier-Stokes equations only through the additional terms called the Reynolds stresses. These equations can be reduced through the boundary-layer approximations and written in terms of the mean variables as follows (ref. 32):

Continuity:

$$\frac{\partial}{\partial x}(r^j \rho u) + \frac{\partial}{\partial y}\left[r^j \rho\left(v + \frac{\overline{\rho' v'}}{\rho}\right)\right] = 0 \tag{4}$$

Momentum:

$$\rho\left[u\,\frac{\partial u}{\partial x} + \left(v + \frac{\overline{\rho' v'}}{\rho}\right)\frac{\partial u}{\partial y}\right] = -\frac{dp}{dx} + \frac{1}{r^j}\frac{\partial}{\partial y}\left[r^j\left(\mu\,\frac{\partial u}{\partial y} - \overline{\rho u' v'}\right)\right] \tag{5}$$

Energy:

$$\rho\left[u\,\frac{\partial}{\partial x}(C_p T) + \left(v + \frac{\overline{\rho' v'}}{\rho}\right)\frac{\partial}{\partial y}(C_p T)\right]$$

$$= u\,\frac{dp}{dx} + \frac{1}{r^j}\frac{\partial}{\partial y}\left[r^j\,\frac{K_\ell}{C_p}\frac{\partial}{\partial y}(C_p T)\right] + \mu\left(\frac{\partial u}{\partial y}\right)^2$$

$$+ \frac{1}{r^j}\frac{\partial}{\partial y}\left[r^j\left(-C_p \rho \overline{v' T'}\right)\right] - \rho\overline{u' v'}\,\frac{\partial u}{\partial y} \tag{6}$$

The reduction of the Reynolds equations to the mean turbulent boundary-layer form presented in equations (4), (5), and (6) requires a number of stringent assumptions based on an order-of-magnitude analysis. These assumptions together with the various correlation terms which are neglected are discussed by Van Driest (ref. 32). However, for hypersonic flows where the boundary-layer thickness may increase rapidly and the density gradients are large, the order-of-magnitude analysis as presented in reference 32 may no longer be valid. For example, the Reynolds shear stress term $\overline{(\rho v)'u'}$ yields three correlation products when expanded; namely, $\rho\overline{(u'v')}$, $v\overline{(\rho'u')}$, and $\overline{\rho'u'v'}$. The $v\overline{(\rho'u')}$ and $\overline{\rho'u'v'}$ correlations are generally neglected for supersonic flows since they are of lower order than the $\rho\overline{(u'v')}$ correlation; however, for hypersonic flows these two correlations may be of the same order or larger than the $\rho\overline{(u'v')}$ term and as such should be retained in the governing equations. (See Bushnell and Beckwith (ref. 33).) The term $\overline{(\rho v)'T'}$ appearing in the energy equation (ref. 32) may also be expanded into three correlation terms; namely, $\rho\overline{(v'T')}$, $v\overline{(\rho'T')}$, and $\overline{\rho'v'T'}$. For supersonic flows the correlation terms $v\overline{(\rho'T')}$ and $\overline{\rho'v'T'}$ are of lower order than $\rho\overline{(v'T')}$ and can be neglected; however, for hypersonic flows these terms may again be of equal order and should then be retained in the governing equations. Another correlation term $\frac{\partial}{\partial y}(\rho'v')$ which appears in the static energy equation ( ref. 32) is also neglected. For hypersonic flows this term may be of the same order as the Reynolds stress term retained in equation (5) and should then be retained in the system of equations. The actual effect of neglecting the various correlation terms can only be determined after well-documented, accurate experimental data become available for the hypersonic speed range.

The mean turbulent equations are identical to those for laminar flows with the exception of the correlations of the turbulent fluctuating quantities which represent the apparent mass, shear, and heat-flux terms caused by the turbulence. The major problem encountered in calculating turbulent flows from this set of equations (eqs. (4) to (6)) is how to relate these turbulent correlations to the mean flow and thereby obtain a closed system. In the present analysis, the apparent mass flux term $\overline{\rho'v'}$, the apparent shear stress term, $\overline{\rho u'v'}$ (Reynolds stress term), and the apparent heat flux term $C_p\overline{\rho v'T'}$ are modeled or represented by a new velocity component $\tilde{v}$, an eddy viscosity $\epsilon$, and an eddy conductivity $K_T$, respectively.

A new velocity component normal to the surface is defined as follows:

$$\tilde{v} = v + \frac{\overline{\rho'v'}}{\rho} \tag{7}$$

The eddy viscosity is defined as

$$\epsilon = -\rho \frac{\overline{u'v'}}{\partial u/\partial y} \tag{8}$$

13

and the eddy conductivity as

$$K_T = -C_p \rho \, \frac{\overline{v'T'}}{\partial T / \partial y} \tag{9}$$

The static turbulent Prandtl number is defined as follows:

$$N_{Pr,t} = \frac{\overline{u'v'}}{\overline{v'T'}} \left( \frac{\partial T / \partial y}{\partial u / \partial y} \right) \tag{10}$$

Equation (10) can then be expressed in terms of equations (8) and (9) as

$$N_{Pr,t} = \frac{C_p \epsilon}{K_T} \tag{11}$$

In terms of equations (7) to (11), the governing differential equations (eqs. (4), (5), and (6)) may be written as follows:

Continuity:

$$\frac{\partial}{\partial x} \left( r^j \rho u \right) + \frac{\partial}{\partial y} \left( r^j \rho \tilde{v} \right) = 0 \tag{12}$$

Momentum:

$$\rho \left( u \, \frac{\partial u}{\partial x} + \tilde{v} \, \frac{\partial u}{\partial y} \right) = - \frac{dp}{dx} + \frac{1}{r^j} \frac{\partial}{\partial y} \left( r^j \mu \bar{\epsilon} \, \frac{\partial u}{\partial y} \right) \tag{13}$$

Energy:

$$\rho \left[ u \, \frac{\partial}{\partial x} (C_p T) + \tilde{v} \, \frac{\partial}{\partial y} (C_p T) \right] = u \, \frac{dp}{dx} + \mu \bar{\epsilon} \left( \frac{\partial u}{\partial y} \right)^2 + \frac{1}{r^j} \frac{\partial}{\partial y} \left[ \frac{r^j \mu}{N_{Pr}} \, \hat{\epsilon} \, \frac{\partial}{\partial y} (C_p T) \right] \tag{14}$$

The terms $\bar{\epsilon}$ and $\hat{\epsilon}$ appearing in equations (13) and (14) are respectively defined as follows:

$$\bar{\epsilon} = \left( 1 + \frac{\epsilon}{\mu} \, \Gamma \right) \tag{15}$$

and

$$\hat{\epsilon} = \left( 1 + \frac{\epsilon}{\mu} \, \frac{N_{Pr}}{N_{Pr,t}} \, \Gamma \right) \tag{16}$$

The function $\Gamma$ appearing in equations (15) and (16) represents the streamwise intermittency distribution in the transitional region of the boundary layer; $\Gamma$ is a function only of the x-coordinate and is discussed in detail subsequently.

In order to complete the system of equations, the perfect gas law and Sutherland's viscosity relation are introduced:

14

Gas law:

$$p = C_p \frac{\gamma - 1}{\gamma} \rho T \qquad (17)$$

Viscosity law:

$$\frac{\mu}{\mu_e} = \left(\frac{T}{T_e}\right)^{3/2} \frac{T_e + S}{T + S} \qquad \text{(Air only)} \qquad (18)$$

It should be noted that any viscosity relationship can be directly incorporated into the solution technique and that the system is not restricted to perfect-air ($\gamma = 1.4$) boundary-layer flows.

The system of governing equations then consists of three nonlinear partial differential equations and two algebraic relations. Two of these differential equations (eqs. (13) and (14)) are second order and the remaining differential equation (eq. (12)) is first order. Consequently, if suitable relations for $\epsilon$, $N_{Pr,t}$, and $\Gamma$ can be specified, there are five unknowns, namely, $u$, $\tilde{v}$, $\rho$, $T$, and $\mu$ and five equations.

The pressure-gradient term appearing in equations (13) and (14) can be replaced by the Bernoulli relation; namely,

$$\frac{dp}{dx} = -\rho_e u_e \frac{du_e}{dx} \qquad (19)$$

which is determined from an inviscid solution. If variable entropy is considered, $dp/dx$ is retained in equations (13) and (14). (See ref. 23.)

Boundary conditions.- In order to obtain a unique solution to the system of governing equations, it is necessary to satisfy the particular boundary conditions of the problem under consideration. These conditions are shown schematically in figure 2. (Note that the outer edge conditions $u_e(x)$ and $T_e(x)$ are related through the energy equation
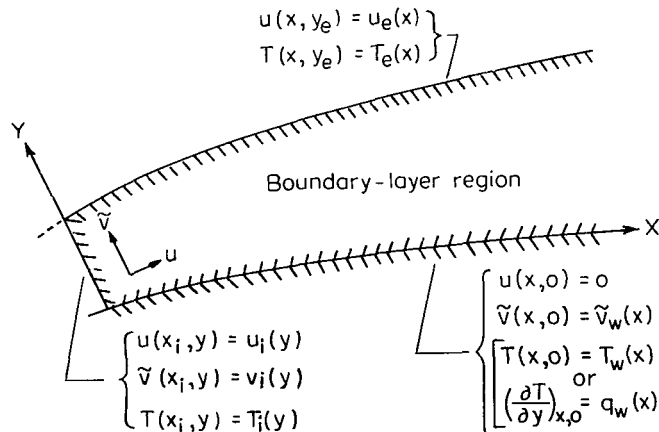


Figure 2.- Boundary conditions in the physical plane.

$T_{t,e} = T_e + u_e^2/2C_p$, where $T_{t,e}$ is constant. The velocity and temperature distribution at the edge of the boundary layer are determined from the shape of the body by using inviscid flow theory. The no-slip condition is imposed at the wall; however, arbitrary distributions of $\tilde{v}_w$ and $T_w$ or $q_w$ may be specified.

The parabolic nature of equations (13) and (14) requires that the initial velocity and temperature profiles be specified at $x_i$. These initial profiles are obtained in the present investigation from an exact numerical solution of the similar boundary-layer equations for laminar flow (eqs. (B47) to (B49)).

<center>Transformed Plane</center>

The system of governing equations is singular at $x = 0$. The Probstein-Elliott (ref. 34) and Levy-Lees (ref. 35) transformation is utilized to remove this singularity as well as to reduce the growth of the boundary layer as the solution proceeds downstream. This transformation can be written as follows:

$$\xi(x) = \int_0^x \rho_e u_e \mu_e r_o^{2j}\, dx \tag{20a}$$

$$\eta(x,y) = \frac{\rho_e u_e r_o^j}{\sqrt{2\xi}} \int_0^y t^j \frac{\rho}{\rho_e}\, dy \tag{20b}$$

where the parameter $t$ appearing in equation (20b) is the transverse curvature term and is defined as

$$t = 1 + \frac{r}{r_o} \tag{21a}$$

or in terms of the y-coordinate as

$$t = 1 + \frac{y}{r_o} \cos \phi \tag{21b}$$

The relation between derivatives in the physical (x,y) and transformed $(\xi,\eta)$ coordinate systems is as follows:

$$\left.\begin{aligned} \left(\frac{\partial}{\partial x}\right)_y &= \rho_e u_e \mu_e r_o^{2j}\left(\frac{\partial}{\partial \xi}\right)_\eta + \left(\frac{\partial \eta}{\partial x}\right)\left(\frac{\partial}{\partial \eta}\right)_\xi \\[2ex] \left(\frac{\partial}{\partial y}\right)_x &= \frac{\rho_e u_e r_o^j t^j}{\sqrt{2\xi}}\left(\frac{\rho}{\rho_e}\right)\left(\frac{\partial}{\partial \eta}\right)_\xi \end{aligned}\right\} \tag{22}$$

Two new parameters $F$ and $\Theta$ are introduced and are defined as

$$\left.\begin{aligned} F &= \frac{u}{u_e} \\ \Theta &= \frac{T}{T_e} \end{aligned}\right\} \tag{23}$$

as well as a transformed normal velocity

$$V = \frac{2\xi}{\rho_e u_e \mu_e r_o^{2j}}\left(F\,\frac{\partial \eta}{\partial x} + \frac{\rho \tilde{v} r_o^j t^j}{\sqrt{2\xi}}\right) \tag{24}$$

The governing equations in the transformed plane can then be expressed as follows:

Continuity:

$$\frac{\partial V}{\partial \eta} + 2\xi\,\frac{\partial F}{\partial \xi} + F = 0 \tag{25}$$

Momentum:

$$2\xi F\,\frac{\partial F}{\partial \xi} + V\,\frac{\partial F}{\partial \eta} - \frac{\partial}{\partial \eta}\left(t^{2j} l\bar{\epsilon}\,\frac{\partial F}{\partial \eta}\right) + \beta\left(F^2 - \Theta\right) = 0 \tag{26}$$

Energy:

$$2\xi F\,\frac{\partial \Theta}{\partial \xi} + V\,\frac{\partial \Theta}{\partial \eta} - \frac{\partial}{\partial \eta}\left(t^{2j}\,\frac{l}{N_{Pr}}\,\hat{\epsilon}\,\frac{\partial \Theta}{\partial \eta}\right) - \alpha l t^{2j}\bar{\epsilon}\left(\frac{\partial F}{\partial \eta}\right)^2 = 0 \tag{27}$$

where

$$\left.\begin{aligned} l &= \frac{\rho\mu}{(\rho\mu)_e} \\ \alpha &= \frac{u_e^2}{C_p T_e} \\ \beta &= \frac{2\xi}{u_e}\,\frac{du_e}{d\xi} \end{aligned}\right\} \tag{28}$$

The parameter $l$ can be written by using the viscosity relation (eq. (18)) and the equation of state (eq. (17)) as

$$l = \sqrt{\Theta}\left(\frac{1 + \bar{S}}{\Theta + \bar{S}}\right) \tag{29}$$

(for air only) where $\bar{S} = S/T_e$.

The transverse curvature term can be expressed in terms of the transformed variables as

$$t = \pm \left( 1 + \frac{2\sqrt{2\xi}\,\cos\,\phi}{\rho_e u_e} \int_0^\eta \frac{\rho_e}{\rho}\,d\eta \right)^{1/2} \tag{30}$$

The physical coordinate normal to the wall is obtained from the inverse transformation; namely,

$$y = \frac{r_0}{\cos\,\phi} \left[ -1 \pm \left( \frac{1 + 2\sqrt{2\xi}\,\cos\,\phi}{\rho_e u_e r_0^{2j}} \int_0^\eta \Theta\,d\eta \right)^{1/2} \right] \tag{31}$$

The positive sign is used in equations (30) and (31) for axisymmetric flow over bodies of revolution and the negative sign is used for flows inside axisymmetric ducts (nozzles).

The boundary conditions in the transformed plane are as follows:

Wall boundary:

$$\left. \begin{aligned} F(\xi,0) &= 0 \\ V(\xi,0) &= V_w(\xi) \\ \Theta(\xi,0) &= \Theta_w(\xi) \\[2ex] \left(\frac{\partial\theta}{\partial\eta}\right)_{\xi,0} &= \left(\frac{\partial\theta}{\partial\eta}\right)_w (\xi) \end{aligned} \right\} \tag{32a}$$

or

Edge conditions:

$$\left. \begin{aligned} F\big(\xi,\eta_e\big) &= 1 \\ \Theta\big(\xi,\eta_e\big) &= 1 \end{aligned} \right\} \tag{32b}$$

The boundary condition at the wall for the transformed V-component can be related to the physical plane as

$$V_w = \frac{\sqrt{2\xi}}{\mu_e r_0^j} \frac{\rho_w \tilde{v}_w}{\rho_e u_e} \tag{33}$$

where the no-slip constraint has been imposed on equation (24). Note that the apparent mass flux term appearing in equations (4) to (6) is zero at the wall and that $\tilde{v}_w = v_w$. Therefore, equation (33) can be expressed in terms of the mass flux at the wall as

$$V_w = \frac{\sqrt{2\xi}}{\mu_e r_0^j} \frac{\rho_w v_w}{\rho_e u_e} \tag{34}$$

18

The turbulent boundary layer is treated as a composite layer consisting of an inner and outer region as shown schematically in figure 3. (See Bradshaw, ref. 36.)
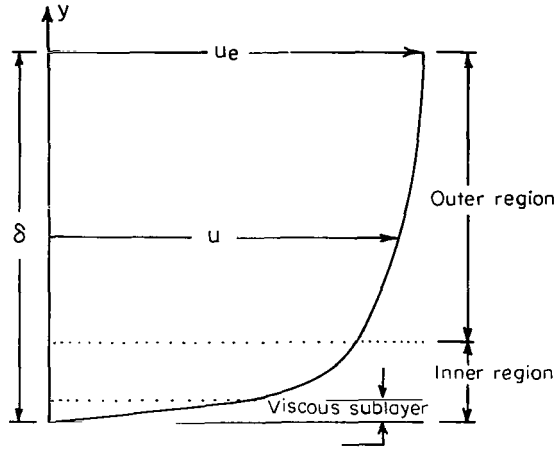


Figure 3.- Two-layer turbulent boundary-layer model.

Inner region model.- The eddy viscosity model used for the inner region is based on the mixing-length hypothesis as developed by Prandtl (ref. 37) in 1925. The eddy viscosity for this region referenced to the molecular viscosity may be expressed as follows:

$$\left(\frac{\epsilon}{\mu}\right)_i = \frac{\rho \bar{l}^2}{\mu}\left|\frac{\partial u}{\partial y}\right| \tag{35}$$

where $\bar{l}$, the mixing length, may be written as

$$\bar{l} = K_1 y \tag{36}$$

The value of $K_1$ has been obtained experimentally and has a value of approximately 0.4, the value which will be used in the present analysis. However, Van Driest (ref. 38) concluded from an analysis based upon experimental data and the second problem of Stokes (ref. 39) that the correct form for the mixing length in the viscous sublayer should be as follows:

$$\bar{l} = K_1 y \left[1 - \exp\left(-\frac{y}{A}\right)\right] \tag{37}$$

where the exponential term is due to the damping effect of the wall on the turbulent fluctuations. The parameter $A$ is usually referred to as the damping constant. The exponential term approaches zero at the outer edge of the viscous sublayer so that the law-of-the-wall region equation, as expressed in equation (36), is valid. The damping constant $A$ is a strong function of the wall boundary conditions and is defined as

$$A = 26\nu\left(\frac{\tau_w}{\rho}\right)^{-1/2} \tag{38}$$

Equation (38) was originally obtained for incompressible, zero-pressure-gradient, solid-wall flow; that is, $\rho$ = Constant, dp/dx = 0, and $\tilde{v}_w$ = 0. The relation has, however, been applied to compressible flows where $\rho$ and $\nu$ are evaluated locally across the sublayer. In the analysis the mixing length is defined as follows:

$$\bar{l} = K_1 y\left\{1 - \exp\left[-\left(\frac{\nu_w}{\bar{\nu}}\right)^{1/2}\frac{y}{A}\right]\right\} \tag{39}$$

where $\bar{\nu}$ is the average value of the kinematic viscosity taken over the viscous sublayer;
$$\bar{\nu} = \sum_{i=1}^{N_{sl}}\nu_i.$$ The density and viscosity appearing in equation (38) are evaluated locally in the present paper; however, these quantities may be evaluated at the local wall boundary conditions if desired. Recent work at the Langley Research Center (ref. 40) has indicated that for hypersonic flow, the density and viscosity should be evaluated at the local wall boundary conditions. The eddy viscosity for the inner region referenced to the molecular viscosity can then be written as follows:

$$\left(\frac{\epsilon}{\mu}\right)_i = \frac{\rho K_1^2 y^2}{\mu}\left[1 - \exp\left(-\sqrt{\frac{\nu_w}{\bar{\nu}}}\frac{y}{A}\right)\right]^2\left|\frac{\partial u}{\partial y}\right| \tag{40}$$

where $A$ is defined in equation (38). Cebeci (ref. 41) has recently attempted to account for the effects of both pressure gradient and wall mass flux on the damping constant. The reader interested in a discussion of this work is referred to the papers by Cebeci (ref. 41) and Harris (ref. 23).

Outer region model.- The eddy viscosity in the outer region is based upon the Clauser (ref. 42) model. The ratio of the eddy viscosity to the molecular viscosity in the outer region can be expressed as follows:

$$\left(\frac{\epsilon}{\mu}\right)_o = K_2\frac{\rho u_e}{\mu}\delta_{inc}^* \tag{41}$$

where $\delta_{inc}^*$ is the incompressible displacement thickness;

$$\delta_{inc}^* = \int_0^{y_e}(1 - F)\,dy \tag{42}$$

The use of $\delta_{inc}^*$ as the scaling parameter for the mixing length is discussed by Maise and McDonald (ref. 43). (See also Morkovin (ref. 44).) The value of $K_2$ in equation (41)

20

is taken to be 0.0168 as reported in reference 45. However, in order to account for the intermittent character of the outer layer flow, equation (41) is modified by an intermittency factor obtained by Klebanoff (ref. 46); that is,

$$\left(\frac{\epsilon}{\mu}\right)_o = K_2 \frac{\rho u_e}{\mu} \delta^*_{inc} \bar{\gamma} \qquad (43)$$

where the transverse intermittency factor $\bar{\gamma}(y)$ is defined as

$$\bar{\gamma} = \frac{1 - erf\left[5\left(\frac{y}{\delta} - 0.78\right)\right]}{2} \qquad (44)$$

The boundary-layer thickness $\delta$ appearing in equation (44) is defined as the distance normal to the wall boundary where $F = 0.995$.

Matching procedure.- The criteria used to determine the boundary between the inner and outer regions is the continuity of eddy viscosity. A sketch of a typical eddy viscosity distribution is presented in figure 4.
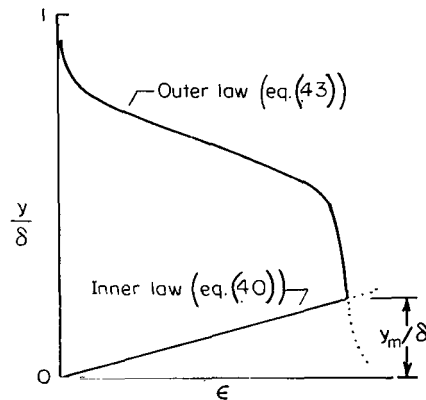


Figure 4.- Matching procedure for two-layer model.

The matching procedure may then be formally written as follows:

$$\left.\begin{array}{ll}
\left(\frac{\epsilon}{\mu}\right)_i = \frac{\rho K_1^2 y^2}{\mu}\left\{1 - \exp\left[-\left(\frac{\nu_w}{\bar{\nu}}\right)^{1/2}\frac{y}{A}\right]\right\}^2 \left|\frac{\partial u}{\partial y}\right| & (0 \leqq y \leqq y_m) \\[2em]
\left(\frac{\epsilon}{\mu}\right)_o = \frac{\rho K_2 u_e}{\mu} \delta^*_{inc} \bar{\gamma} & (y > y_m)
\end{array}\right\} \qquad (45)$$

The location of the boundary separating the two regions $y_m$ is determined from the continuity of equations (45); that is, where

$$\left(\frac{\epsilon}{\mu}\right)_o = \left(\frac{\epsilon}{\mu}\right)_i \tag{46}$$

Eddy conductivity.- The eddy conductivity is formulated in terms of a static turbulent Prandtl number $N_{Pr,t}$ and the eddy viscosity $\epsilon$. (See eqs. (9) to (11).) The two-layer concept for the eddy viscosity model suggests that there should also be a two-layer model for the static turbulent Prandtl number. Numerous assumptions have been made over the past years concerning the eddy conductivity, and corresponding models have been proposed to attempt to predict the mean turbulent boundary-layer temperature profiles. One of the earliest assumptions that has been used extensively is that the static turbulent Prandtl number is a constant equal to unity and implies that the heat and momentum are transferred by the same process. However, the data which are available, although often inclusive, definitely show that $N_{Pr,t}$ is a function of $y/\delta$ for both incompressible and compressible flows. Consequently, the assumption of $N_{Pr,t} = 1$ would be expected to lead to error in predicting the temperature profiles for the turbulent boundary layer.

The incompressible data which are available for the outer region of pipe flow (ref. 47) and boundary layers (ref. 48) indicate that $N_{Pr,t}$ ranges between 0.7 and 0.9. These data indicate that as the wall is approached, $N_{Pr,t}$ achieves a maximum value near the wall and then decreases rapidly to a value between 0.5 to 0.7 at the wall. (See also ref. 49.) Simpson, Whitten, and Moffat (ref. 50) found that $N_{Pr,t}$ ranged from approximately 0.95 at $(y/\delta) \approx 0.1$ to 0.45 at $(y/\delta) = 1.0$. The data in this region were predicted well by the expression $N_{Pr,t} = 0.95\left[1 - 0.5(y/\delta)^2\right]$ as proposed by Rotta (ref. 51). Cebeci (ref. 52) presents a continuous expression for the eddy conductivity which accounts for pressure gradient and mass transfer at the wall boundary. The resulting $N_{Pr,t}$ distribution appears to agree with both the experimental data of Simpson, Whitten, and Moffat (ref. 50) as well as with the Jenkins model (ref. 53). For compressible flows, where very little data are available, it appears that $N_{Pr,t}$ has a value near unity in the outer region of the boundary layer and a value between 0.7 and 0.9 at the wall boundary (ref. 49). Rotta (ref. 51) found that $N_{Pr,t}$ may reach values as high as 2.0 as the wall is approached before decreasing rapidly to the wall boundary value. Meier and Rotta (ref. 54) found for $1.75 \leqq M_\infty \leqq 4.5$ that $N_{Pr,t}$ increased above unity for $y^+ < 50$ and ranged between 0.8 and 0.85 as the outer edge of the boundary layer was approached.

The eddy conductivity and resulting static turbulent Prandtl number model must of necessity at the present time be formulated in terms of existing experimental data. The assessment of the value of the current empirical models must be based upon the agreement between experimental and calculated temperature profiles over a wide range of flow variables. The inconclusiveness of much of the experimental data which exist to date for

both subsonic and supersonic flows and the lack of data for hypersonic flows clearly indicates the severe need for accurate, well-documented experimental temperature and velocity profile data. In the present analysis, since the cases considered deal specifically with either wall gradient values or velocity profile parameters, a constant $N_{Pr,t}$ equal to 0.9 is utilized. However, the numerical procedure utilized is completely general and any function $N_{Pr,t}(y/\delta)$ could be used.

Reynolds number effects.- The eddy viscosity model as presented in the previous sections has implied that $K_1$, $K_2$, and $A^+$ $\left(A^+ = Au_{\tau,w}/\nu_w\right)$ are constants (see eqs. (45)) and therefore independent of flow conditions. However, recent studies have shown that $K_1$, $K_2$, and $A^+$ are strong functions of $R_{e,\theta}$ for moderate to low Reynolds numbers; for example, $R_{e,\theta} < 5000$. (See refs. 52 and 55.) Cebeci (ref. 52) has found that a $K_1$ value of 0.4, as used in the present analysis, is accurate and reliable in predicting the velocity profiles in the law-of-the-wall region provided that $R_{e,\theta} > 6000$. Cebeci, using the data of Simpson (ref. 56), generated polynomial curves for $K_1$ and $A^+$ as functions of $R_{e,\theta}$. These functions were then used to obtain predictions for the data of Whitten (ref. 57) which were in very good agreement in the law-of-the-wall region for $1200 \leqq R_{e,\theta} \leqq 4100$. McDonald (ref. 55) has shown that $K_2$ is a strong function of Reynolds number for $R_{e,\theta} < 5000$; that is, $K_2$ ranges from a value near that used in the present analysis for $R_{e,\theta} > 5000$ to values as large as 0.036 for $R_{e,\theta} = 450$.

For all the cases presented in the present paper, $K_1$, $K_2$, and $A^+$ are held constant and equal to 0.4, 0.0168, and 26, respectively, since low $R_{e,\theta}$ cases are not considered. However, the flexibility of the numerical technique allows any desired variation of these variables to be easily incorporated into the solution.

Transformed models.- Since the governing equations are solved in the transformed plane, it is necessary to transform the eddy viscosity relations from the real plane to the transformed plane.

In the inner region the ratio of eddy viscosity to molecular viscosity is as follows:

$$\left(\frac{\epsilon}{\mu}\right)_i = \frac{\rho_e^2 u_e^2 K_1^2 r_o^j}{\mu_e \sqrt{2\xi}} t^j \frac{y^2 \Pi^2}{l \Theta^3} \left| \frac{\partial F}{\partial \eta} \right| \tag{47}$$

where $y$ is defined by equation (31). The parameter $\Pi$ appearing in equation (47) is the damping term and is defined as

$$\Pi = 1 - \exp\left(-\Pi_1 \Pi_2\right) \tag{48}$$

where

$$\Pi_1 = \frac{\Theta_w}{\overline{\Theta}} \sqrt{\frac{l_w}{l}} \tag{49}$$

23

and

$$\Pi_2 = \frac{y\rho_e u_e}{26 l \Theta^2 \mu_e} \left[ \Theta \frac{\mu_e r_o^j l w}{\sqrt{2\xi}} \left( \frac{\partial F}{\partial \eta} \right)_w \right]^{1/2} \tag{50}$$

In the outer region the ratio of eddy viscosity to molecular viscosity is as follows:

$$\left( \frac{\epsilon}{\mu} \right)_o = \frac{\rho_e u_e}{\mu_e} \, K_2 \, \frac{\overline{\gamma} \delta_{inc}^*}{l \Theta^2} \tag{51}$$

where

$$\overline{\gamma} = \frac{1 - \mathrm{erf} \, 5 \left( \dfrac{y}{y_e} - 0.78 \right)}{2} \tag{52}$$

and

$$\delta_{inc}^* = \frac{\sqrt{2\xi}}{\rho_e u_e r_o^j} \int_0^{\eta_e} t^{-j} \Theta (1 - F) \, d\eta \tag{53}$$

### Transition Region

Equations (25), (26), (27), and (29) together with the boundary conditions (eqs. (32)), and the eddy viscosity relations defined by equations (47) and (51) complete the required system for either laminar or fully developed turbulent boundary-layer flows. However, the main objective is to present a technique that will efficiently solve the laminar, transitional, or turbulent boundary-layer equations as the boundary layer develops along the surface. Consequently, the location of transition $x_{t,i}$, the extent of the transitional flow $x_{t,f} - x_{t,i}$, and the characteristics of the mean flow structure in the transition region must be taken into consideration.

Stability and transition.- Stability theory cannot currently be used to predict either the nonlinear details of the transition process after the two-dimensional waves have been amplified or the location of transition $x_{t,i}$. Stability theory can, however, establish the unstable boundary-layer profiles and the initial amplification rates. The theory can identify those frequencies which will be amplified at the greatest rate as well as the effect on stability of various flow parameters. (See refs. 2, 58, and 59.) A review of methods used to predict the location of transition from stability theory is presented by Jaffe, Okamura, and Smith in reference 60. However, the connection, if any, between stability and transition has not yet been established.

Transition location.- Many parameters influence the location of transition. These parameters can best be thought of as forming a parameter phase space. Such a parameter phase space would include Reynolds number, Mach number, unit Reynolds number,

24

surface roughness, nose bluntness, pressure gradients, boundary conditions at the wall, angle of attack, free-stream turbulence level, and radiated aerodynamic noise. Morkovin (ref. 12) recently completed a very extensive and thorough examination of the current state of the art of transition from laminar to turbulent shear layers. The most striking conclusion that one obtains from the review is that although a great bulk of experimental data on transition currently exists, much of the information on high-speed transition has not been documented in sufficient detail to allow the separation of the effects of these multiple parameters on transition. A discussion of the effects of each of the parameters that may influence transition in high-speed flow is beyond the scope of the present paper.

The reader interested in a detailed discussion is directed to the paper by Morkovin (ref. 12) where over 300 related references are cited and discussed. Another, although less detailed discussion, is presented by Fischer (ref. 61). The effects of radiated aerodynamic noise on transition are discussed by Pate and Schueler (ref. 62). Hypersonic transition, to name but a few references, is discussed by Softley, Graber, and Zempel (ref. 63), Richards (ref. 64), Potter and Whitfield (ref. 65), and Deem and Murphy (ref. 66). A discussion on the effects of extreme surface cooling on hypersonic flat-plate transition is presented by Cary (ref. 67). The effects of nose bluntness and surface roughness on boundary-layer transition are discussed by Potter and Whitfield (ref. 68). In the present analysis the location of transition will be determined by one of, or a combination of, the following three methods. These methods are (1) use of a stability index or vorticity Reynolds number first proposed by Rouse (ref. 69), (2) use of correlations based upon a collection of experimental data over a broad range of test conditions, and (3) use of the measured experimental location of transition as a direct input into the analytical solution.

Stability index.- Hunter Rouse (ref. 69) nearly 25 years ago obtained by dimensional analysis a stability index expressed as follows:

$$\chi = \frac{y^2}{\nu} \frac{\partial u}{\partial y} \tag{54}$$

This index has the form of a vorticity Reynolds number which is obtained from the ratio of the local inertial stress $\rho y^2 (\partial u/\partial y)^2$ to the local viscous stress $\mu(\partial u/\partial y)$. Rouse assumed that for transition to occur the stability index should reach some limiting value which was assumed to be invariant. He was able to show further that this invariant value $(\chi_{max})_{cr}$ should be on the order of 500 for incompressible flows.

The use of $\chi_{max}$ as a stability index is in principle similar to the basic reasoning which led Osborne Reynolds (ref. 31) to postulate that the nondimensional parameter $ud/\nu$ could be used to define a critical value $(ud/\nu)_{cr}$ at which transition would occur in a

circular pipe of diameter d. Unfortunately, $(\chi_{max})_{cr}$ is a function of the transition parameter phase space in much the same fashion as the critical Reynolds number and cannot in reality be a true invariant for transition as suggested by Rouse. The stability index does, however, possess a number of important characteristics which can be directly related to the stability of laminar flows.

A schematic distribution of $\chi$ for a compressible laminar boundary layer is presented in figure 5. The vorticity Reynolds number has a value of zero at the wall and approaches zero as the outer edge of the layer is approached. The maximum value of $\chi$, that is, $\chi_{max}$, occurs at some transverse location $(y/\delta)_{\chi_{max}}$. The values of $\chi_{max}$ and $(y/\delta)_{\chi_{max}}$ are of importance in the use of the vorticity Reynolds number as a guide to boundary-layer stability and transition.

As the laminar boundary layer develops over a surface, $\chi_{max}$ increases monotonically until the critical value $(\chi_{max})_{cr}$ is reached at which point transition is assumed to occur; that is, the location of $x_{t,i}$. For compressible flows $(\chi_{max})_{cr}$ is not an invariant. In the present study $(\chi_{max})_{cr}$ ranged from approximately 2100 to values on the order of 4000. The variation $(\chi_{max})_{cr}$ is a strong function of unit Reynolds number for data obtained in air wind-tunnel facilities. However, although not invariant, the stability index does exhibit the same dependence on various parameters that is predicted by the more complicated stability theory. For example, at a given streamwise location x, the value of $\chi_{max}$ for supersonic flow is found to decrease (which implies a more stable flow) with wall cooling, wall suction, and favorable pressure gradients, whereas it increases (which implies a more unstable flow) with wall heating, mass injection (transpiration), and adverse pressure gradients. The vorticity Reynolds number $\chi_{max}$ appears to have been used as a correlation parameter in only two boundary-layer transition studies. A modified form of the parameter was used to
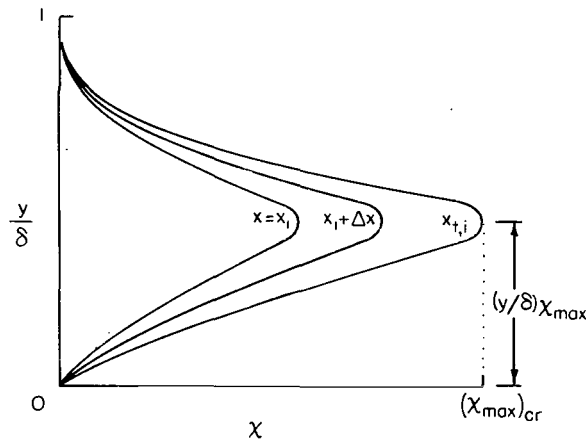


Figure 5.- Vorticity Reynolds number.

correlate the effect of free-stream turbulence on transition by Van Driest and Blumer (ref. 70). Correlation attempts, using Rouse's original invariant assumptions, were made by Ivensen and Hsu (ref. 71); however, the results were only fair.

One of the most important characteristics of the vorticity Reynolds number is that the value of $(y/\delta)_{\chi_{max}}$ is in excellent agreement with the experimental location of the critical layer which represents the distance normal to the wall where laminar flow breakdown will occur. Stainback (ref. 72) computed the Rouse stability index for similar laminar-boundary-layer flows over a broad range of ratios of wall temperature to total temperature for Mach numbers up to 16. The numerical calculations were made for both air and helium boundary layers. The agreement between $(y/\delta)_{\chi_{max}}$ and the experimental critical layer position was excellent over the entire range.

Empirical correlations.- In most instances one has to rely on empirical correlations of experimental transition data in order to fix the most probable transition location for a design configuration. However, caution should always be used when obtaining the most probable location of transition from such correlations, since any given correlation is based upon a specific collection of data which will not be completely general. There currently exists a number of empirical correlations for predicting the probable location of transition. Some of these correlations are of questionable value; however, some can be used with confidence providing it is realized that one is predicting a probable range of locations and not an exact fixed point. One of the more successful correlations (unpublished) was obtained by Stainback and Beckwith for sharp cones at zero angle of attack. The correlation is based on experimental transition data obtained over a wide range of test conditions in air wind tunnels, ballistic ranges, and free flight. The correlation can be expressed as follows:

$$\log_{10}\left(\frac{R_{e,\delta_t^*}}{R_{e,d}^R}\right) = P + QM_e(\Theta_w)^{0.7\exp\left(-0.05M_e^2\right)} \tag{55}$$

where $R_{e,d}$ and $R_{e,\delta_t^*}$ are the Reynolds numbers based on base diameter $d$ and the displacement thickness at transition, respectively. The constants $P$, $Q$, and $R$ are functions of the environment in which transition was measured and are given in the following table:

| Facility | P | Q | R |
|---|---|---|---|
| Air wind tunnel | 1.6217 | 0.11708 | 0.25 |
| Ballistic range | 2.2082 | .14047 | .15 |
| Free flight | 1.2683 | .10441 | .325 |

Equation (55) can be expressed in terms of the transition Reynolds number $R_{e,x_{t,i}}$ as follows:

$$R_{e,x_{t,i}} = \frac{3}{2} \frac{R_{e,d}^{2R}}{l_w} \frac{10\left[2P + 2QM_e(\Theta_w)^{0.7\exp\left(-0.05M_e^2\right)}\right]}{\left(0.094M_e^2 + 1.22\Theta_w\right)^2} \tag{56}$$

Equations (55) and (56) are similar to the relations presented by Bertram and Beckwith (ref. 73); however, the constants P, Q, and R presented in the preceding table are somewhat different from those of reference 73.

Experimental transition.- Much of the confusion that exists in the literature concerning boundary-layer transition may be attributed to the following two factors. The first factor is that in many instances the investigator who made the experimental study may not have carefully measured or recorded the complete conditions under which the data were obtained. The second factor is that the experimentally observed transition location depends on the experimental technique used.

The importance of carefully measuring the environment under which the experiments are made cannot be overstressed. In the past, many of the factors which influence transition such as free-stream turbulence and acoustic radiation from the tunnel sidewall boundary layer were not measured. (See refs. 73 to 76.) The location of transition as obtained experimentally is a function of the method used to determine its location. There are currently a number of techniques used to obtain the transition location. Some of these methods are hot-wire traverses, pitot-tube surveys near the wall, visual indication from schlieren photographs, and heat-transfer measurements at the wall. Each of these methods basically measures a different flow process. Consequently, it would be misleading to believe that each technique would yield the same location for transition if simultaneously applied to the same boundary layer. Of course, the concept of a transition "point" is misleading in itself since transition does not occur at a "point" but instead over some finite region.

For the test cases presented herein, the transition location $x_{t,i}$ will be determined from heat-transfer measurements at the wall whenever possible. The reason for this choice is that it is the method most often used in the literature. However, it should be noted that the actual nonlinear transition process begins somewhat upstream of the location where the heat transfer at the wall deviates from the laminar trend.

Transitional flow structure.- Once the transition location has been fixed for a given problem, one must next consider the following two important factors; first, the length of the transition region, $x_{t,f} - x_{t,i}$ (sometimes referred to as transition extent), and secondly, the mean flow characteristics within the region. Once appropriate models are

obtained for these two factors, it is possible to connect the three flow regions smoothly so that one set of governing equations may be used.

The laminar boundary-layer equations (eqs. (1) to (3)) should yield accurate profiles and wall boundary gradients in the region prior to turbulent spot formation. The intermittent appearance of the turbulent spots and the process of cross-contamination are not well understood. The spots originate in a more or less random fashion and merge with one another as they grow and move downstream. Eventually, the entire layer is contaminated which marks the end of the transition process $x_{t,f}$. As the turbulent spots move over a fixed point in the transition region, the point experiences an alternation between fully laminar flow when no spot is present and turbulent flow when engulfed by a spot. These alternations can be described by an intermittency factor which represents the fraction of time that any point in the transition region is engulfed by turbulent flow.

The distribution of spots in time and space is Gaussian for low-speed natural transition. However, very little is known about the spot distribution in high-speed compressible flow. Furthermore, there is no assurance that the spot formation and distribution in hypersonic flows will be analogous to the low-speed model; however, in the absence of a more satisfactory theory, the approach of Dhawan and Narasimha (ref. 77) is used. In reference 77 the source density function of Emmons (ref. 20) was used to formulate the probability distribution (intermittency) of the turbulent spots as follows:

$$\Gamma(\bar{\xi}) = 1 - \exp\left(-0.412\bar{\xi}^2\right) \tag{57}$$

where

$$\bar{\xi} = \frac{x - x_{t,i}}{\lambda} \tag{58}$$

for $x_{t,i} \leq x \leq x_{t,f}$. The term $\bar{\xi}$ in equation (57) represents a normalized streamwise coordinate in the transition region, and $\lambda$ is a measure of the extent of the transition region; that is,

$$\lambda = (x)_{\Gamma=3/4} - (x)_{\Gamma=1/4} \tag{59}$$

The intermittency distributions in the transverse direction (y-direction) are similar to those observed by Corrsin and Kistler (ref. 78) for fully developed turbulent boundary layers (ref. 79). Corrsin and Kistler found that the transverse intermittency varied from a maximum of unity near the wall to a near-zero value at the outer edge of the layer. The transverse intermittency distribution is of secondary importance in relation to the streamwise distribution in determining the mean profiles and wall fluxes; consequently, the only intermittency distribution applied in the transverse direction (y-direction) is that of Klebanoff (ref. 46) in the outer layer as applied to the fully developed turbulent layer. (See eq. (44).) It should be carefully noted in order to avoid any confusion concerning the

29

two intermittency functions used herein that $\Gamma$ is a function only of the x-coordinate whereas $\bar{\gamma}$ is a function only of the y-coordinate.

Transition extent.- The assumption of a universal intermittency distribution implies that the transition zone length (transition extent) can be expressed as a function of the transition Reynolds number $u_e x_{t,i}/\nu_e$. In reference 77 it is shown, for the transition data considered, that the data are represented on the average by the equation

$$R_{e,\Delta x_t} = 5\left(R_{e,x_{t,i}}\right)^{0.8} \tag{60}$$

where $R_{e,\Delta x_t} = \dfrac{u_e}{\nu_e}\Delta x_t$. The location of the end of transition $x_{t,f}$ can then be obtained directly from equation (60) as follows:

$$x_{t,f} = x_{t,i} + 5R_e^{-1}\left(R_{e,x_{t,i}}\right)^{0.8} \tag{61}$$

where $R_e$ is the local unit Reynolds number $u_e/\nu_e$. Morkovin (ref. 12) noted that only about 50 percent of the experimental data he considered could be fitted to the low-speed universal curve of Dhawan and Narasimha, that is, to equation (60). This result was to be expected, since the data considered in reference 77 covered only a very limited Mach number range.

Potter and Whitfield (ref. 68) measured the extent of the transition zone over a rather broad Mach number range ($3 \leq M_\infty \leq 5$; $M_\infty = 8$). They observed that the transition region, when defined in terms of $R_{e,\Delta x_t}$, is basically independent of the unit Reynolds number and leading-edge geometry; that is,

$$R_{e,\Delta x_t} = \Omega\left(R_{e,x_{t,i}}, M_\infty\right) \tag{62}$$

They noted (ref. 68) that the extent of the transition region increased with increasing transition Reynolds number over the Mach number range $0 \leq M_\infty \leq 8$ for adiabatic walls. The extent of the transition region was also observed to increase with increasing Mach numbers for a fixed transition Reynolds number.

In the present analysis, because of the lack of general correlations for the extent of transition, this quantity is obtained directly from the experimental data unless otherwise noted. In particular, if heat-transfer data are available, the transition zone is assumed to lie between the initial deviation from the laminar heat-transfer distribution and the final peak heating location. The transition region defined on the basis of the Stanton number distribution is presented in figure 6. The design engineer seldom has the advantage of having access to experimental data which were obtained under the actual flight conditions. Consequently, the most probable location of transition would be obtained from a
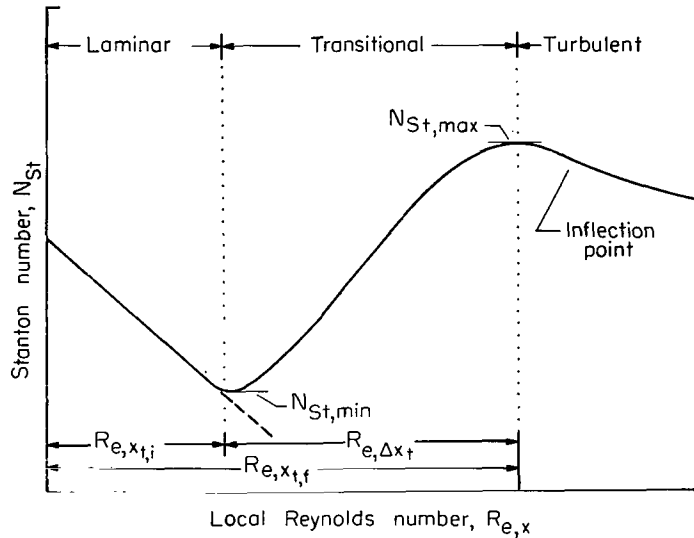
Figure 6.- Transition extent definition.

correlation such as presented in equation (56). The extent of transition could then be obtained from equation (61) or an approximate relation such as follows (see ref. 80):

$$\frac{R_{e,x_{t,f}}}{R_{e,x_{t,i}}} \approx 2 \tag{63}$$

## NUMERICAL SOLUTION OF THE GOVERNING EQUATIONS

The system of governing equations for compressible laminar, transitional, and turbulent boundary layers consist of three nonlinear partial differential equations (see eqs. (25) to (27)) and two algebraic relations. (See eqs. (17) and (18).) The most important feature of this system is that it is parabolic and therefore can be numerically integrated in a step-by-step procedure in the streamwise direction. In order to cast the equations into a form in which the step-by-step procedure can be efficiently utilized, the derivatives with respect to $\xi$ and $\eta$ are replaced by linear finite-difference quotients.

The method of linearization and solution used in the present analysis closely parallels that of Flügge-Lotz and Blottner (ref. 29) with modifications suggested by Davis and Flügge-Lotz (ref. 30) to improve the accuracy. These modifications involve the use of three-point implicit differences in the $\xi$-direction which produce truncation errors of order $\Delta\xi_1 \Delta\xi_2$ rather than $\Delta x$ as in reference 29. The primary difference between the present development and that of reference 30 is that the solution is obtained in the transformed plane for arbitrary grid-point spacing in the $\xi$-direction and for a spacing in the $\eta$-direction such that the ratio of the spacing between any two successive grid points is a constant.

31

## The Implicit Solution Technique

Finite-difference mesh model.- It has been shown for laminar boundary layers that equally spaced grid points can be used in the normal coordinate direction. (See refs. 29 and 30.) However, for transitional and turbulent boundary layers, the use of equally spaced grid points is not practical because the fine-mesh size required to obtain accurate results near the wall boundary is inefficient for the entire boundary layer. The grid-point spacing in the $\eta$-direction used in the present analysis assumes that the ratio of any two successive steps is a constant; that is, the successive $\Delta\eta_i$ form a geometric progression. (See ref. 81.)

The advantage of having variable grid-point spacing in the x-coordinate becomes clearly apparent for problems in which either the rate of change of the boundary conditions is large or discontinuous or the mean profiles are changing rapidly. A good example would be a slender blunted cone in supersonic flow. Variable grid-point spacing in the $\xi$-direction would be utilized by having very small steps in the stagnation region where the pressure gradient is severe (favorable) and again in some downstream region where transitional flow exists. A good example of discontinuous boundary conditions would be a sharp-tipped cone with a porous insert at some downstream station through which a gas is being injected into the boundary layer. Relatively large step sizes could be utilized upstream of the ramp injection; however, small steps must be used in the region of the ramp injection. Downstream of the porous region, as the flow relaxes, larger step sizes could be used. It is very important that small grid-point spacing be utilized in the transition region where the mean profiles are a strong function of the intermittency distribution.

In constructing the difference quotients, the sketch of the grid-point distribution presented in figure 7 is useful for reference. The dependent variables F, $\Theta$, and V are assumed to be known at each of the N grid points along the m - 1 and m stations, but unknown at station m + 1. The $\Delta\xi_1$ and $\Delta\xi_2$ values, not specified to be equal, are obtained from the specified x-values $\left(x_{m-1}, x_m, \text{and } x_{m+1}\right)$ and equation (20a). The relationship between the $\Delta\eta_i$ for the chosen grid-point spacing is given by the following equation:

$$\Delta\eta_i = (K)^{i-1} \Delta\eta_1 \qquad (i = 1, 2, \ldots, N) \qquad (64)$$

where K is the ratio of any two successive steps, $\Delta\eta_1$ is the spacing between the second grid point and the wall (note that the first grid point is at the wall boundary), and N denotes the total number of grid points across the chosen $\eta$-strip. The total thickness of the $\eta$-strip can then be expressed as follows:

$$\eta_N = \Delta\eta_1 \left[\frac{1 - (K)^{N-1}}{1 - K}\right] \qquad (K \neq 1) \qquad (65)$$

32
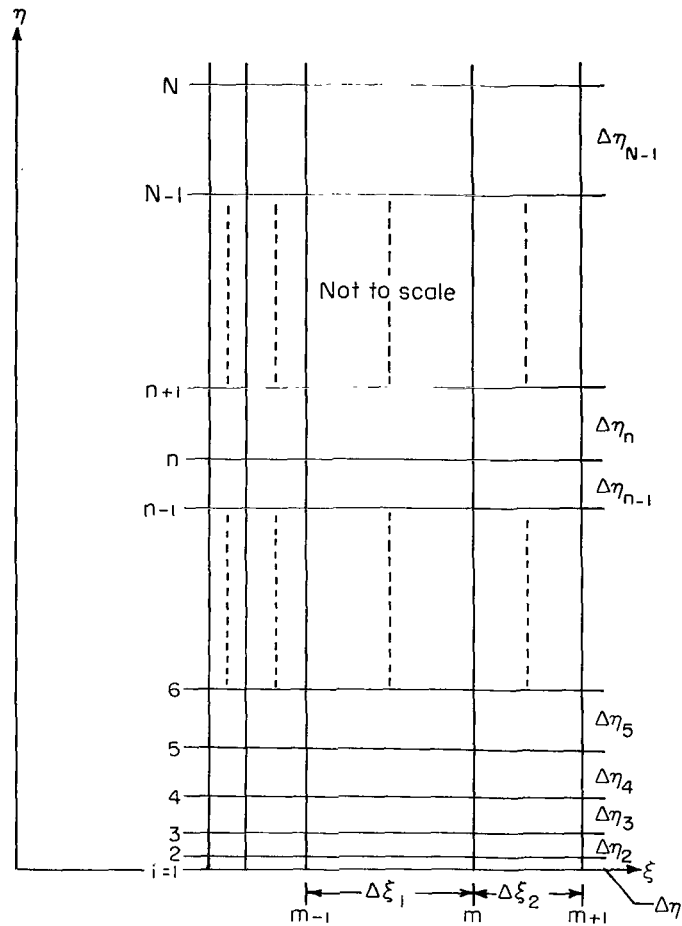
Figure 7.- Finite-difference grid model.

The selection of the optimum  K  and  N  values for a specified  $\eta_N$  depends upon the
particular problem under consideration.  The main objective in the selection is to obtain
the minimum number of grid points with which a convergent solution may be obtained and
thereby minimize the computer processing time per test case.  The laminar boundary
layer presents no problem since a  K  value of unity is acceptable; however, for transi-
tional and turbulent layers, the value of  K  will be a number slightly greater than unity,
for example, 1.02 to 1.04.  If transitional or turbulent flow occurs in a given problem;
the laminar part of the boundary layer is calculated with the value of  K  used for the
turbulent region; that is, for a given problem  K  is invariant.

Difference equations.- Three-point implicit difference relations (see appendix A)
are used to reduce the transformed momentum and energy equations (eqs. (26) and (27))
to finite-difference form.  The difference quotients produce linear difference equations
when substituted into the momentum and energy equations provided that truncation terms

33

of the order $\Delta \xi_{m-1} \Delta \xi_m$ and $\Delta \eta_{n-1} \Delta \eta_n$ are neglected. The resulting difference equations may be written as follows:

$$A_n^{(1)} F_{m+1,n-1} + B_n^{(1)} F_{m+1,n} + C_n^{(1)} F_{m+1,n+1} + D_n^{(1)} \Theta_{m+1,n-1}$$

$$+ E_n^{(1)} \Theta_{m+1,n} + F_n^{(1)} \Theta_{m+1,n+1} = G_n^{(1)} \tag{66}$$

$$A_n^{(2)} F_{m+1,n-1} + B_n^{(2)} F_{m+1,n} + C_n^{(2)} F_{m+1,n+1} + D_n^{(2)} \Theta_{m+1,n-1}$$

$$+ E_n^{(2)} \Theta_{m+1,n} + F_n^{(2)} \Theta_{m+1,n+1} = G_n^{(2)} \tag{67}$$

The coefficients $A_n^{(1)}, B_n^{(1)}, \ldots, G_n^{(1)}, A_n^{(2)}, \ldots, G_n^{(2)}$ (see appendix B) are functions of known quantities at stations $m$ and $m-1$. The dependent variable $V$ does not appear explicitly as an unknown at station $m+1$ in these equations (eqs. (66) and (67)). This condition occurs because of the particular way that the nonlinear terms $V(\partial F/\partial \eta)$ and $V(\partial \Theta/\partial \eta)$ appearing in the momentum and energy equations (eqs. (26) and (27)), respectively, are linearized (see eq. (A23)); however, equations (66) and (67) are coupled in that the dependent variables $F$ and $\Theta$ appear explicitly in each equation.

Solution of difference equations.- The system of difference equations (eqs. (66) and (67)) represents a set of exactly $2(N-1)$ equations for $2(N-1)$ unknowns since the $N-1$ unknown values of $V$ do not appear explicitly and the $A_n^{(1)}, B_n^{(1)}, \ldots, G_n^{(2)}$ coefficients are known. The proper boundary conditions to be used with the difference equations are specified in equations (32). The system of algebraic linear equations may be written as a tridiagonal matrix; consequently, an efficient algorithm is available for their simultaneous solution. The simultaneous or coupled-solution technique has been discussed in detail by Flügge-Lotz and Blottner (ref. 29). For perfect gas flows or systems where only two governing equations must be considered, the simultaneous solution technique (coupled solution) is very efficient since the equations are solved without the need for iteration procedures such as in reference 33. However, for real-gas flows or systems where more than two governing equations are required, the iterative (uncoupled) solution technique proposed by Blottner (ref. 6) should be used to avoid the large digital computer storage requirements associated with the present coupled solution technique. Another uncoupled solution technique that appears to be more flexible and faster than the method presented in reference 6 is that developed by Keller and Cebeci (ref. 82). This method should efficiently handle both three-dimensional steady and two-dimensional

34

unsteady flows as well as flows with chemically reacting species; however, the technique to date has not been used extensively.

Solution of continuity equation.- The continuity equation (eq. (25)) can be numerically solved for the $N - 1$ unknown values of $V$ at station $m + 1$ once the values of $F$ and $\Theta$ are known at station $m + 1$. Equation (25) is integrated to yield the following relation for $V$ at the grid point $(m + 1, n)$:

$$V_{m+1,n} = V_{m+1,1} - \int_0^{\eta_n} \left( 2\xi \frac{\partial F}{\partial \xi} + F \right)_{m+1} d\eta \tag{68}$$

where $V_{m+1,1}$ represents the boundary condition at the wall and is defined in equation (34) as a function of the mass transfer at the wall $(\rho v)_w$. The integral appearing in equation (68) is numerically integrated across the $\eta$-strip to obtain the $N - 1$ values of $V$. In the present analysis, the trapezoidal rule of integration was utilized; however, any sufficiently accurate numerical procedure could be used.

Initial profiles.- Initial profiles for starting the finite-difference scheme are required at two stations since three-point differences are utilized. The initial profiles at the stagnation point or line for blunt bodies, or near $x = 0$ for sharp-tipped bodies, are obtained by a numerical solution of the similar boundary-layer equations. The equations are solved by a fourth-order Runge-Kutta scheme with a Newton's iteration method to modify the initial estimates of the gradients of $F$ and $\Theta$ evaluated at the wall boundary. The $N-1$ values of $F$, $\Theta$, and $V$ which are now known at the $N - 1$ equally spaced grid points are numerically redistributed to $N - 1$ grid points whose spacing is determined from equations (64) and (65), if a variable spacing is required. The second initial profile located at station $m$ is assumed to be identical to the one located at station $m - 1$. Any errors that might be incurred because of this assumption are minimized by using an extremely small $\Delta \xi$, that is, an initial step size in the physical plane on the order of $\Delta x = 1 \times 10^{-5}$. The solution at the unknown station $m + 1$ is then obtained by the finite-difference method. Extremely small, equally spaced $\Delta \xi$-steps are used in the region of the initial profile. The step size is increased after the errors due to the starting procedure have approached zero, that is, after 10 to 15 steps in $\Delta \xi$.

It is also advantageous to have the capability of starting the solution from experimentally measured profiles, especially in the case of turbulent flow. This capability can be directly incorporated into the numerical procedure used in the present analysis. This capability is extremely useful for cases where one cannot easily locate the origin of the boundary layer, for example, on nozzle walls.

Evaluation of wall derivatives.- The shear stress and heat transfer at the wall are directly proportional to the gradient of $F$ and $\Theta$ evaluated at the wall, respectively. By using $G$ to represent a general quantity where $G_{m+1,1}$ is not specified to be zero,

the four-point difference scheme used to evaluate derivatives at the wall is as follows (see pp. 49 to 50, ref. 29):

$$\left(\frac{\partial G}{\partial \eta}\right)_{m+1,1} = Y_7 G_{m+1,1} + Y_8 G_{m+1,2} + Y_9 G_{m+1,3} + Y_{10} G_{m+1,4} \tag{69}$$

where the coefficients $Y_7, \ldots, Y_{10}$ are defined by the following relations:

$$\left.\begin{aligned} Y_7 &= -\frac{(1 + K + K^2)^2\left[K(1 + K) - 1\right] + 1 + K}{(1 + K)(1 + K + K^2)K^3 \Delta \eta_1} \\[2ex] Y_8 &= \frac{1 + K + K^2}{K^2 \Delta \eta_1} \\[2ex] Y_9 &= -\frac{1 + K + K^2}{(1 + K)K^3 \Delta \eta_1} \\[2ex] Y_{10} &= \frac{1}{(1 + K + K^2)K^3 \Delta \eta_1} \end{aligned}\right\} \tag{70}$$

For the case of equally spaced grid points in the $\eta$-direction (K = 1), equations (70) become

$$\left.\begin{aligned} Y_7 &= -\frac{11}{6\,\Delta\eta} \\[2ex] Y_8 &= \frac{18}{6\,\Delta\eta} \\[2ex] Y_9 &= -\frac{9}{6\,\Delta\eta} \\[2ex] Y_{10} &= \frac{2}{6\,\Delta\eta} \end{aligned}\right\} \tag{71}$$

and equation (69) reduces to the four-point relation (see pp. 49 to 50, ref. 29); that is,

$$\left(\frac{\partial G}{\partial \eta}\right)_{m+1,1} = -\frac{1}{6\,\Delta\eta}\left(11 G_{m+1,1} - 18 G_{m+1,2} + 9 G_{m+1,3} - 2 G_{m+1,4}\right) \tag{72}$$

### Eddy Viscosity Distribution

The primary difference between the present solution technique and other typical procedures such as those of Cebeci, Smith, and Mosinkis (ref. 83) and Beckwith and

Bushnell (ref. 84) is that the momentum and energy equations (eqs. (66) and (67)) are simultaneously solved without iteration, whereas in the techniques of these two references the momentum and energy equations are each individually solved and iterated for convergence. In the present procedure, extreme care must be used when the eddy viscosity functions $\bar{\epsilon}$ and $\hat{\epsilon}$ (see eqs. (15) and (16)) and their derivatives with respect to $\eta$ are extrapolated from the known values of $\bar{\epsilon}_{m-1,n}$ and $\bar{\epsilon}_{m,n}$ to the unknown station $m + 1$, n.

During the development of the present digital computer program, the calculations would frequently become unstable in either the transitional or turbulent flow region. This problem would always occur in one of two ways. In some instances an apparently converged solution would be obtained, but the distribution of boundary-layer thickness would not be smooth. In other instances, where the transition was abrupt or where boundary conditions were abruptly changed, the solution would not converge. The problem was caused by a wavy or rippled distribution in eddy viscosity across the layer. These ripples first occurred in the region where the inner and outer eddy viscosity models were matched. If the initial ripples were below a certain level, the solution would apparently converge, but slightly nonsmooth boundary-layer thickness distributions would occur. If the initial ripples were above a certain level, the oscillations would grow very rapidly as a function of $\xi$ and propagate throughout the layer as the solution proceeded downstream with the result that valid solutions could not be obtained downstream of the initial ripples.

The initial extrapolation of the known values of $\bar{\epsilon}_{m,n}$ and $\bar{\epsilon}_{m-1,n}$ to the unknown grid point (m + 1, n) is obtained as follows (see eq. (A3)):

$$\bar{\epsilon}_{m+1,n} = X_4\bar{\epsilon}_{m,n} - X_5\bar{\epsilon}_{m-1,n} \tag{73}$$

However, there is no assurance that the distribution of the extrapolated values at station $m + 1$ will be smooth across the layer for all possible flow conditions. If oscillations occur in the extrapolated $\bar{\epsilon}$ distribution of sufficient magnitude to cause the sign of the derivative of $\bar{\epsilon}$ with respect to $\eta$ to alternate, then the entire calculation becomes highly unstable.

The requirement of small grid-point spacing in the law-of-the-wall region contributes to the stability problem since the size of an "acceptable oscillation" is apparently a function of the grid-point spacing being utilized in the $\eta$-direction. For turbulent layers where the viscous sublayer is relatively thick, the grid-point spacing in the outer portion of the law-of-the-wall region will be large in comparison with cases where the viscous sublayer is relatively thin. Consequently, the former case can tolerate a larger ripple in the region of the match point $y_m$ than can the latter case without experiencing a change in the sign of the derivative of $\bar{\epsilon}$ with respect to $\eta$.

37

There are two possible ways to eliminate the problem caused by the oscillations in the eddy viscosity distribution. The first approach is to develop an iteration scheme; in which case the present solution technique has no advantage over other techniques (for example, refs. 33, 83, and 84), that is the advantages of the simultaneous solution would be lost. The second approach is to smooth numerically the extrapolated eddy viscosity distribution prior to the matrix solution. Both approaches were tried during the development phase of the digital computer program. The second approach was incorporated into the solution and is discussed in the remaining part of this section.

The problem posed by the ripples in the eddy viscosity distribution, if they exist, can be avoided by utilizing a three-point mean value for $\bar{\epsilon}$ at station $m + 1$, n; that is,

$$\left(\bar{\epsilon}_{av}\right)_{m+1,n} = \frac{\bar{\epsilon}_{m+1,n-1} + \bar{\epsilon}_{m+1,n} + \bar{\epsilon}_{m+1,n+1}}{3} \tag{74}$$

where $\bar{\epsilon}_{av}$ denotes the three-point mean of the eddy viscosity function. In the present procedure the eddy viscosity functions appearing on the right-hand side of equation (74) are first obtained at each grid point across the $m + 1$ station from equation (73). After these values are obtained, the three-point mean is evaluated at each of the $N - 1$ grid points from equation (74). The matrix solution for $F$ and $\theta$ is then obtained for equations (66) and (67) by using these precomputed values of $\left(\bar{\epsilon}_{av}\right)_{m+1,n}$. After the $N - 1$ values for $F$, $\Theta$, and $V$ at station $m + 1$ have been obtained, the eddy viscosity distribution is recalculated at the $m + 1$ station from equations (47) and (51) prior to moving to the next $\xi$ grid-point station. This procedure has been found to be stable under all circumstances and to yield convergent solutions for transitional and fully turbulent boundary layers.

## EXAMPLE SOLUTIONS AND COMPARISONS WITH
## EXPERIMENTAL DATA

The selection of a typical set of test cases always presents a problem since there are many possibilities from which to choose. However, the cases considered in the present paper were chosen to provide an indication of the merits of the solution technique as well as the validity of the eddy viscosity and intermittency models. In all cases presented herein, the gas is assumed to be perfect air with a constant ratio of specific heats $(\gamma = 1.4)$, a constant Prandtl number $\left(N_{Pr} = 0.72\right)$, and a constant static turbulent Prandtl number $\left(N_{Pr,t} = 0.9\right)$. The molecular viscosity $\mu$ is evaluated from Sutherland's viscosity law (eq. (18)). The external pressure distributions used are either experimental or obtained from an exact solution of the full inviscid Euler equations. All calculations were made on the Control Data Corporation 6600 digital computer.

Flows with large adverse pressure gradients are not considered in the present paper. This omission is due to the current lack of understanding of the effect of large adverse pressure gradients on the turbulent models for supersonic flow as discussed by Harris (ref. 23) and Beckwith (ref. 17) who have made comparisons of numerical results with the experimental data of McLafferty and Barber (ref. 85).

## High Reynolds Number Turbulent Flow

The accurate prediction of boundary-layer characteristics for high Reynolds number turbulent flow is important in the design of high-speed vehicles. In particular, it is important to be able to predict with accuracy the skin-friction drag. A good example of high Reynolds number turbulent flow is provided by the data of Moore and Harkness (ref. 86). The experimental skin-friction data were measured with a floating-element-type balance. The data were obtained on a sharp-leading-edge flat-plate model that completely spanned the width of the tunnel test section for $1 \times 10^7 < R_{e,x} < 2 \times 10^8$ and on the tunnel diffuser floor for $2 \times 10^8 < R_{e,x} < 1 \times 10^9$. The test conditions were as follows:

$$M_\infty = 2.8$$

$$p_{t,\infty} = 0.997 \text{ MN/m}^2$$

$$T_{t,\infty} = 311.1 \text{ K}$$

$$\frac{T_w}{T_{t,\infty}} = 0.947$$

The experimental transition location was not reported in reference 86. Consequently, for the numerical calculations, the transition location was determined by the stability index and was assumed to occur at the x-station where $\chi_{max}$ achieved a value of 2500. The extent of the transition region was calculated from equation (61). The intermittency distribution was calculated from equation (57). The solution was started at the leading edge of the sharp flat plate (x = 0) by obtaining a numerical solution of the similar boundary-layer equations. (See eqs. (B47) to (B49).) The grid-point spacing was varied in both the $\xi$- and $\eta$-directions in order to check for convergence.

The numerical results for the skin-friction coefficient distribution are compared with the experimental data in figure 8(a). The agreement is excellent over the entire Reynolds number range of the experimental data for K = 1.04; however, for K = 1.01, convergence was not attained. It should be noted at this point that the terms convergence and stability, as used in relation to the numerical method, are defined herein as in references 23 and 29. The divergence for K = 1.01 is attributed to an insufficient number of grid points in the wall region, in particular, in the thin viscous sublayer region.

The effect of the grid-point spacing parameter $K$ on the numerical solution was studied for additional values of 1.02, 1.03, 1.05, and 1.06. The solution was found to diverge for $K < 1.02$ and converge for $K \leqq 1.02$. The $C_{f,e}$ results for $K \geqq 1.02$ (other than $K = 1.04$) are not presented since the variation of $C_{f,e}$ with $K$ would not be discernible if plotted to the scale of figure 8(a). The convergence criteria used in this particular example was to decrease the $\eta$-grid-point spacing until any change which occurred in $C_{f,e}$ at a given x-solution station was beyond the fourth significant digit. The laminar curve shown in figure 8(a) was obtained by suppressing transition ($\Gamma = 0$). Grid-point spacing in the x-direction was varied from $\Delta x = 0.03$ to 1.22 cm, and convergence to the accuracy of the experimental data was obtained for all values; because of the abruptness of transition, step sizes greater than $\Delta x = 1.22$ cm were not studied.

Comparisons of the numerical results with typical experimental velocity profiles are presented in figure 8(b) for the flat-plate model and figure 8(c) for the tunnel diffuser floor. The agreement is seen to be very good.
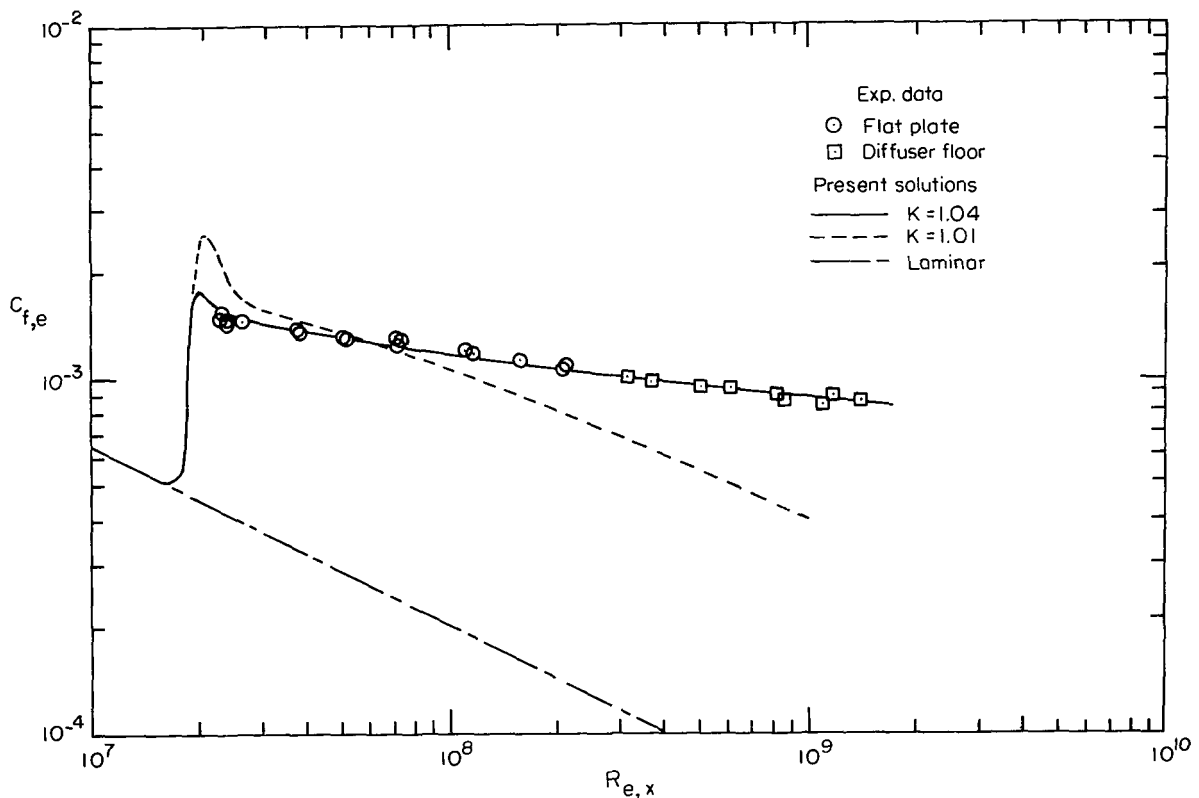


(a) Comparisons with skin-friction coefficient data.

Figure 8.- High Reynolds number turbulent flow.
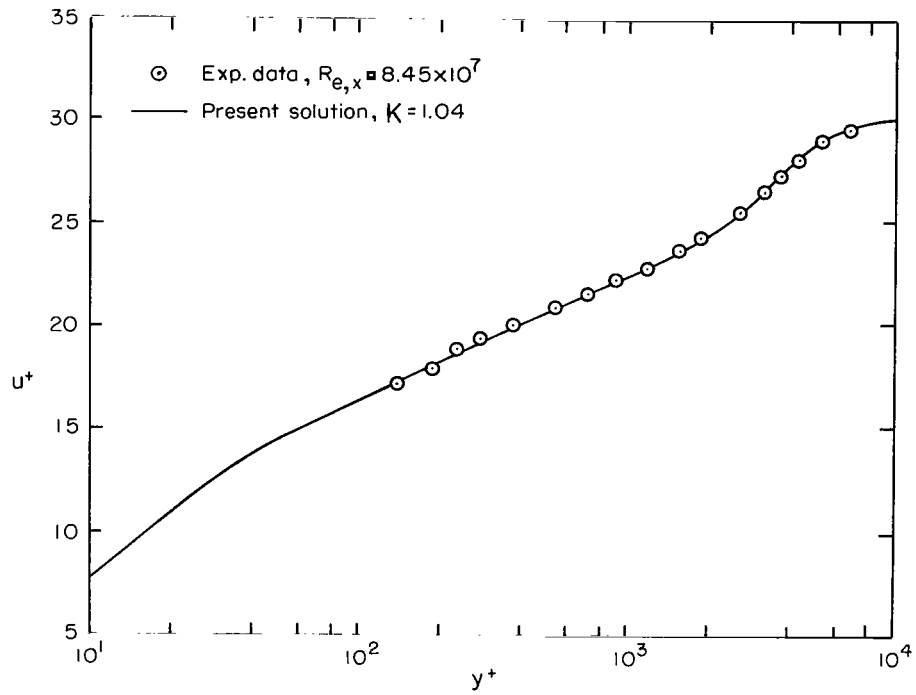
(b) Comparison with flat-plate velocity-profile data.

Figure 8.- Continued.
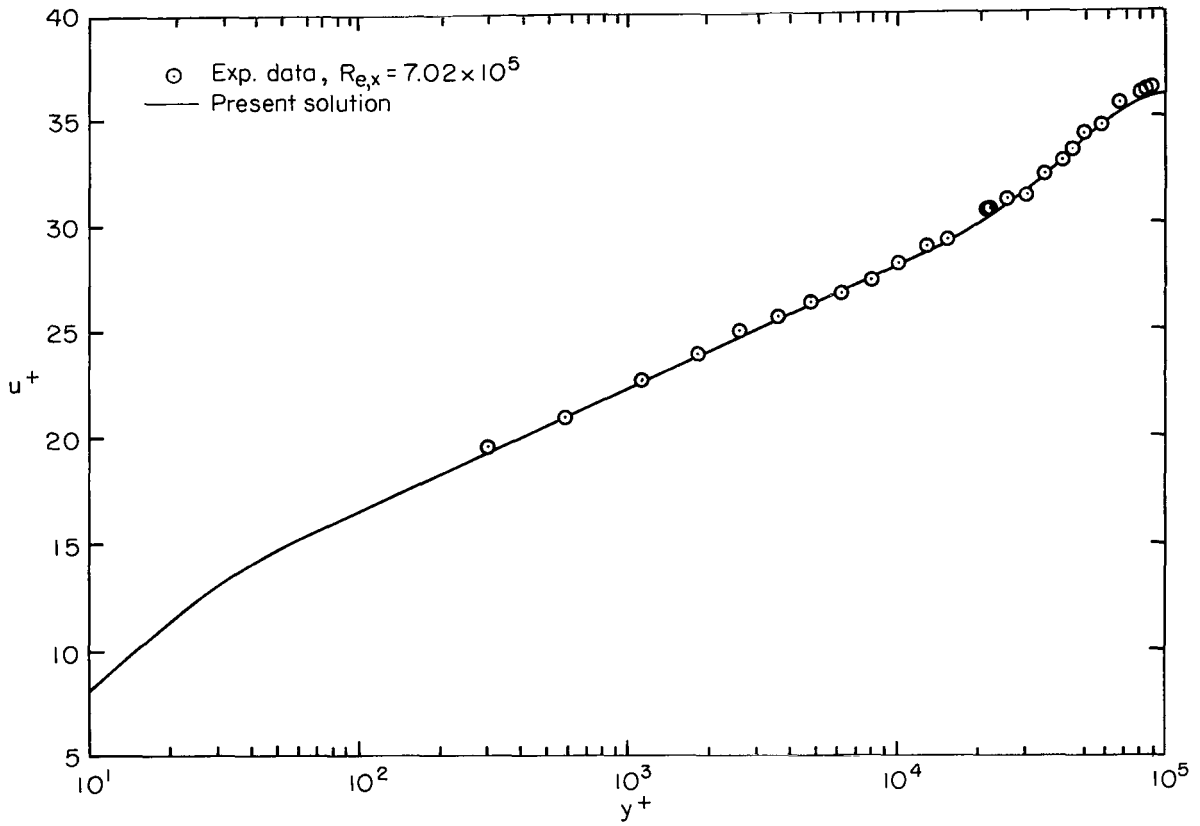
(c) Comparison with diffuser-floor velocity-profile data.

Figure 8.- Concluded.

## Tripped Turbulent Boundary Layers

In most supersonic and hypersonic wind-tunnel facilities, it is necessary to trip the laminar boundary layer on small-scale models in order to simulate the full-scale conditions where most of the boundary layer would be turbulent. An example of turbulent data obtained by tripping the laminar boundary layer is that of Coles (ref. 87). These data were obtained in the Jet Propulsion Laboratory 20-inch supersonic wind tunnel. The test model was a sharp-leading-edge flat plate. The free-stream Mach number was varied from 1.966 to 4.544. Test numbers 30, 20, and 22 (see p. 33 of ref. 87) were selected as typical test cases. For these three cases the laminar boundary layer was tripped by a fence located at the leading edge of the flat plate. (See fig. 40 of ref. 87.) The skin friction was measured at three surface locations with a floating-element balance. Boundary-layer profiles were measured at $x = 54.56$ cm.

The test conditions for the three cases are listed as follows:

| Coles' test number | $M_e$ | $p_{t,\infty}$, MN/m$^2$ | $T_{t,\infty}$, K | $T_w/T_{t,\infty}$ |
|---|---|---|---|---|
| 30 | 1.982 | 0.09468 | 302.8 | 0.8295 |
| 20 | 3.701 | .1373 | 311.7 | .7152 |
| 22 | 4.554 | .3894 | 307.8 | .6764 |

Transition was assumed to occur near the leading edge of the plate for the numerical calculations $x_{t,i} = 0.15$ cm and to be completed ($\Gamma = 1.0$) at $x_{t,f} = 0.30$ cm. Twenty equally spaced x-solution stations were used in the region $0 \leq x \leq 0.30$ cm; the x-solution stations were then equally spaced 0.30 cm apart over the remainder of the plate. The total number of grid points in the $\eta$-direction and the grid-point spacing parameter K were assigned values of 301 and 1.04, respectively. The computer processing time per test case was approximately 3 minutes. The numerical results are compared with the experimental velocity and Mach number profile data in figure 9 for the three test cases. The agreement between the numerical results and the experimental data is very good for all three test cases. In particular, it should be noted that the experimental skin-friction coefficients (see figs. 9(a), 9(c), and 9(e)) were predicted to within 1 percent, which is well within the accuracy range of 2 percent as quoted for the data in reference 87. The slight disagreement between the numerical results and the Mach number profiles for increasing free-stream Mach number may be due in part to eddy conductivity effects caused by the simple $N_{Pr,t}$ model utilized in the calculations.
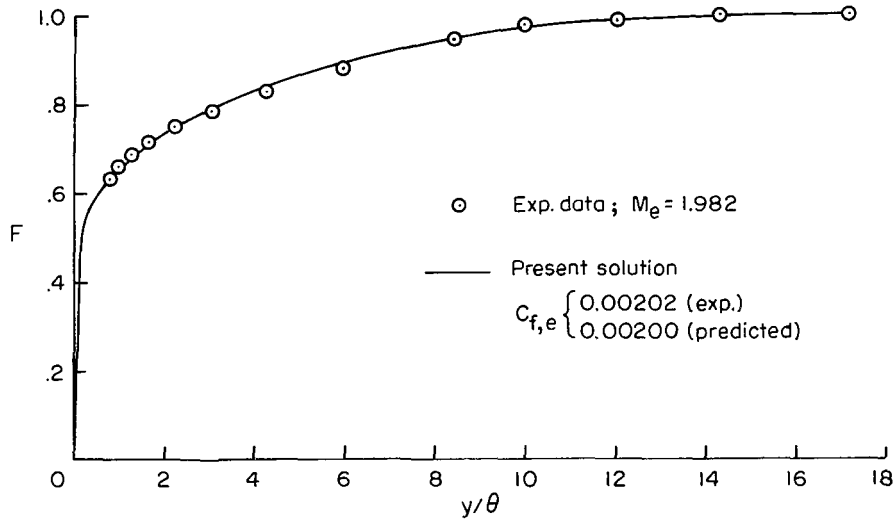
(a) Velocity profile and skin-friction coefficient for $M_\infty = 1.982$.
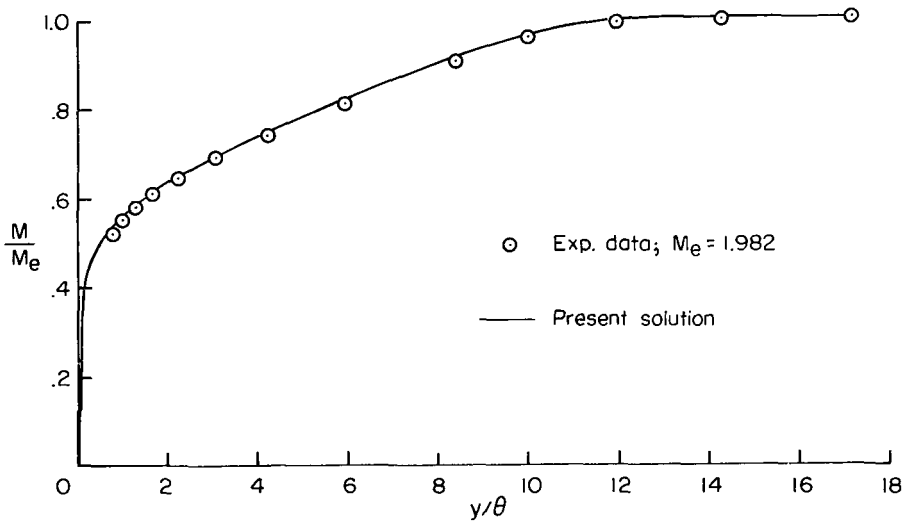


(b) Mach number profile for $M_\infty = 1.982$.

Figure 9.- Comparisons with experimental data for tripped turbulent boundary layers.
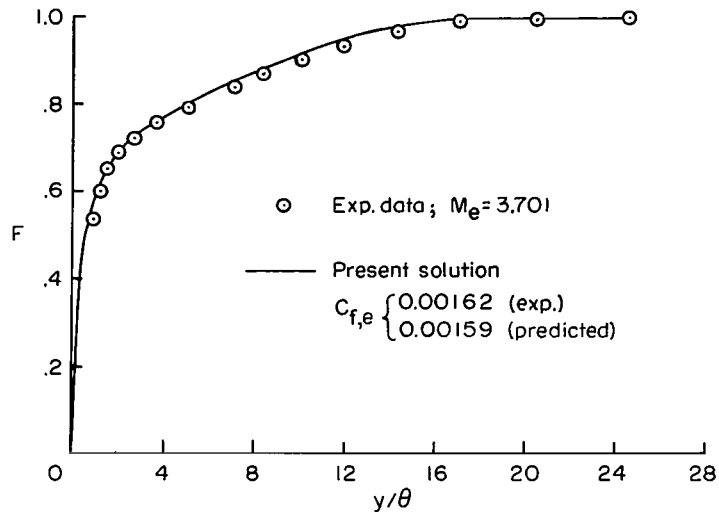
(c) Velocity profile and skin-friction coefficient for $M_\infty = 3.701$.
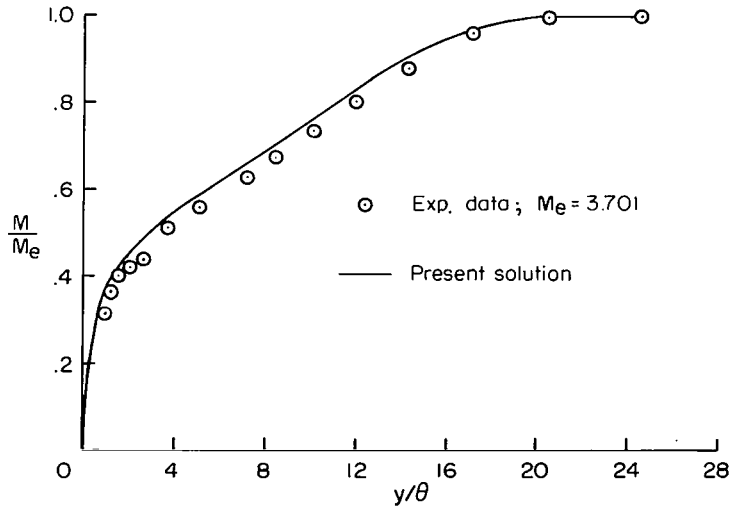


(d) Mach number profile for $M_\infty = 3.701$.

Figure 9.- Continued.
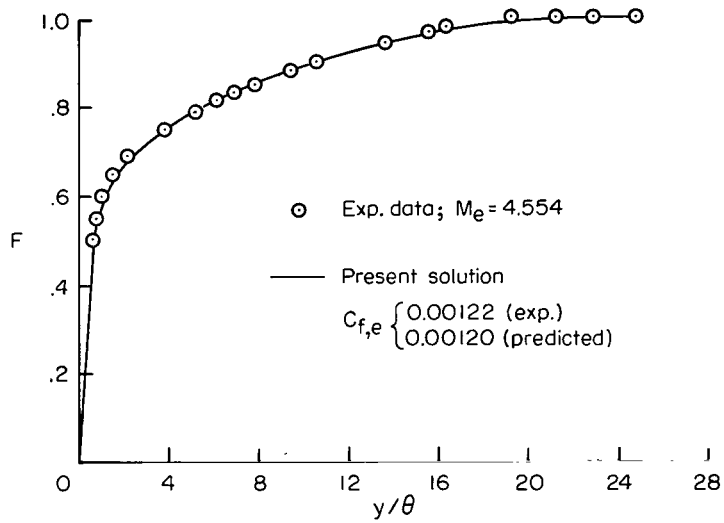
(e) Velocity profile and skin-friction coefficient for $M_\infty = 4.554$.
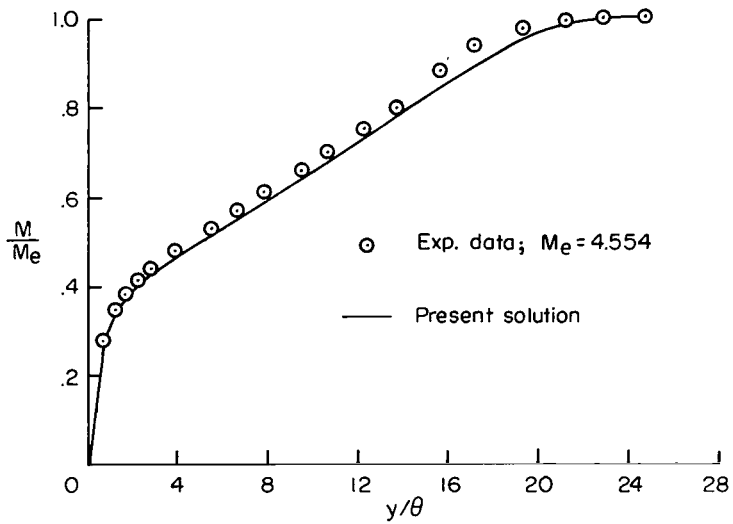


(f) Mach number profile for $M_\infty = 4.554$.

Figure 9.- Concluded.

## Laminar Flow With Mass Injection

An example of data for laminar flow with transpiration cooling is presented by Marvin and Akin (ref. 88). These data were obtained over a range of injection rates for a sharp-tipped $5^\circ$ cone. The cone was solid for $x < 9.53$ cm; the remainder of the cone was porous. The test conditions were as follows:

$$M_\infty = 7.4$$

$$p_{t,\infty} = 4.137 \text{ N/m}^2$$

$$T_{t,\infty} = 833.3 \text{ K}$$

$$\frac{T_w}{T_{t,\infty}} = 0.38$$

The air-injection parameter $\tilde{F}$ ranged from a minimum value of zero (no injection) to a maximum value of $1.3903 \times 10^{-3}$.

A comparison of the heating rate at the wall normalized by the heating rate at the wall just prior to the ramp injection ($x = 9.53$ cm) is presented in figure 10(a). The mass injection distribution was not uniform, as can be seen from the plot of the actual injection distribution normalized by the ideal injection rate. The nonuniform distribution of mass injection was utilized in the numerical solutions. The agreement between the numerical results and the experimental heat-transfer data is excellent over the entire injection range. Marvin and Sheaffer (ref. 89) have also obtained numerical solutions for this test case which are in very good agreement with the experimental data.

This particular case is an example where variable step size must be used in the region of the ramp injection ($x/L = 1.0$). For this case the $\Delta x$ values (grid-point spacing in the x-direction) were constant and equal to 0.3 cm up to $x/L = 0.99$ at which point the step size was decreased to a value of 0.03 cm through the ramp injection region. The step size was then progressively increased up to a value of 0.3 cm at $x/L = 1.5$. The flow was laminar; consequently, K was set to unity and 101 equally spaced grid points were used in the $\eta$-direction. The digital computer processing time per test case was approximately 2 minutes.

The effect of mass injection on the vorticity Reynolds number is shown in figures 10(b) and 10(c). In figure 10(b) the maximum value of the vorticity Reynolds number $\chi_{max}$ is seen to increase with increasing x. In particular, the $y/\delta$ value at which $\chi_{max}$ occurred is in excellent agreement with the location of the critical-layer position. (See ref. 72.) The effect of mass injection on the vorticity Reynolds number distribution is presented in figure 10(c). Increasing mass injection increases the value of $\chi_{max}$ at a given x-station as well as moves the location at which the maximum occurs $(y/\delta)_{\chi_{max}}$ toward the outer edge of the boundary layer.
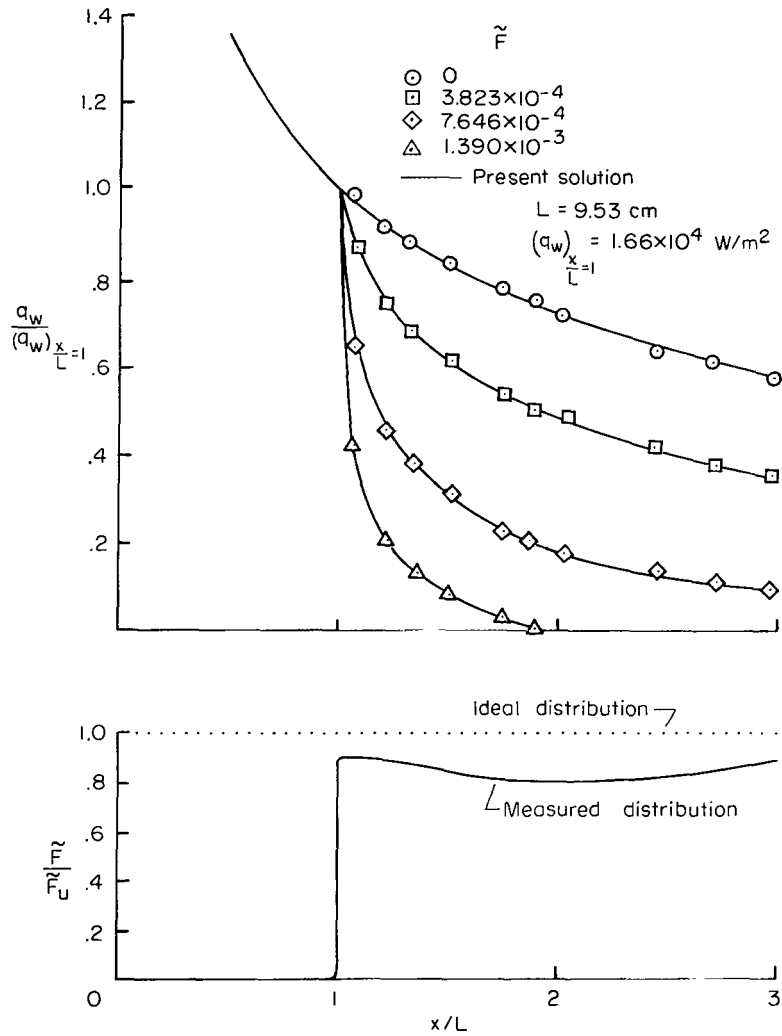
(a) Comparisons with heat-transfer data.

Figure 10.- Hypersonic laminar boundary-layer flow with mass injection.
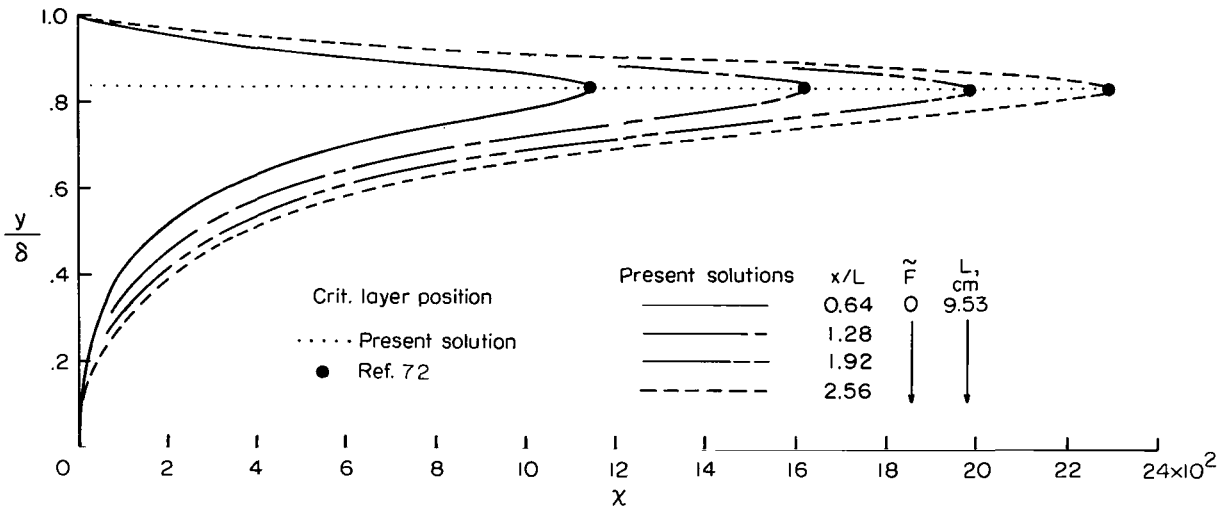
(b) Vorticity Reynolds number distribution for zero mass injection.
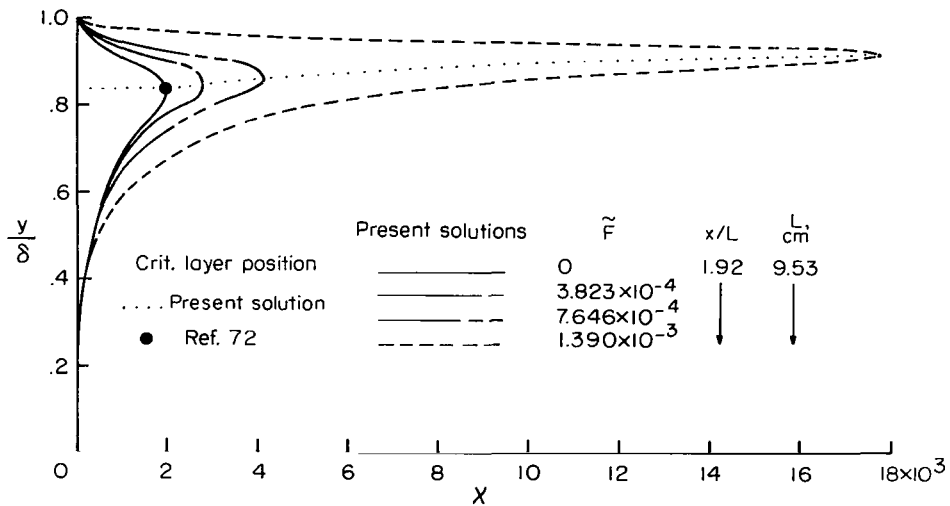


(c) Vorticity Reynolds number distribution for variable mass injection.

Figure 10.- Concluded.

# Laminar Blunt Body Flow

The numerical procedure as presented in the present paper has been applied to a number of blunt-body flows at supersonic and hypersonic speeds. A typical case for a hemispherical nose is presented in figure 11. The test conditions for this case were as follows:

$$M_\infty = 10.4$$

$$p_{t,\infty} = 10.77 \text{ MN/m}^2$$

$$r_n = 0.08891 \text{ m}$$

$$T_{t,\infty} = 1222 \text{ K}$$

$$\frac{T_w}{T_{t,\infty}} = 0.25$$

Solution for this particular example has been obtained by Marvin and Sheaffer (ref. 89) and Clutter and Smith (ref. 90). The heating rate and shear stress at the wall referenced to the maximum heating rate and shear stress, respectively, are compared with the results presented in references 89 and 90 in figure 11.

Equally spaced grid points were used in the $\xi$-direction. Solutions were obtained for $\Delta x$ values ranging from 0.03 cm to 0.60 cm in order to check for convergence.
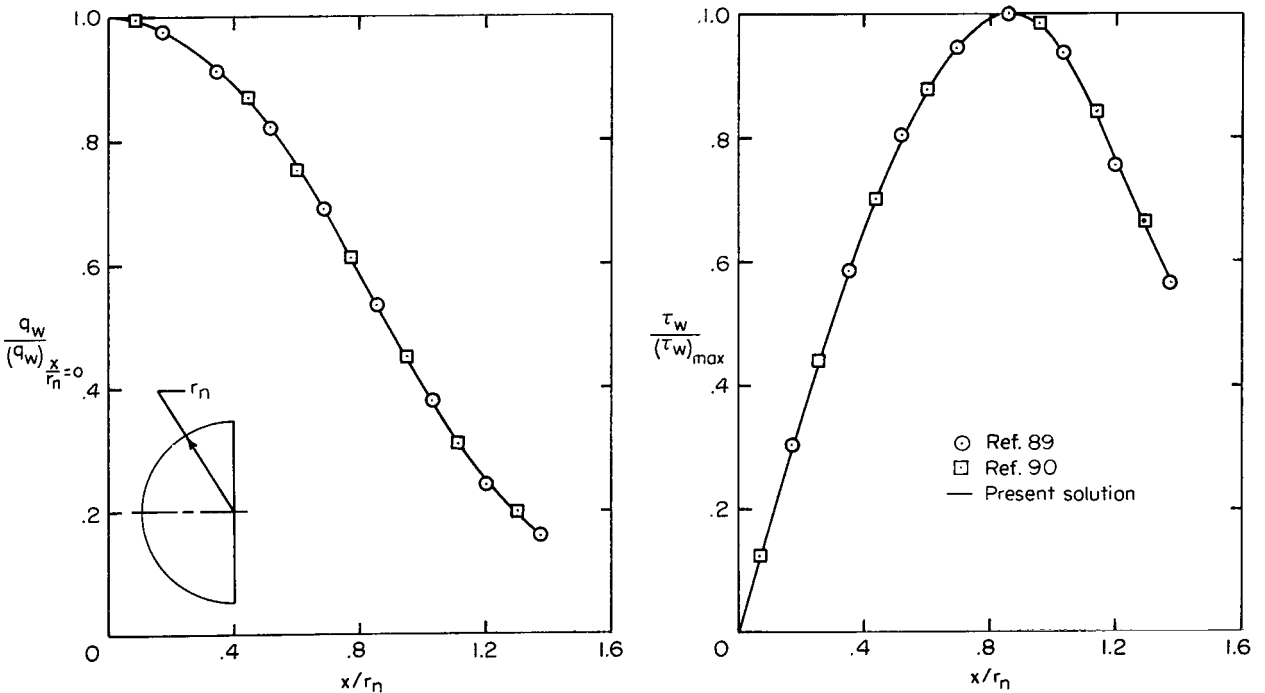


Figure 11.- Hypersonic blunt-body flow.

The data shown in figure 11 were calculated by using $\Delta x = 0.15$ cm although much larger steps could be used for engineering calculations, for example, $\Delta x = 0.3$ cm. The grid-point spacing in the $\eta$-direction was held constant ($K = 1$).

Another example of hypersonic laminar flow is presented in figure 12. These experimental data were obtained on a spherically blunted, $25^\circ$ half-angle cone. (See ref. 91.) The test conditions were as follows:

$$M_\infty = 7.95$$

$$p_{t,\infty} = 6.31 \ \mathrm{MN/m^2}$$

$$T_{t,\infty} = 783 \ \mathrm{K}$$

$$\frac{T_w}{T_{t,\infty}} = 0.38$$

The pressure distribution used in the numerical solution was obtained by the technique presented in reference 92 and is compared with the experimental data in figure 12(a).
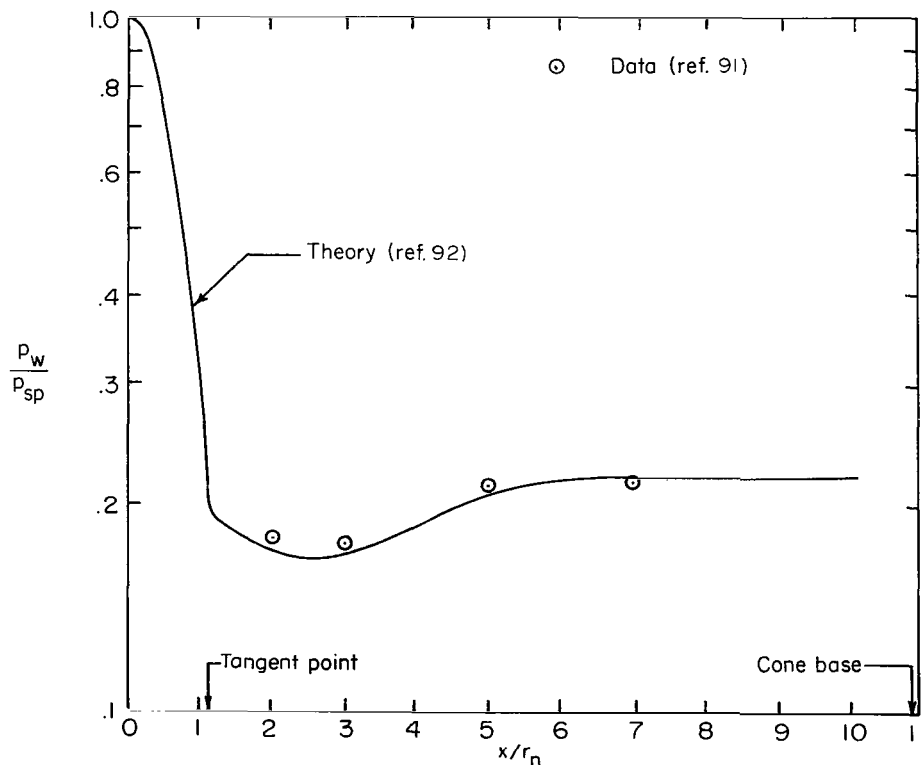


(a) External pressure distribution.

Figure 12.- Laminar flow over a spherically blunted $25^\circ$ half-angle cone.
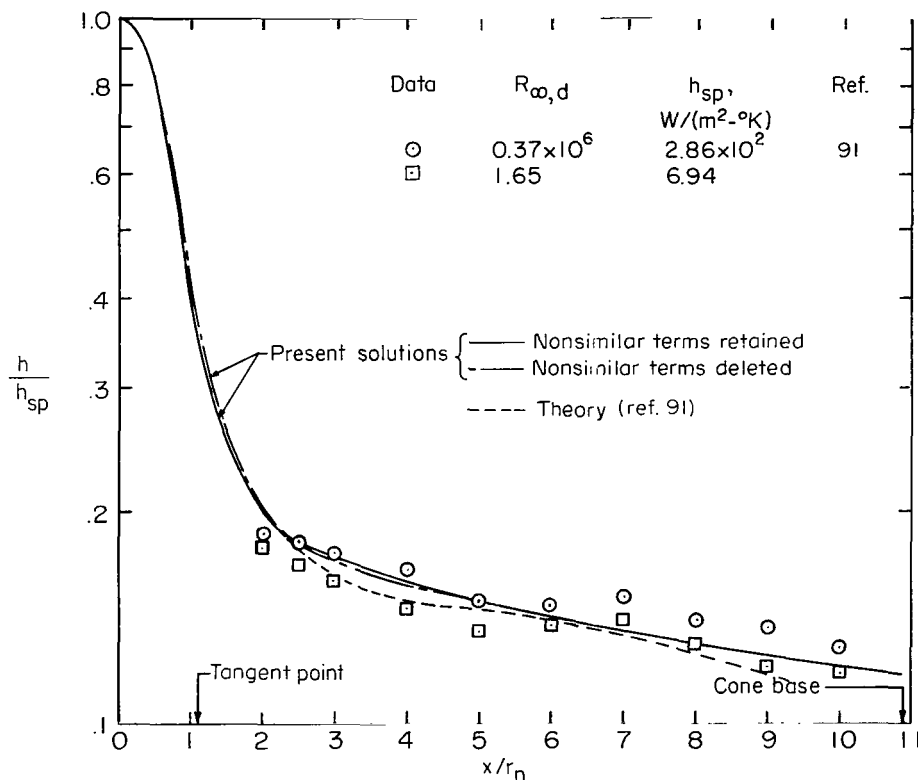
(b) Comparison with heat-transfer data. $r_n = 0.10$; $d = 1.27$ cm.

Figure 12.- Concluded.

The numerical results for the heat-transfer coefficient distribution referenced to the stagnation-point value are compared with the experimental data in figure 12(b) and also with the local similarity method as reported in reference 91. The present results are in somewhat better agreement with the data than the local similarity results presented in reference 91. In order to assess the difference between the two predictions, the present method was utilized as a local similarity method by eliminating the nonsimilar terms from the governing equations. (See eqs. (B47) to (B49).) The results of this solution are also shown in figure 12(b) and indicate that the discrepancies in the present nonsimilar solution and the local similarity solution presented in reference 91 are not due to the nonsimilar terms in the governing equations.

## Nonsimilar Flow With Transverse and Longitudinal Curvature

## and Variable Pressure Gradients

Turbulent boundary-layer data for flows where variable pressure gradients exist are few in number. A good example of a case where both favorable and adverse pressure

gradients occur as well as where transverse curvature effects are important is the data of Winter, Rotta, and Smith (ref. 93). The model used in the study was an axisymmetric configuration with continuous derivatives. (See fig. 13(a).)

Experimental data are presented in reference 93 for the turbulent region; however, the solutions presented herein were obtained by starting the calculations at the tip of the sharp-cone forebody (x = 0). This particular configuration has received considerable attention over the past 2-year period. Calculations have been made by Herring and Mellor (ref. 94), Cebeci, Smith, and Mosinkis (ref. 83), and Beckwith (ref. 17); however, these solutions were all started by utilizing the experimentally measured profiles at station $z/c = 2$. The solutions presented herein are believed to be the first obtained without any dependence whatsoever on experimental profile or skin-friction data.

The test conditions for the two cases considered are as follows:

|  | Case 1 | Case 2 |
|---|---|---|
| $M_\infty$ | 1.398 | 1.70 |
| $p_{t,\infty}$, MN/m$^2$ | 0.0441 | 0.0475 |
| $T_{t,\infty}$, K | 297.8 | 297.8 |
| $\dfrac{T_w}{T_{t,\infty}}$ | 0.976 | 0.971 |

$$z/c = 0; \quad c = 1.524 \text{ m}$$
$$r_0/c = 0.36397 \, (z/c)$$
$$z/c = 0.14158$$
$$r_0/c = 6.3473 \, (z/c)^4 - 6.49221 \, (z/c)^3 + 1.22668 \, (z/c)^2 + 0.33498 \, (z/c) - 0.00461$$
$$z/c = 0.45725$$
$$r_0/c = -0.236382 \, (z/c)^3 + 0.60762 \, (z/c)^2 - 0.595521 \, (z/c) + 0.22694$$
$$z/c = 0.64473$$
$$r_0/c = -53.58258 \, (z/c)^4 + 150.87806 \, (z/c)^3 - 158.03866 \, (z/c)^2 + 72.96859 \, (z/c) - 12.4939$$
$$z/c = 0.76317$$
$$r_0/c = 0.236382 \, (z/c)^3 + 0.390789 \, (z/c)^2 + 0.290242 \, (z/c) - 0.064001$$
$$z/c = 1.0$$
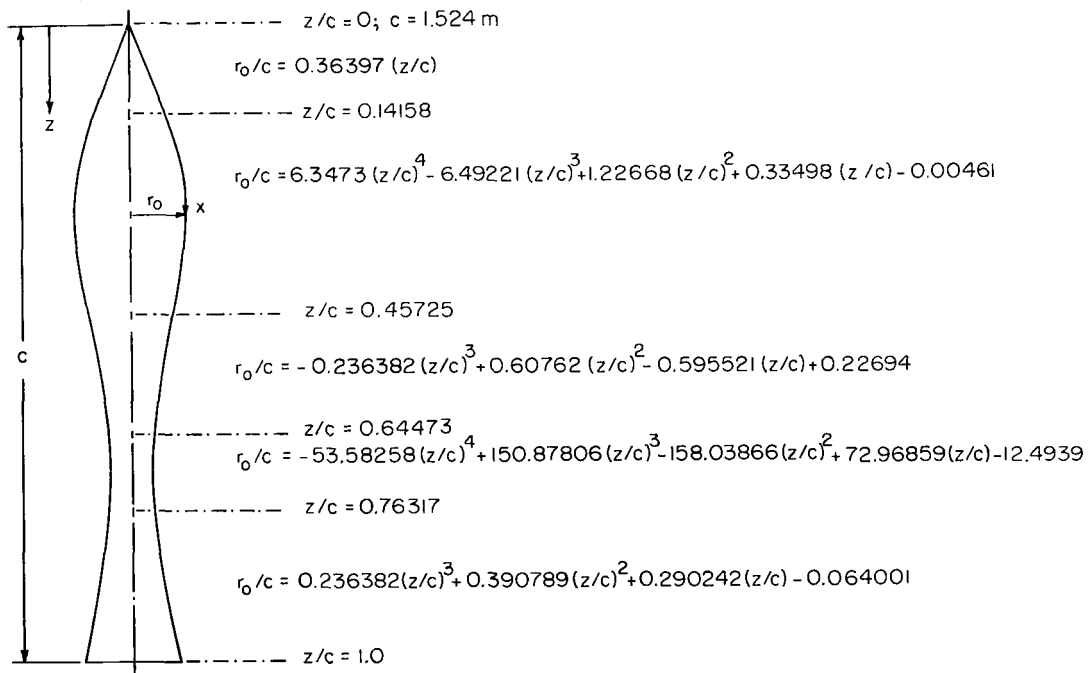
(a) Geometry of configuration.

Figure 13.- Comparisons with data for highly nonsimilar supersonic flow with transverse curvature effects.
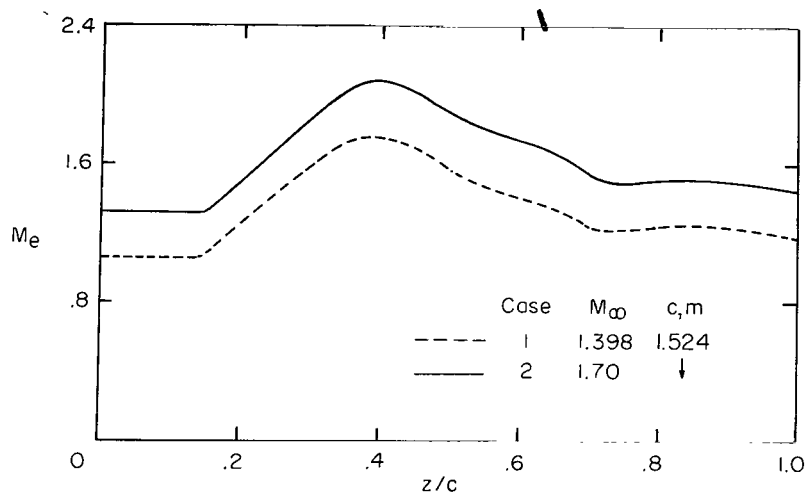
(b) Experimental edge Mach number distribution.
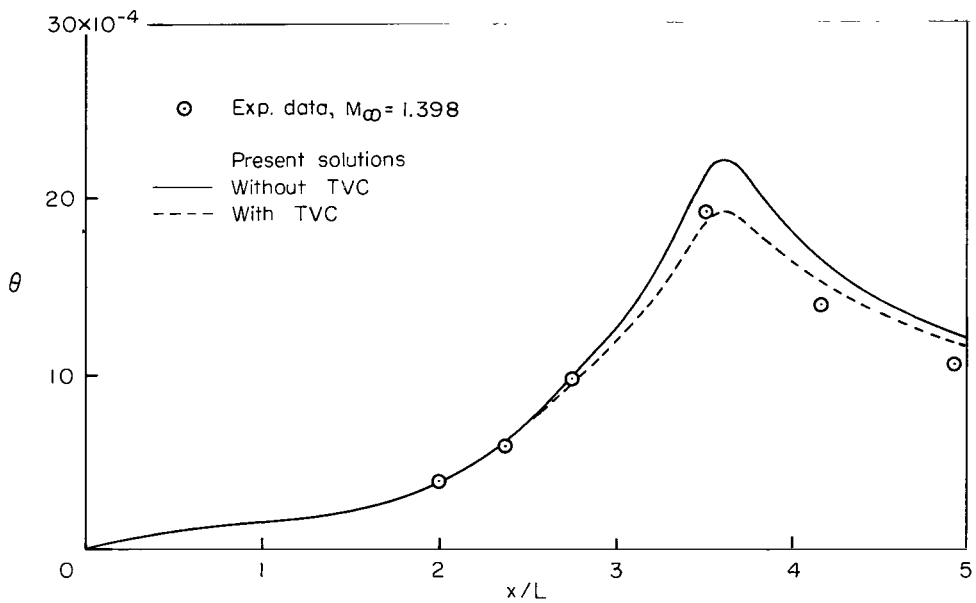


(c) Momentum thickness for $M_\infty = 1.398$. $L = 30.48$ cm.

Figure 13.- Continued.
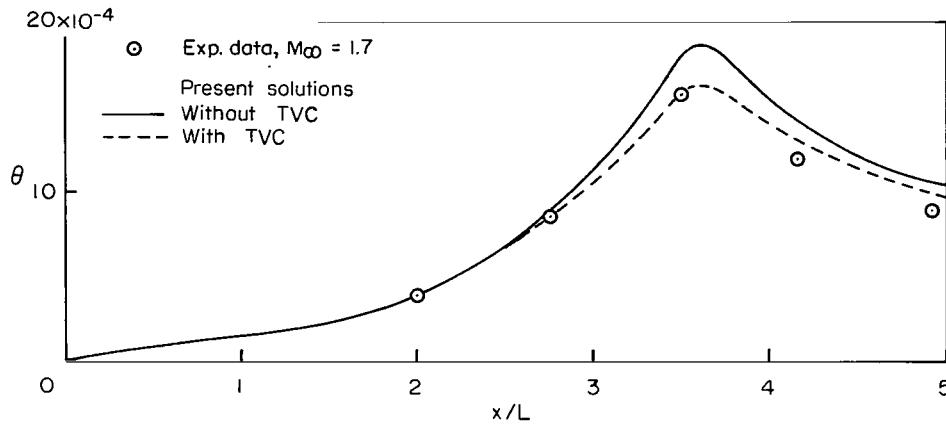
(d) Momentum thickness for $M_\infty = 1.7$.   $L = 30.48$ cm.
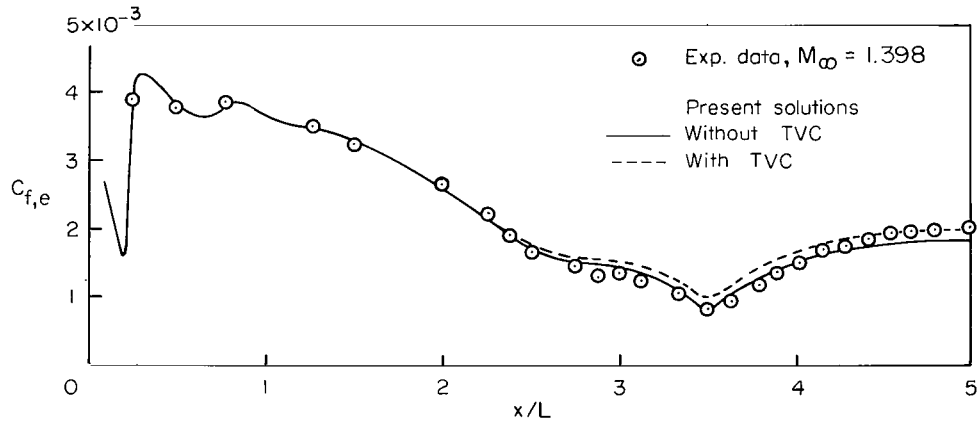


(e) Skin-friction coefficient for $M_\infty = 1.398$.   $L = 30.48$ cm.
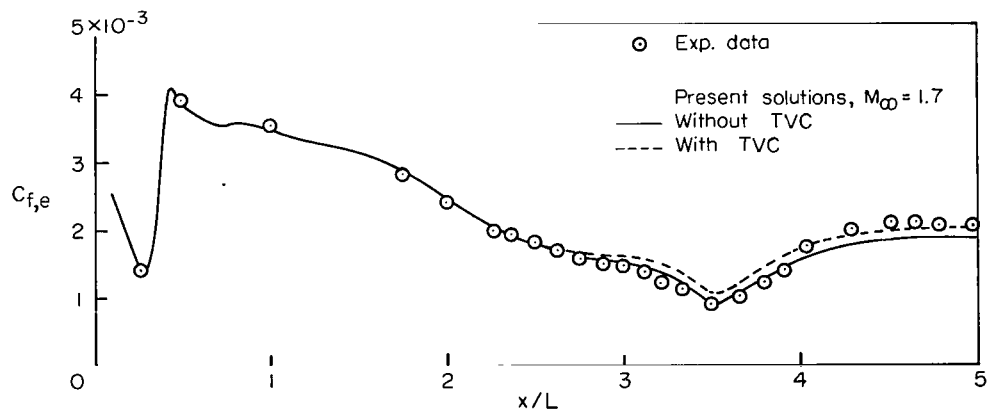


(f) Skin-friction coefficient for $M_\infty = 1.7$.   $L = 30.48$ cm.

Figure 13.- Concluded.

The experimental Mach number distributions are presented in figure 13(b); these distributions were used as an input to the digital computer program instead of $p_e$.

The initial profiles required to start the finite-difference solution were obtained by an exact solution of the similar boundary-layer equations (eqs. (B47) to (B49)) near $x = 0$. Transition was initiated at the x-station where $\chi_{max}$ achieved a value of 2500. The transition extent was then computed from equation (63). The grid-point spacing in the $\xi$-direction varied from a maximum $\Delta x$ value of 0.3 cm to a minimum value of 0.03 cm in the regions of large pressure gradients. Variable grid-point spacing in the $\eta$-direction was required with a K value of 1.04. Calculations were made for K values of 1.03 and 1.05 to insure convergence. The computer processing time per test case was approximately 4 minutes.

The numerical results are compared with the experimental data for momentum thickness and skin-friction coefficient distributions in figures 13(c) to 13(f). The agreement between the numerical and experimental momentum thickness and skin-friction coefficient distributions is good for both test cases. In particular, note the agreement with the minimum $C_{f,e}$ data point in transition (fig. 13(f)). It is also of interest to note that although the solutions with transverse curvature were in closest agreement with the $\theta$ values for $x/L < 3.5$, the solutions without transverse curvature agreed best with the $C_{f,e}$ values in the same region. A similar trend was noted in reference 83.

Laminar, Transitional, and Turbulent Flow on Sharp Cones

Fischer (ref. 61) studied the effect of unit Reynolds number $R_e$ on transition on a sharp $10°$ half-angle cone. The test conditions were as follows:

$$M_\infty = 7$$

$$p_{t,\infty} = 1.384 \text{ to } 4.199 \text{ MN/m}^2$$

$$T_{t,\infty} \approx 572 \text{ K}$$

$$\frac{T_w}{T_{t,\infty}} \approx 0.52$$

The boundary-layer edge values were obtained from reference 95. The experimental location of transition and the extent of transition were used in the numerical calculations. The computer processing time per test case was approximately 2 minutes.

Comparisons of the numerical results with the experimental Stanton number distributions are presented in figures 14(a) to 14(f). The value of $(\chi_{max})_{cr}$ at the experimental transition location is noted in each figure. The recovery factor used to compute the adiabatic wall temperature (see ref. 23) was as follows:

$$r_f = \sqrt{N_{Pr}}\left[1 + \left(N_{Pr}^{-1/6} - 1\right)\Gamma\right] \tag{75}$$

56
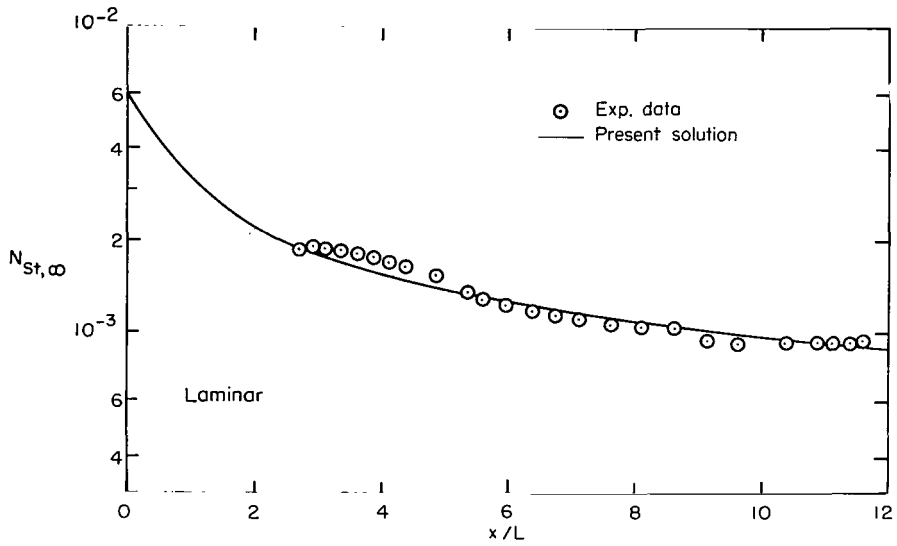
(a) $M_\infty = 7$; $R_e = 9.84 \times 10^6$ per meter.
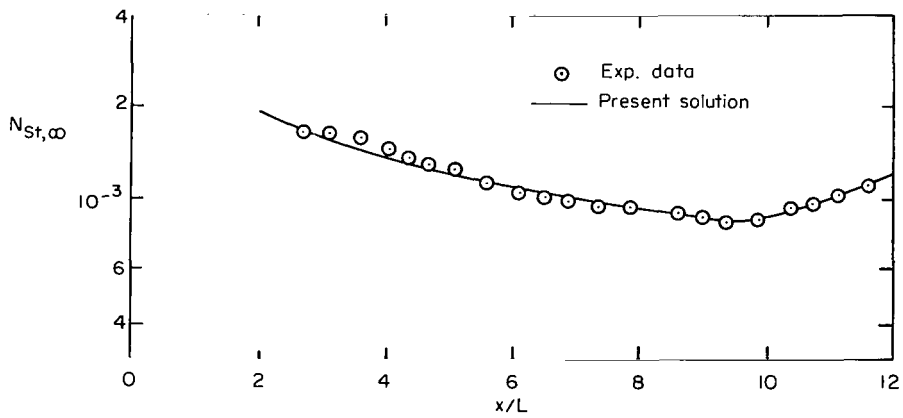


(b) $M_\infty = 7$; $R_e = 1.293 \times 10^7$ per meter; $\left(X_{max}\right)_{cr} = 2450$.

Figure 14.- Comparisons with experimental Stanton number distributions for hypersonic flow over sharp-tipped cones. L = 2.54 cm.
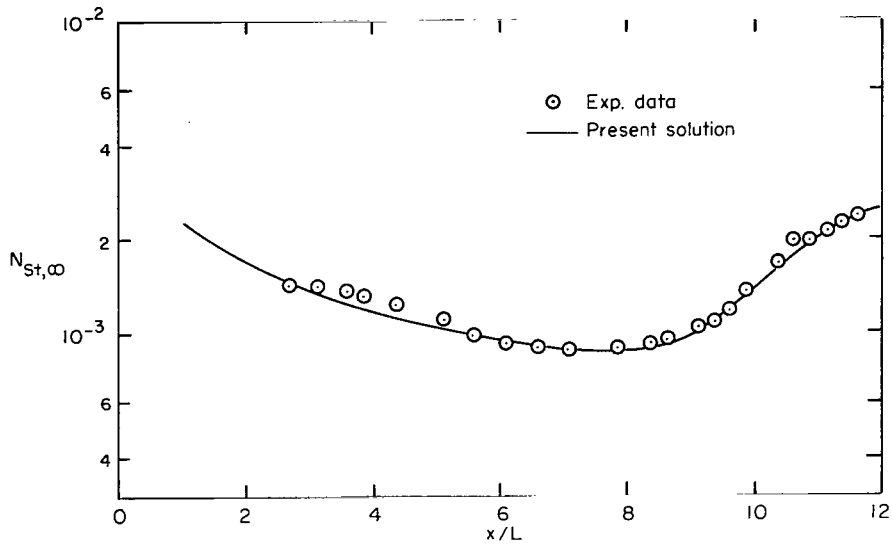
(c)  $M_\infty = 7$;  $R_e = 1.739 \times 10^7$ per meter;  $\left(X_{max}\right)_{cr} = 2500$.
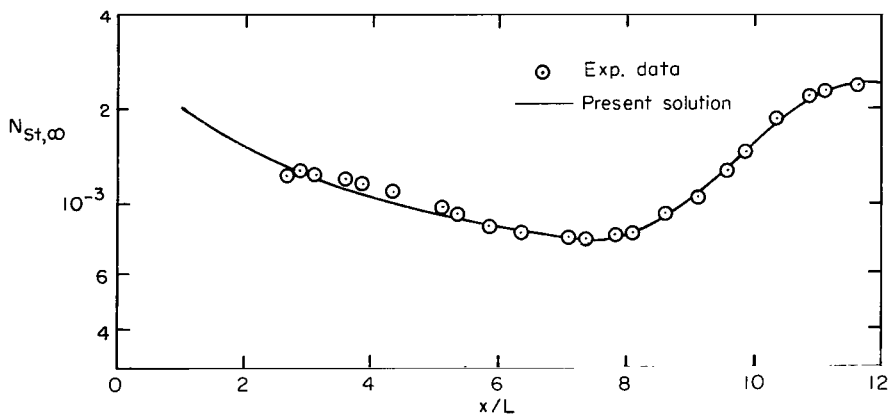


(d)  $M_\infty = 7$;  $R_e = 2.195 \times 10^7$ per meter;  $\left(X_{max}\right)_{cr} = 2800$.

Figure 14.- Continued.
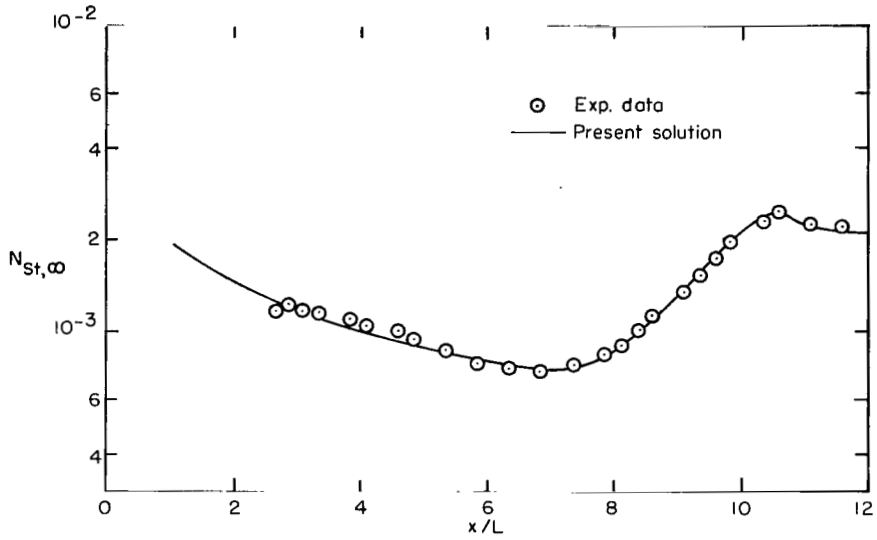
(e)  $M_\infty = 7$;  $R_e = 2.454 \times 10^7$ per meter;  $\left(X_{max}\right)_{cr} = 2850$.
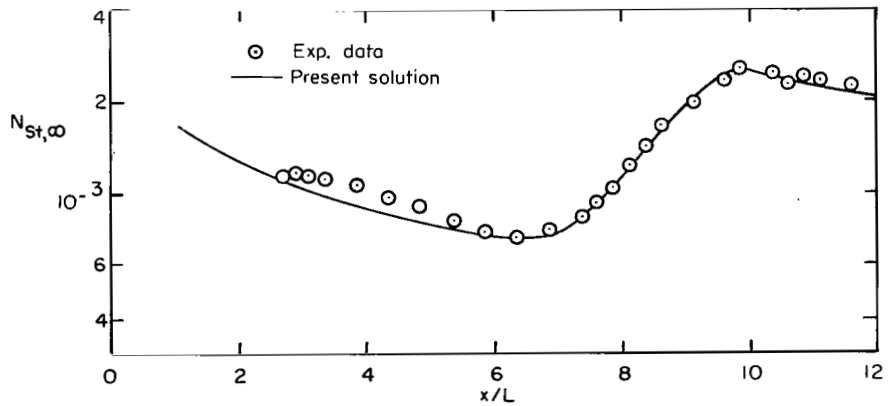


(f)  $M_\infty = 7$;  $R_e = 3.012 \times 10^7$ per meter;  $\left(X_{max}\right)_{cr} = 3015$.

Figure 14.- Continued.
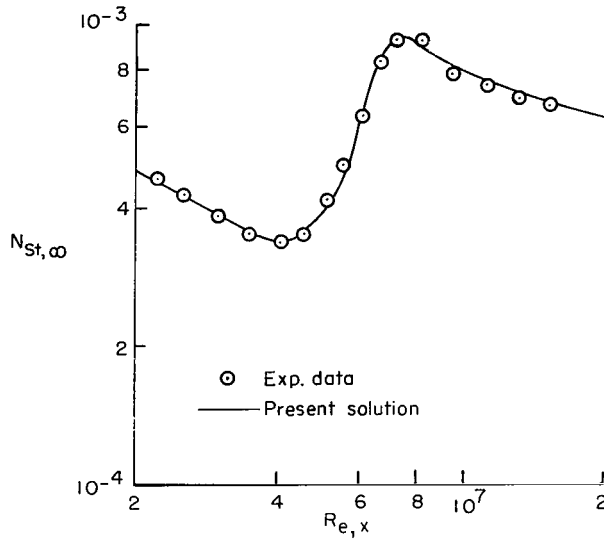
(g)   $M_{\infty} = 8$;   $R_e = 4.101 \times 10^7$ per meter;   $(X_{max})_{cr} = 2500$.
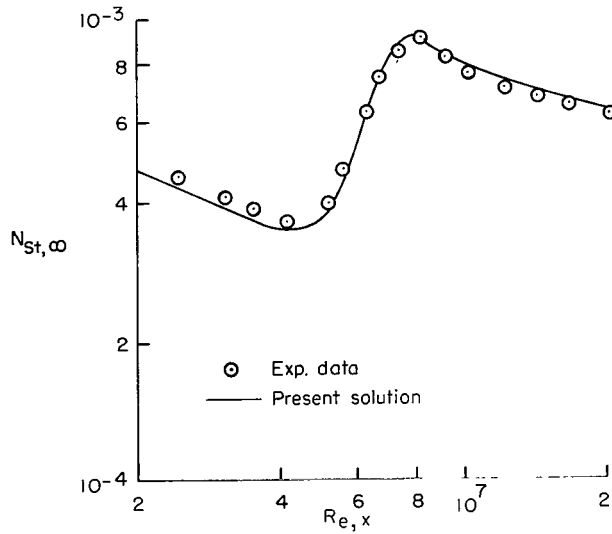


(h)   $M_{\infty} = 8$;   $R_e = 5.643 \times 10^7$ per meter;   $(X_{max})_{cr} = 2750$.

Figure 14.- Concluded.

where $\Gamma$ is the intermittency. (See eq. (57).) The experimental and numerical heat-transfer-coefficient distributions were reduced to the Stanton number distributions as presented in figure 14 with a common recovery factor; that is, the recovery factor obtained from equation (75).

Two similar cases are presented in figures 14(g) and 14(h). These data were obtained at the Langley Research Center on a $10^O$ sharp cone model. The test conditions for these data were as follows:

|  | Case 1 | Case 2 |
|---|---|---|
| $M_\infty$ . . . . . . . . . . . . . . . . . . . . . . . . . . . . . . . . | 8 | 8 |
| $p_{t,\infty}$, $MN/m^2$ . . . . . . . . . . . . . . . . . . . . . . . . . . . | 13.93 | 17.38 |
| $T_{t,\infty}$, K . . . . . . . . . . . . . . . . . . . . . . . . . . . . . | 809.9 | 759.4 |
| $\dfrac{T_w}{T_{t,\infty}}$ . . . . . . . . . . . . . . . . . . . . . . . . . . . . . | 0.40 | 0.42 |

The local values of $M_e$, $R_e$, and $\left(\chi_{max}\right)_{cr}$ are indicated in the figures; $\left(\chi_{max}\right)_{cr}$ ranged from 2450 to 3015. The agreement in the peak heating region is good; in particular, note the predicted "overshoot" behavior near the end of transition and its agreement with the data.

### Laminar, Transitional, and Turbulent Flow Over a Hollow Cylinder

O'Donnell (ref. 96) studied laminar, transitional, and turbulent boundary-layer flows over a hollow cylinder. Total-pressure profiles were measured at various stations along the cylinder. The test conditions were as follows:

$$M_\infty = 2.41$$

$$p_{t,\infty} = 23.7 \text{ to } 406.5 \text{ kN/m}^2$$

$$T_{t,\infty} = 311.1 \text{ K}$$

$$\frac{T_w}{T_{t,\infty}} = 0.9$$

For this particular set of calculations, the experimental transition location was utilized; however, the extent of transition was calculated from equation (61). Consequently, the only variable inputs to the computer program were the specific values of the total pressure $p_{t,\infty}$ and the transition location $x_{t,i}$.

The velocity profile comparisons are presented in figures 15(a) to 15(e). For a unit Reynolds number of $2.2 \times 10^6$ per meter, the boundary layer was laminar throughout the measured area. The velocity profiles are similar and the agreement between the numerical results and experimental data is very good. (See fig. 15(a).) For unit Reynolds
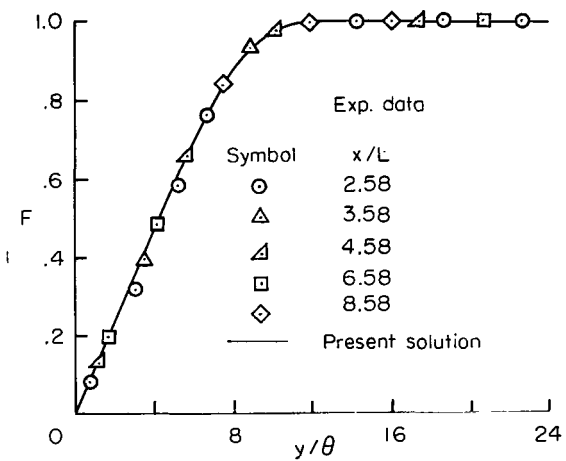
(a) $R_e = 2.2 \times 10^6$ per meter.
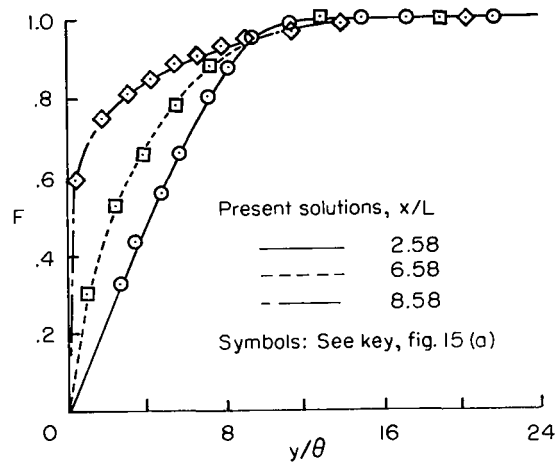
(b) $R_e = 9.45 \times 10^6$ per meter.
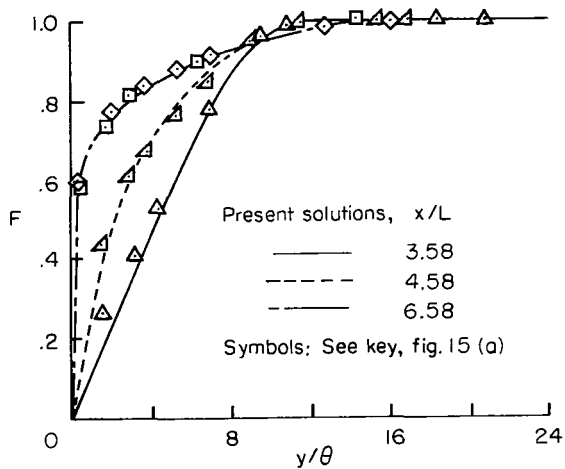
(c) $R_e = 1.89 \times 10^7$ per meter.
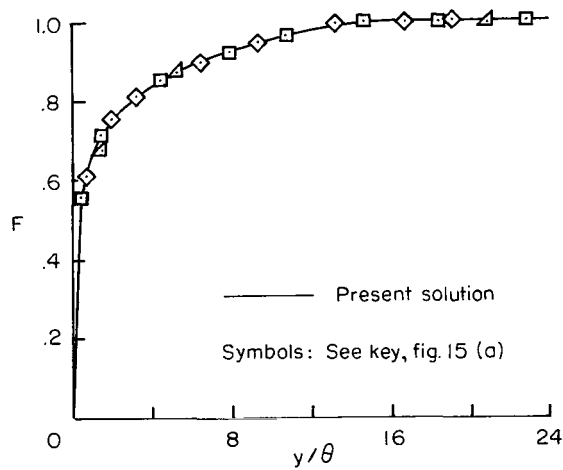
(d) $R_e = 2.835 \times 10^7$ per meter.

Figure 15.- Comparisons with velocity profile data and momentum thickness for laminar, transitional, and turbulent flow over a hollow cylinder at $M_\infty = 2.41$. $L = 2.54$ cm.
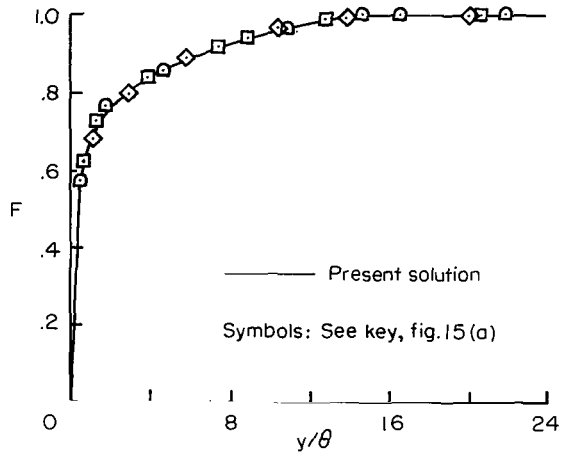
(e)  $R_e = 3.773 \times 10^7$ per meter.
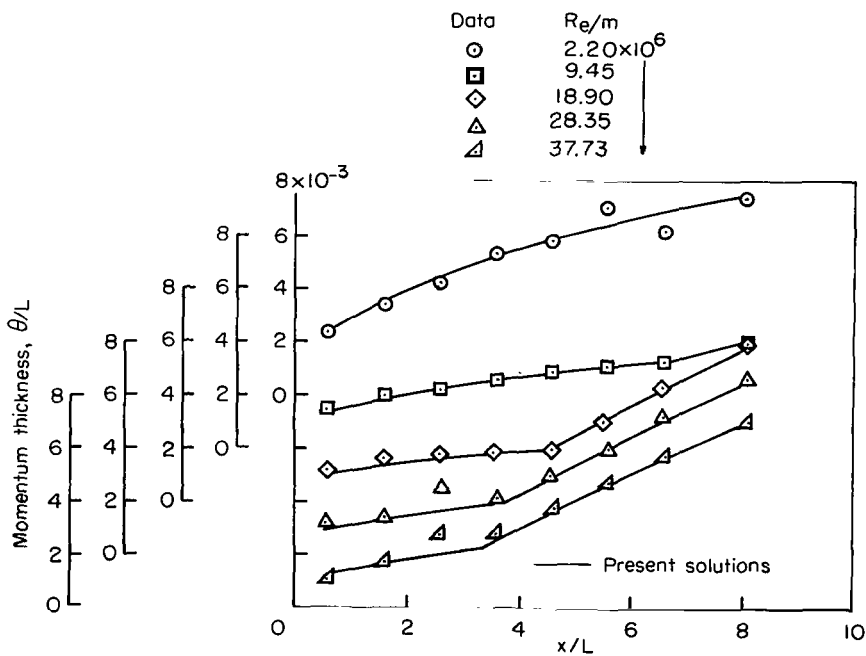


(f) Momentum thickness.

Figure 15.- Concluded.

numbers of $9.45 \times 10^6$ per meter and $1.89 \times 10^7$ per meter, laminar, transitional, and turbulent flow occurred. (See figs. 15(b) and 15(c).) For unit Reynolds numbers of $2.835 \times 10^7$ per meter and $3.773 \times 10^7$ per meter, the flow was turbulent as presented in figures 15(d) and 15(e), respectively. The experimental and calculated turbulent profiles are similar. Comparisons with the experimental momentum thicknesses are presented in figure 15(f). The agreement is good over the entire unit Reynolds number range.

<div align="center">Flat-Plate Hypersonic Flow</div>

A final example of laminar and transitional boundary-layer flow for hypersonic test conditions is presented in figure 16. These data were obtained by Johnson (ref. 97) on a sharp-leading-edge flat-plate model. The experimental test conditions were as follows:

$$M_\infty = 7.8$$

$$p_{t,\infty} = 4.226 \ MN/m^2$$

$$T_{t,\infty} = 794.4 \ K$$

$$\frac{T_w}{T_{t,\infty}} = 0.388$$

The agreement between the numerical results and the experimental Stanton number distribution is very good provided the experimental transition location is used as an input quantity. The transition extent was calculated from equation (63). (Note that the transition from laminar to turbulent flow was not completed; that is, $x_{t,f}$ was not located on
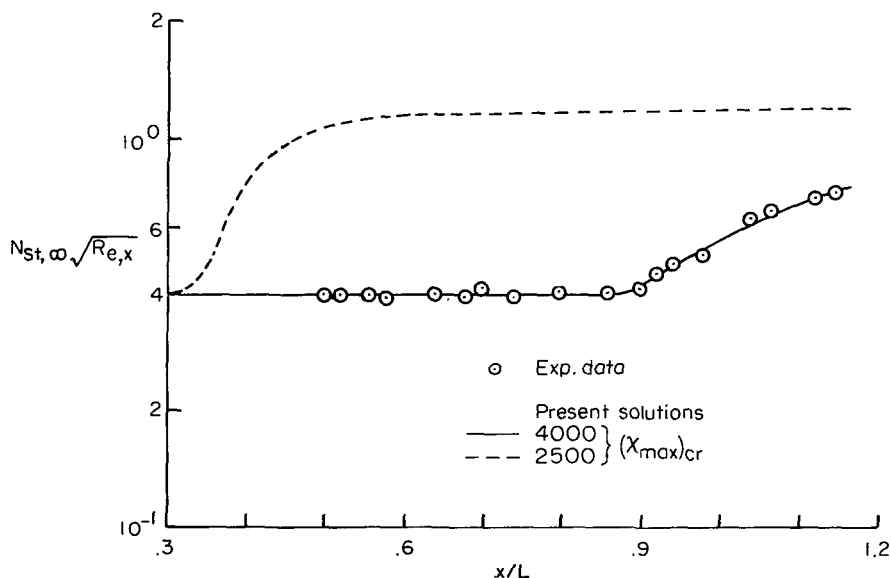


Figure 16.- Comparison with experimental data for laminar and transitional flat-plate flow at $M_\infty = 7.8$. $L = 30.48$ cm.

the model.)  The total number of grid points in the $\eta$-direction and the grid-point-spacing parameter $K$ were assigned values of 201 and 1.04, respectively.  The computer processing time was approximately 2 minutes.

This particular test case is presented to emphasize the fact that the stability index $(\chi_{max})_{cr}$ is not an invariant as originally suggested by Rouse (ref. 69) but is, in fact, a strong function of the unit Reynolds number.  For all the previous test cases presented herein, $(\chi_{max})_{cr}$ has varied over a relatively small range, $2500 \leqq (\chi_{max})_{cr} \leqq 3000$ which might lead one to the erroneous conclusion that, although not invariant, $(\chi_{max})_{cr}$ varies only slightly.  However, the present flat-plate test case value of $(\chi_{max})_{cr} = 4000$ clearly extends the range from 2500 to 4000.  The numerical results obtained by assuming that transition would occur at the x-station where $\chi_{max}$ equaled 2500 are presented in figure 16.  These results indicate that no assumption concerning the location of experimental transition should be made on the basis of the magnitude of the stability index as being an invariant or a near constant.  An area of interest concerning the possibility of using $\chi_{max}$ as a transition correlation parameter would be to apply the present numerical method to particular classes of flow over a broad range of test conditions; for example, boundary-layer flows with nonsimilar wall boundary conditions, flows with pressure gradient histories, and similar flows where experimental transition data are available.  From these systematic calculations, one could determine the possibility of using $\chi_{max}$ as a guide for predicting transition.  (See ref. 23.)

## CONCLUDING REMARKS

A system of equations which govern the mean flow properties of laminar, transitional, and turbulent compressible boundary layers for either planar or axisymmetric flows and a numerical method by which the system can be accurately solved has been presented.

The turbulent boundary layer was treated by a two-layer concept with appropriate eddy viscosity models for each layer to replace the Reynolds stress terms.  A specifiable turbulent Prandtl number replaces the turbulent heat flux term.  A constant static turbulent Prandtl number equal to 0.9 was used in the present solutions; however, the numerical procedure is completely general and any functional relation may be used.

The mean flow properties of the transitional boundary layer were calculated by multiplying the eddy viscosity by an intermittency function based on the statistical production and growth of the turbulent spots.  The intermittency function represents the fraction of time that any given streamwise station experiences turbulent flow or the probability at any given instant of time that a specific point will be engulfed in a turbulent spot.

The numerical method used to solve the system of equations was a three-point implicit finite-difference scheme for variable grid-point spacing in both spatial coordinates. The method is self starting; that is, it requires no experimental data input except the empirical or experimental location and extent of transition. The momentum and energy equations remain coupled and are solved simultaneously without iteration. The technique is inherently stable provided the eddy viscosity distribution is properly treated; that is, no constraint is placed on the grid-point spacing by a step-size stability parameter such as in the case of explicit finite-difference schemes. The method is highly efficient with regard to flexibility, digital computer processing time, and accuracy.

A number of test cases have been compared with experimental data for supersonic and hypersonic flows over planar and axisymmetric geometries. These test cases included laminar, transitional, and turbulent boundary-layer flows with both favorable and unfavorable pressure gradient histories. Mass flux at the wall and transverse curvature effects were also considered. Excellent agreement between the numerical results and experimental data was obtained for all test cases. However, low Reynolds number and high Mach number turbulent flows, supersonic flows with large favorable or unfavorable pressure gradient histories, and flows with large longitudinal curvature have not been considered. The omission of these particular classes of flow was deliberate and was done for two reasons: (1) to minimize the empiricism contained in the eddy viscosity and eddy conductivity models and (2) the lack of accurate, well-documented data for these classes of flow. Advances in the state of the art of formulating turbulent transport models which contain low Reynolds number effects, pressure gradient effects, and longitudinal curvature effects can be directly applied with little or no effort to the technique presented herein as they become available.

Langley Research Center,
    National Aeronautics and Space Administration,
        Hampton, Va., June 21, 1971.

APPENDIX A

DIFFERENCE RELATIONS

Three-point implicit difference relations are used to reduce the transformed
momentum and energy equations (eqs. (26) and (27)) to finite-difference form. It is
assumed that all data are known at the solution stations $m - 1$ and $m$. (See fig. 7.)
One then wishes to obtain the unknown quantities at the grid points for the $m + 1$ station.
In the following development, the notations $G$ and $H$ are utilized to represent any
typical variable.

Taylor series expansions are first written about the unknown grid point $(m + 1, n)$
in the $\xi$-direction as follows:

$$G_{m,n} = G_{m+1,n} - \Delta\xi_2\left(G_\xi\right)_{m+1,n} + \frac{\Delta\xi_2^2}{2}\left(G_{\xi\xi}\right)_{m+1,n} - \frac{\Delta\xi_2^3}{6}\left(G_{\xi\xi\xi}\right)_{m+1,n} + \ldots \tag{A1a}$$

and

$$G_{m-1,n} = G_{m+1,n} - \left(\Delta\xi_1 + \Delta\xi_2\right)\left(G_\xi\right)_{m+1,n} + \frac{\left(\Delta\xi_1 + \Delta\xi_2\right)^2}{2}\left(G_{\xi\xi}\right)_{m+1,n}$$

$$- \frac{\left(\Delta\xi_1 + \Delta\xi_2\right)^3}{6}\left(G_{\xi\xi\xi}\right)_{m+1,n} + \ldots \tag{A1b}$$

where subscript notation has been utilized to denote differentiation; that is, $G_\xi \equiv (\partial G/\partial\xi)$,
and so forth.

Equations (A1a) and (A1b) can be solved to yield

$$\left(\frac{\partial G}{\partial\xi}\right)_{m+1,n} = \frac{X_1 G_{m+1,n} - X_2 G_{m,n} + X_3 G_{m-1,n}}{2\Delta\xi_2} + \frac{\Delta\xi_2\left(\Delta\xi_1 + \Delta\xi_2\right)}{6}G_{\xi\xi\xi} + \ldots \tag{A2}$$

and

$$G_{m+1,n} = X_4 G_{m,n} - X_5 G_{m-1,n} + \frac{\Delta\xi_1\Delta\xi_2}{2}\left(1 + \frac{\Delta\xi_2}{\Delta\xi_1}\right)G_{\xi\xi} + \ldots \tag{A3}$$

Terms of the order $\Delta\xi_1\Delta\xi_2$ or smaller are neglected. This procedure produces trun-
cation errors of the order $\Delta\xi_1\Delta\xi_2$ instead of $\Delta\xi_2$ as in reference 29 where two-point
difference relations are used. The $X_1, X_2, \ldots, X_5$ coefficients appearing in equa-
tions (A2) and (A3) are defined as follows:

$$X_1 = 2 \frac{\Delta \xi_1 + 2 \Delta \xi_2}{\Delta \xi_1 + \Delta \xi_2} \tag{A4}$$

$$X_2 = 2 \frac{\Delta \xi_1 + \Delta \xi_2}{\Delta \xi_1} \tag{A5}$$

$$X_3 = 2 \frac{\Delta \xi_1 \Delta \xi_2}{\Delta \xi_1 (\Delta \xi_1 + \Delta \xi_2)} \tag{A6}$$

$$X_4 = \frac{\Delta \xi_1 + \Delta \xi_2}{\Delta \xi_1} \tag{A7}$$

$$X_5 = \frac{\Delta \xi_2}{\Delta \xi_1} \tag{A8}$$

Taylor series expansions are next written about the unknown grid point $(m + 1, n)$ in the $\eta$-direction as follows:

$$G_{m+1,n+1} = G_{m+1,n} + \Delta \eta_n (G_\eta)_{m+1,n} + \frac{\Delta \eta_n^2}{2}(G_{\eta\eta})_{m+1,n} + \frac{\Delta \eta_n^3}{6}(G_{\eta\eta\eta})_{m+1,n} + \cdots \tag{A9a}$$

$$G_{m+1,n-1} = G_{m+1,n} - \Delta \eta_{n-1} (G_\eta)_{m+1,n} + \frac{\Delta \eta_{n-1}^2}{2}(G_{\eta\eta})_{m+1,n} - \frac{\Delta \eta_{n-1}^3}{6}(G_{\eta\eta\eta})_{m+1,n} + \cdots \tag{A9b}$$

Equations (A9a) and (A9b) can be solved to yield

$$\left(\frac{\partial^2 G}{\partial \eta^2}\right)_{m+1,n} = Y_1 G_{m+1,n+1} - Y_2 G_{m+1,n} + Y_3 G_{m+1,n-1} + \frac{(\Delta \eta_{n-1} - \Delta \eta_n)}{3} G_{\eta\eta\eta} + \cdots \tag{A10}$$

and

$$\left(\frac{\partial G}{\partial \eta}\right)_{m+1,n} = Y_4 G_{m+1,n+1} - Y_5 G_{m+1,n} - Y_6 G_{m+1,n-1} - \frac{\Delta \eta_n \Delta \eta_{n-1}}{6} G_{\eta\eta\eta} + \cdots \tag{A11}$$

The $Y_1, Y_2, \ldots, Y_6$ coefficients appearing in equations (A10) and (A11) are defined as follows:

$$Y_1 = \frac{2}{\Delta \eta_n (\Delta \eta_n + \Delta \eta_{n-1})} \tag{A12}$$

$$Y_2 = \frac{2}{\Delta\eta_n \, \Delta\eta_{n-1}} \cdot \tag{A13}$$

$$Y_3 = \frac{2}{\Delta\eta_{n-1}(\Delta\eta_n + \Delta\eta_{n-1})} \tag{A14}$$

$$Y_4 = \frac{\Delta\eta_{n-1}}{\Delta\eta_n(\Delta\eta_n + \Delta\eta_{n-1})} \tag{A15}$$

$$Y_5 = \frac{\Delta\eta_{n-1} - \Delta\eta_n}{\Delta\eta_n \, \Delta\eta_{n-1}} \tag{A16}$$

$$Y_6 = \frac{\Delta\eta_n}{\Delta\eta_{n-1}(\Delta\eta_n + \Delta\eta_{n-1})} \tag{A17}$$

For the case of equally spaced grid points in the $\xi$ and $\eta$ coordinates, equations (A4) to (A8) and (A12) to (A17) reduce to the following relations:

$$\left. \begin{aligned} X_1 &= 3 \\ X_2 &= 4 \\ X_3 &= 1 \\ X_4 &= 2 \\ X_5 &= 1 \end{aligned} \right\} \tag{A18a}$$

and

$$\left. \begin{aligned} Y_1 &= \frac{1}{\Delta\eta^2} \\ Y_2 &= 2Y_1 \\ Y_3 &= Y_1 \\ Y_4 &= \frac{1}{2\,\Delta\eta} \\ Y_5 &= 0 \\ Y_6 &= Y_4 \end{aligned} \right\} \tag{A18b}$$

where $\Delta\xi$ and $\Delta\eta$ represent the spacing between the grid points in the $\xi$ and $\eta$ coordinates, respectively.

APPENDIX A — Continued

Equations (A2), (A3), (A10), and (A11) can then be written for constant grid-point spacing as follows:

$$\left(\frac{\partial G}{\partial \xi}\right)_{m+1,n} = \frac{3G_{m+1,n} - 4G_{m,n} + G_{m-1,n}}{2\Delta\xi} + \frac{\Delta\xi^2}{3}G_{\xi\xi\xi} + \ldots \tag{A19}$$

$$G_{m+1,n} = 2G_{m,n} - G_{m-1,n} + \Delta\xi^2 G_{\xi\xi} + \ldots \tag{A20}$$

$$\left(\frac{\partial^2 G}{\partial \eta^2}\right)_{m+1,n} = \frac{G_{m+1,n+1} - 2G_{m+1,n} + G_{m+1,n-1}}{\Delta\eta^2} - \frac{\Delta\eta^2}{12}G_{\eta\eta\eta\eta} + \ldots \tag{A21}$$

$$\left(\frac{\partial G}{\partial \eta}\right)_{m+1,n} = \frac{G_{m+1,n+1} - G_{n+1,n-1}}{2\Delta\eta} - \frac{\Delta\eta^2}{6}G_{\eta\eta\eta} + \ldots \tag{A22}$$

Equations (A19) to (A22) are recognized as the standard relations for equally spaced grid points. (See, for example, ref. 30.)

Quantities of the form $\left(G\frac{\partial H}{\partial \xi}\right)$ that appear in the governing equations must be linearized in order to obtain a system of linear difference equations. Quantities of this type are linearized by using equations (A2) and (A3); that is,

$$\left(G\frac{\partial H}{\partial \xi}\right)_{m+1,n} = \left(X_4 G_{m,n} - X_5 G_{m-1,n}\right)\frac{\left(X_1 H_{m+1,n} - X_2 H_{m,n} + X_3 H_{m-1,n}\right)}{2\Delta\xi_2} + O\left(\Delta\xi_1\ \Delta\xi_2\right) \tag{A23}$$

The procedure used to linearize nonlinear products such as $(\partial G/\partial\eta)(\partial H/\partial\eta)$ is the same as that used by Flügge-Lotz and Blottner (ref. 29) and is as follows:

$$\left[\left(\frac{\partial G}{\partial\eta}\right)\left(\frac{\partial H}{\partial\eta}\right)\right]_{m+1,n} = \left(\frac{\partial G}{\partial\eta}\right)_{m,n}\left(\frac{\partial H}{\partial\eta}\right)_{m+1,n} - \left(\frac{\partial G}{\partial\eta}\right)_{m,n}\left(\frac{\partial H}{\partial\eta}\right)_{m,n} + \left(\frac{\partial H}{\partial\eta}\right)_{m,n}\left(\frac{\partial G}{\partial\eta}\right)_{m+1,n} \tag{A24}$$

where the terms $\left(\frac{\partial G}{\partial\eta}\right)_{m,n}$ and $\left(\frac{\partial H}{\partial\eta}\right)_{m,n}$ are evaluated from equation (A11), but at the known station m. By equating G to H in equation (A24), the linearized form for quantities of the type $\left(\frac{\partial G}{\partial\eta}\right)^2$ is obtained; that is,

$$\left(\frac{\partial G}{\partial \eta}\right)^2_{m+1,n} = \left(\frac{\partial G}{\partial \eta}\right)_{m,n}\left[2\left(\frac{\partial G}{\partial \eta}\right)_{m+1,n} - \left(\frac{\partial G}{\partial \eta}\right)_{m,n}\right] \tag{A25}$$

where $\left(\dfrac{\partial G}{\partial \eta}\right)_{m+1,n}$ is obtained from equation (A22).

The preceding relations for the difference quotients produce linear difference equations (eqs. (66) and (67)) when substituted into the governing differential equations for the conservation of momentum (eq. (26)) and energy (eq. (27)), respectively, since terms of order $(\Delta \xi)^2$ are neglected.

COEFFICIENTS FOR DIFFERENCE EQUATIONS

Equations (66) and (67) are the difference equations used to represent the partial differential equations for the conservation of momentum and energy, respectively. These equations are repeated for convenience as follows:

$$A_n^{(1)} F_{m+1,n-1} + B_n^{(1)} F_{m+1,n} + C_n^{(1)} F_{m+1,n+1} + D_n^{(1)} \Theta_{m+1,n-1}$$

$$+ E_n^{(1)} \Theta_{m+1,n} + F_n^{(1)} \Theta_{m+1,n+1} = G_n^{(1)} \tag{B1}$$

$$A_n^{(2)} F_{m+1,n-1} + B_n^{(2)} F_{m+1,n} + C_n^{(2)} F_{m+1,n+1} + D_n^{(2)} \Theta_{m+1,n-1}$$

$$+ E_n^{(2)} \Theta_{m+1,n} + F_n^{(2)} \Theta_{m+1,n+1} = G_n^{(2)} \tag{B2}$$

These equations are obtained from equations (26) and (27) and the difference quotients presented in appendix A. The coefficients $A_n^{(1)}$, $B_n^{(1)}$, and so forth, in equations (B1) and (B2) are functions of known quantities evaluated at stations $m$ and $m-1$. (See fig. 7.) Therefore, equations (B1) and (B2) can be solved simultaneously without iterative procedures. The coefficients are as follows:

$$A_n^{(1)} = Y_3 H_3 - Y_6 H_{11} \tag{B3}$$

$$B_n^{(1)} = X_1 H_1 - Y_2 H_3 - Y_5 H_{11} + H_5 \tag{B4}$$

$$C_n^{(1)} = Y_1 H_3 + Y_4 H_{11} \tag{B5}$$

$$D_n^{(1)} = -Y_6 H_4 F_Y \tag{B6}$$

$$E_n^{(1)} = \frac{Y_5}{Y_6} D_n^{(1)} + H_6 \tag{B7}$$

$$F_n^{(1)} = -\frac{Y_4}{Y_6} D_n^{(1)} \tag{B8}$$

$$G_n^{(1)} = H_1 F_{m2} + H_4 T_Y F_Y \tag{B9}$$

$$A_n^{(2)} = -2Y_6 H_8 F_Y \tag{B10}$$

$$B_n^{(2)} = \frac{Y_5}{Y_6} A_n^{(2)} \tag{B11}$$

$$C_n^{(2)} = -\frac{Y_4}{Y_6} A_n^{(2)} \tag{B12}$$

$$D_n^{(2)} = Y_3 H_{10} - Y_6 H_{12} \tag{B13}$$

$$E_n^{(2)} = X_1 H_1 - Y_2 H_{10} - Y_5 H_{12} \tag{B14}$$

$$F_n^{(2)} = Y_1 H_{10} + Y_4 H_{12} \tag{B15}$$

$$G_n^{(2)} = H_1 T_{m2} + H_8 (F_Y)^2 + H_9 (T_Y)^2 \tag{B16}$$

The coefficients $Y_1, Y_2, \ldots, Y_6$, $X_1, \ldots, X_5$, etc., are functions of the grid-point spacing and are defined in equations (A12) to (A17) and (A4) to (A8), respectively. The coefficients $H_1$, $H_2$, . . . are defined as follows:

$$H_1 = \xi_{m+1} F_{m1} \frac{FT}{\Delta \xi_2} \tag{B17}$$

$$H_2 = V_{m1} - L_{m1}\left(\overline{E}_{m1} C'_{m1} + \overline{E}'_{m1} C_{m1}\right) \tag{B18}$$

$$H_3 = -\overline{E}_{m1} L_{m1} C_{m1} \tag{B19}$$

$$H_4 = H_3 \frac{L'_{m1}}{L_{m1}} \tag{B20}$$

$$H_5 = \beta_{m+1} F_{m1} \tag{B21}$$

$$H_6 = -\beta_{m+1} \tag{B22}$$

$$H_7 = V_{m1} - L_{m1}\left(\hat{E}_{m1} C'_{m1} + \hat{E}'_{m1} C_{m1}\right) \tag{B23}$$

$$H_8 = -\alpha_{m+1} L_{m1} \overline{E}_{m1} C_{m1} \tag{B24}$$

$$H_9 = -\hat{E}_{m1}L'_{m1}C_{m1} \qquad (B25)$$

$$H_{10} = H_9 \frac{L_{m1}}{L'_{m1}} \qquad (B26)$$

$$H_{11} = H_2 + H_4 T_Y \qquad (B27)$$

$$H_{12} = H_7 + 2H_9 T_Y \qquad (B28)$$

The undefined quantities appearing in equations (B17) to (B28) are defined as follows:

$$F_{m1} = X_4 F_{m,n} - X_5 F_{m-1,n} \qquad (B29)$$

$$T_{m1} = X_4 \Theta_{m,n} - X_5 \Theta_{m-1,n} \qquad (B30)$$

$$V_{m1} = X_4 V_{m,n} - X_5 V_{m-1,n} \qquad (B31)$$

$$F_{m2} = X_2 F_{m,n} - X_3 F_{m-1,n} \qquad (B32)$$

$$T_{m2} = X_2 \Theta_{m,n} - X_3 \Theta_{m-1,n} \qquad (B33)$$

$$L_{m1} = \sqrt{T_{m1}} \; \frac{1 + \left(\dfrac{S}{T_e}\right)_{m+1}}{T_{m1} + \left(\dfrac{S}{T_e}\right)_{m+1}} \qquad \text{(Air only)} \qquad (B34)$$

$$L'_{m1} = \frac{L_{m1}}{2T_{m1}} \left[ \frac{\left(\dfrac{S}{T_e}\right)_{m+1} - T_{m1}}{\left(\dfrac{S}{T_e}\right)_{m+1} + T_{m1}} \right] \qquad \text{(Air only)} \qquad (B35)$$

$$\overline{E}_{m1} = \left(\bar{\epsilon}_{av}\right)_{m+1,n} \qquad \text{(See eq. (74))} \qquad . \qquad (B36)$$

$$\hat{E}_{m1} = \frac{\left(\hat{\epsilon}_{av}\right)_{m+1,n}}{N_{Pr}} \qquad (B37)$$

$$\overline{E}_Y = Y_4 \overline{\epsilon}_{m,n+1} - Y_5 \overline{\epsilon}_{m,n} - Y_6 \overline{\epsilon}_{m,n-1} \qquad \text{(See eq. (A11))} \qquad \text{(B38)}$$

$$\hat{E}_Y = Y_4 \hat{\epsilon}_{m,n+1} - Y_5 \hat{\epsilon}_{m,n} - Y_6 \hat{\epsilon}_{m,n-1} \qquad \text{(B39)}$$

$$F_Y = Y_4 F_{m,n+1} - Y_5 F_{m,n} - Y_6 F_{m,n-1} \qquad \text{(B40)}$$

$$T_Y = Y_4 \Theta_{m,n+1} - Y_5 \Theta_{m,n} - Y_6 \Theta_{m,n-1} \qquad \text{(B41)}$$

$$\beta_{m+1} = \left( \frac{2\xi}{u_e} \frac{du_e}{d\xi} \right)_{m+1} \qquad \text{(See eq. (28))} \qquad \text{(B42)}$$

$$\alpha_{m+1} = \left( \frac{u_e^2}{T_e} \right)_{m+1} \qquad \text{(B43)}$$

The transverse curvature terms are contained in the quantities $C_{m1}$ and $C'_{m1}$ which appear explicitly in the $H_2$, $H_3$, $H_7$, $H_8$, and $H_9$ coefficients. The transverse curvature term in the transformed plane (see eq. (30)) may be written as follows:

$$t^{2j} = 1 + \frac{2j(W)\sqrt{2\xi}\,\cos\phi}{\rho_e u_e} \int_0^{\eta} \Theta \, d\eta \qquad \text{(B44)}$$

where $t$ represents the ratio $r/r_0$ and is a known quantity for the $N - 1$ grid points at station $m - 1$ and $m$. Then, the extrapolated values at $m + 1, n$ are obtained as follows where the parameter $C$ is used to represent $t^{2j}$:

$$C_{m1} = X_4 C_{m,n} - X_5 C_{m-1,n} \qquad \text{(B45)}$$

$$C'_{m1} = Y_4 C_{m,n+1} - Y_5 C_{m,n} - Y_6 C_{m,n-1} \qquad \text{(B46)}$$

Two quantities (symbols) as of now remain undefined. These are the code symbols FT and W which appear in equations (B17) and (B44), respectively. The code symbol W appearing in equation (B44) is used to either retain or neglect the transverse curvature terms for axisymmetric flows; that is, $W = 1$ or $0$, respectively. For planar flows, the transverse curvature term does not appear since $j$ equals 0. The code symbol FT (flow type) appearing in equation (B17) is used to either retain or neglect the nonsimilar terms in the governing differential equations; that is, $FT = 1$ or $0$, respectively. If FT is assigned a value of unity, the solution to the nonsimilar equations

75

(eqs. (25) to (27)) is obtained. If FT is assigned a value of zero, the locally similar solution is obtained; that is, the following system of equations are solved:

Continuity:

$$\frac{\partial V}{\partial \eta} + F = 0 \tag{B47}$$

Momentum:

$$V \frac{\partial F}{\partial \eta} - \frac{\partial}{\partial \eta}\left(t^{2j} l \bar{\epsilon} \frac{\partial F}{\partial \eta}\right) + \beta\left(F^2 - \Theta\right) = 0 \tag{B48}$$

Energy:

$$V \frac{\partial \Theta}{\partial \eta} - \frac{\partial}{\partial \eta}\left(t^{2j} l \frac{\hat{\epsilon}}{N_{Pr}} \frac{\partial \Theta}{\partial \eta}\right) - \alpha l t^{2j} \bar{\epsilon}\left(\frac{\partial F}{\partial \eta}\right)^2 = 0 \tag{B49}$$

The governing equations for the locally similar system are obtained from equations (25) to (27) by neglecting derivatives of the dependent variables F, $\Theta$, and V with respect to the streamwise coordinate $\xi$. The capability of obtaining locally similar solutions is desirable in that for a given test case the locally similar and completely nonsimilar solutions can be obtained for the identical program inputs and numerical procedures. Consequently, the effects of the nonsimilar terms on the boundary-layer characteristics for a particular case can be determined by direct comparison of the results obtained for solutions for FT = 1 and FT = 0, respectively.

# REFERENCES

1. Prandtl, L.: Über Flüssigkeitsbewegung bei sehr kleiner Reibung. Verh. des III. Int. Math-Kong., Heidelberg, B. G. Teubner (Leipzig), 1904, pp. 484-491.

2. Schlichting, Hermann (J. Kestin, Transl.): Boundary-Layer Theory. Sixth ed., McGraw-Hill Book Co., 1968.

3. Moore, F. K., ed.: Hypersonic Boundary Layer Theory. Theory of Laminar Flows. Vol. IV of High Speed Aerodynamics and Jet Propulsion, F. K. Moore, ed., Princeton Univ. Press, 1964, pp. 439-527.

4. Rosenhead, L., ed.: Laminar Boundary Layers. Clarendon Press (Oxford), 1963.

5. Dewey, C. Forbes, Jr.; and Gross, Joseph F.: Exact Similar Solutions of the Laminar Boundary-Layer Equations. Mem. RM-5089-ARPA (Contract No. DAH15 67 C 0141), Rand Corp., July 1967. (Available from DDC as AD 665 969.)

6. Blottner, F. G.: Finite Difference Methods of Solution of the Boundary-Layer Equations. AIAA J., vol. 8, no. 2, Feb. 1970, pp. 193-205.

7. Tani, Itiro; and Hama, Francis R.: Some Experiments on the Effect of a Single Roughness Element on Boundary-Layer Transition. J. Aeronaut. Sci., vol. 20, no. 4, Apr. 1953, pp. 289-290.

8. Mitchner, Morton: Propagation of Turbulence From an Instantaneous Point Disturbance. J. Aeronaut. Sci., vol. 21, no. 5, May 1954, pp. 350-351.

9. Schubauer, G. B.; and Klebanoff, P. S.: Contributions on the Mechanics of Boundary-Layer Transition. NACA Rep. 1289, 1956. (Supersedes NACA TN 3489.)

10. James, Carlton S.: Observations of Turbulent-Burst Geometry and Growth in Supersonic Flow. NACA TN 4235, 1958.

11. Săvulescu, St. N.: Tranzitia de la Scurgerea Laminara la Cea Turbulenta. Editura Academiei Republicii Socialiste România, 1968.

12. Morkovin, Mark V.: Critical Evaluation of Transition From Laminar to Turbulent Shear Layers With Emphasis on Hypersonically Traveling Bodies. AFFDL-TR-68-149, U.S. Air Force, Mar. 1969. (Available from DDC as AD 686 178.)

13. Mack, Leslie M.; and Morkovin, Mark V.: High Speed Boundary-Layer Stability and Transition. AIAA Professional Study Series, 1969.

14. Kline, S. J.; Morkovin, M. V.; Sovran, G.; and Cockrell, D. J., eds.: Computation of Turbulent Boundary Layers — 1968 AFOSR-IFP-Stanford Conference. Vol. I — Methods, Predictions, Evaluation and Flow Structure. Stanford Univ., c.1969.

15. Coles, D. E.; and Hirst, E. A., eds.: Computation of Turbulent Boundary Layers —
    1968 AFOSR-IFP-Stanford Conference. Vol. II — Compiled Data. Stanford Univ.,
    c.1969.

16. Anon.: Compressible Turbulent Boundary Layers. NASA SP-216, 1969.

17. Beckwith, Ivan E.: Recent Advances in Research on Compressible Turbulent Bound-
    ary Layers. Analytic Methods in Aircraft Aerodynamics, NASA SP-228, 1970,
    pp. 355-416.

18. Persh, Jerome: A Procedure for Calculating the Boundary-Layer Development in
    the Region of Transition From Laminar to Turbulent Flow. NAVORD Rep. 4438,
    U.S. Navy, Mar. 19, 1957. (Available from DDC as AD 131 947.)

19. Weber, H. E.: Turbulent and Transition Boundary Layer Based on Mixing Length
    and Intermittency. Paper 68-FE-52, Amer. Soc. Mech. Eng., May 1968.

20. Emmons, H. W.: The Laminar-Turbulent Transition in a Boundary Layer — Pt. I.,
    J. Aeronaut. Sci., vol. 18, no. 7, July 1951, pp. 490-498.

21. Masaki, M.; and Yakura, J. K.: Transitional Boundary Layer Considerations for the
    Heating Analyses of Lifting Reentry Vehicles. AIAA Paper No. 68-1155, Dec. 1968.

22. Martellucci, A.; Rie, H.; and Sontowski, J. F.: Evaluation of Several Eddy Viscosity
    Models Through Comparison With Measurements in Hypersonic Flows. AIAA
    Paper No. 69-688, June 1969.

23. Harris, Julius Elmore: Numerical Solution of the Compressible Laminar, Transi-
    tional, and Turbulent Boundary Layer Equations With Comparisons to Experimental
    Data. Ph. D. Thesis, Virginia Polytech. Inst., May 1970.

24. Adams, John C., Jr.: Eddy Viscosity-Intermittency Factor Approach to Numerical
    Calculation of Transitional Heating on Sharp Cones in Hypersonic Flow.
    AEDC-TR-70-210, U.S. Air Force, Nov. 1970.

25. Kuhn, Gary D.: Calculation of Compressible, Nonadiabatic Boundary Layers in
    Laminar, Transitional and Turbulent Flow by the Method of Integral Relations.
    NASA CR-1797, 1970.

26. Fish, R. W.; and McDonald, H.: Practical Calculations of Transitional Boundary
    Layers. Rep. UAR-H48, United Aircraft Corp., Mar. 14, 1969.

27. Glushko, G. S.: Turbulent Boundary Layer on a Flat Plate in an Incompressible
    Fluid. Bull. Acad. Sci. USSR, Mech. Ser., no. 4, 1965, pp. 13-23.

28. Donaldson, Coleman duP.; and Rosenbaum, Harold: Calculation of Turbulent Shear
    Flows Through Closure of the Reynolds Equations by Invariant Modeling. Rep.
    No. 127, Aeronaut. Res. Assoc. Princeton, Inc., Dec. 1968.

29. Flügge-Lotz, I.; and Blottner, F. G.: Computation of the Compressible Laminar Boundary-Layer Flow Including Displacement-Thickness Interaction Using Finite-Difference Methods. AFOSR 2206, U.S. Air Force, Jan. 1962.

30. Davis, R. T.; and Flügge-Lotz, I.: Laminar Compressible Flow Past Axisymmetric Blunt Bodies (Results of a Second-Order Theory). Tech. Rep. No. 143 (Grants AF-AFOSR-62-242 and AF-AFOSR-235-63), Div. Eng. Mech., Stanford Univ., Dec. 1963.

31. Reynolds, Osborne: An Experimental Investigation of the Circumstances Which Determine Whether the Motion of Water in Parallel Channels Shall be Direct or Sinuous and of the Law of Resistance in Parallel Channels. Phil. Trans. Roy. Soc. London, vol. 174, 1883, pp. 935-982.

32. Van Driest, E. R.: Turbulent Boundary Layer in Compressible Fluids. J. Aeronaut. Sci., vol. 18, no. 3, Mar. 1951, pp. 145-160, 216.

33. Bushnell, Dennis M.; and Beckwith, Ivan E.: Calculation of Nonequilibrium Hypersonic Turbulent Boundary Layers and Comparisons With Experimental Data. AIAA J., vol. 8, no. 8, Aug. 1970, pp. 1462-1469.

34. Probstein, Ronald F.; and Elliott, David: The Transverse Curvature Effect in Compressible Axially Symmetric Laminar Boundary-Layer Flow. J. Aeronaut. Sci., vol. 23, no. 3, Mar. 1956, pp. 208-224, 236.

35. Hayes, Wallace D.; and Probstein, Ronald F.: Hypersonic Flow Theory. Academic Press, Inc., 1959.

36. Bradshaw, P.: Turbulent Boundary Layers. Aeronaut. J., vol. 72, no. 689, May 1968, pp. 451-458.

37. Prandtl, L.: Report on Investigation of Developed Turbulence. NACA TM 1231, 1949.

38. Van Driest, E. R.: On Turbulent Flow Near a Wall. J. Aeronaut. Sci., vol. 23, no. 11, Nov. 1956, pp. 1007-1011.

39. Stokes, G. G.: On the Effect of the Internal Friction of Fluids on the Motion of Pendulums. Trans. Cambridge Phil. Soc., vol. IX, pt. II, 1851, pp. 8-106.

40. Bushnell, Dennis M.; and Morris, Dana J.: Shear Stress, Eddy Viscosity, and Mixing Length Distributions in Hypersonic Turbulent Boundary Layers. NASA TM X-2310, 1971.

41. Cebeci, Tuncer: Behavior of Turbulent Flow Near a Porous Wall With Pressure Gradient. AIAA J., vol. 8, no. 12, Dec. 1970, pp. 2152-2156.

42. Clauser, Francis H.: The Turbulent Boundary Layer. Vol. IV of Advances in Applied Mechanics, H. L. Dryden and Th. von Kármán, eds., Academic Press, Inc., 1956, pp. 1-51.

43. Maise, George; and McDonald, Henry: Mixing Length and Kinematic Eddy Viscosity in a Compressible Boundary Layer. AIAA J., vol. 6, no. 1, Jan. 1968, pp. 73-80.

44. Morkovin, Mark V.: Effects of Compressibility on Turbulent Flows. The Mechanics of Turbulence, Gordon & Breach, Sci. Publ., Inc., c.1964, pp. 367-380.

45. Matsui, Tatsuya: Mean Velocity Distribution in the Outer Layer of a Turbulent Boundary Layer. Res. Rep. No. 42 (Contract NONR 978(03)), Aerophys. Dep., Mississippi State Univ., Feb. 19, 1963.

46. Klebanoff, P. S.: Characteristics of Turbulence in a Boundary Layer With Zero Pressure Gradient. NACA Rep. 1247, 1955. (Supersedes NACA TN 3178.)

47. Kestin, J.; and Richardson, P. D.: Heat Transfer Across Turbulent Incompressible Boundary Layers. The Mechanics of Turbulence, Gordon & Breach, Sci. Publ., Inc., c.1964, pp. 409-418.

48. Johnson, Donald S.: Turbulent Heat Transfer in a Boundary Layer With Discontinuous Wall Temperature. Publ. No. 55 (OSR Tech. Note 55-289), Dep. Aeronaut., The Johns Hopkins Univ., Aug. 1955.

49. Rochelle, William C.: Prandtl Number Distribution in a Turbulent Boundary Layer With Heat Transfer at Supersonic Speeds. DRL-508 (Grants DA-ORD-31-124-61-G3 and DA-ORD(D)-31-124-G132), Univ. of Texas, Oct. 1963. (Available from DDC as AD 427 156.)

50. Simpson, R. L.; Whitten, D. G.; and Moffat, R. J.: An Experimental Study of the Turbulent Prandtl Number of Air With Injection and Suction. Int. J. Heat Mass Transfer, vol. 13, no. 1, Jan. 1970, pp. 125-143.

51. Rotta, J. C.: Heat Transfer and Temperature Distribution in Turbulent Boundary Layers at Supersonic and Hypersonic Flow. AGARDograph 97, Pt. I, May 1965, pp. 35-63.

52. Cebeci, Tuncer: A Model for Eddy-Conductivity and Turbulent Prandtl Number. Rep. No. MDC-J0747/01, McDonnell Douglas Corp., May 1970.

53. Jenkins, Rodman: Variation of the Eddy Conductivity With Prandtl Modulus and Its Use in Prediction of Turbulent Heat Transfer Coefficients. 1951 Heat Transfer and Fluid Mechanics Institute, Stanford Univ. Press, June 1951, pp. 147-158, 266-267.

54. Meier, H. U.; and Rotta, J. C.: Experimental and Theoretical Investigations of Temperature Distributions in Supersonic Boundary Layers. AIAA Paper No. 70-744, June-July 1970.

55. McDonald, H.: Mixing Length and Kinematic Eddy Viscosity in a Low Reynolds Number Boundary Layer. Rep. J214453-1, Res. Lab., United Aircraft Corp., Sept. 1970.

56. Simpson, Roger Lyndon: The Turbulent Boundary Layer on a Porous Plate: An Experimental Study of the Fluid Dynamics With Injection and Suction. Ph. D. Thesis, Stanford Univ., 1968.

57. Whitten, Derrill Gene: The Turbulent Boundary Layer on a Porous Plate: Experimental Heat Transfer With Variable Suction, Blowing and Surface Temperature. Ph. D. Thesis, Stanford Univ., 1968.

58. Lin, C. C.: On the Stability of Two-Dimensional Parallel Flows. Part I — General Theory. Quart. Appl. Math., vol. III, no. 2, July 1945, pp. 117-142.

59. Lin, C. C.: The Theory of Hydrodynamic Stability. Cambridge Univ. Press, 1955.

60. Jaffe, N. A.; Okamura, T. T.; and Smith, A. M. O.: Determination of Spatial Amplification Factors and Their Application to Predicting Transition. AIAA J., vol. 8, no. 2, Feb. 1970, pp. 301-308.

61. Fischer, Michael Carlton: An Experimental Investigation on Unit Reynolds Number and Bluntness Effects on Boundary-Layer Transition for a $10^{\circ}$ Half-Angle Cone at $M_{\infty} = 7$. M.S. Thesis, Virginia Polytech. Inst., June 1969.

62. Pate, S. R.; and Schueler, C. J.: Effects of Radiated Aerodynamic Noise on Model Boundary-Layer Transition in Supersonic and Hypersonic Wind Tunnels. AEDC-TR-67-236, U.S. Air Force, Mar. 1968. (Available from DDC as AD 666 644.)

63. Softley, E. J.; Graber, B. C.; and Zempel, R. E.: Transition of the Hypersonic Boundary Layer on a Cone: Pt. I — Experiments at $M_{\infty} = 12$ and 15. R67SD39 (Contract AF 04(694)-772), Missile Space Div., Gen. Elec. Co., Nov. 1967. (Available from DDC as AD 824 681.)

64. Richards, Bryan E.: Transitional and Turbulent Boundary Layers on a Cold Flat Plate in Hypersonic Flow. Aeronaut. Quart., vol. XVIII, Pt. 3, Aug. 1967, pp. 237-257.

65. Potter, J. Leith; and Whitfield, Jack D.: Boundary-Layer Transition Under Hypersonic Conditions. Recent Development in Boundary Layer Research, Pt. III, AGARDograph 97, May 1965, pp. 1-62.

66. Deem, Ralph E.; and Murphy, James S.: Flat Plate Boundary Layer Transition at Hypersonic Speeds. AIAA Paper No. 65-128, Jan. 1965.

67. Cary, Aubrey M., Jr.: Turbulent Boundary Layer Heat Transfer and Transition Measurements With Extreme Surface Cooling in Hypersonic Flow. M.A.E. Thesis, Univ. of Virginia, Aug. 1969.

68. Potter, J. Leith; and Whitfield, Jack D.: Effects of Slight Nose Bluntness and Roughness on Boundary-Layer Transition in Supersonic Flows. J. Fluid Mech., vol. 12, pt. 4, Apr. 1962, pp. 501-535.

69. Rouse, Hunter: A General Stability Index for Flow Near Plane Boundaries. J. Aeronaut. Sci., vol. 12, no. 4, Oct. 1945, pp. 429-431.

70. Van Driest, E. R.; and Blumer, C. B.: Boundary Layer Transition: Freestream Turbulence and Pressure Gradient Effects. AIAA J., vol. 1, no. 6, June 1963, pp. 1303-1306.

71. Ivensen, H. W.; and Hsu, Tao-Ting: A Local Reynolds Number to Predict Transition From Laminar to Turbulent Flow. Heat Transfer Thermodynamics and Education, Harold A. Johnson, ed., McGraw-Hill Book Co., Inc., 1964, pp. 207-212.

72. Stainback, P. Calvin: Use of Rouse's Stability Parameter in Determining the Critical Layer Height of a Laminar Boundary Layer. AIAA J., vol. 8, no. 1, Jan. 1970, pp. 173-175.

73. McCauley, William D., ed.: Boundary Layer Transition Study Group Meeting. Vol. III — Session on Ground Test Transition Data and Correlations. BSD-TR-67-213, Vol. III, U.S. Air Force, Aug. 1967.

74. McCauley, William D., ed.: Boundary Layer Transition Study Group Meeting. Vol. I — Session on Flight Test Transition Data and Correlations. BSD-TR-67-213, Vol. I, U.S. Air Force, Aug. 1967.

75. McCauley, William D., ed.: Boundary Layer Transition Study Group Meeting. Vol. II — Session on Boundary Layer Stability. BSD-TR-67-213, Vol. II, U.S. Air Force, Aug. 1967. (Available from DDC as AD 820 364.)

76. McCauley, William D., ed.: Boundary Layer Transition Study Group Meeting. Vol. IV — Session on Boundary Layer Transition Control. BSD-TR-67-213, Vol. IV, U.S. Air Force, Aug. 1967.

77. Dhawan, S.; and Narasimha, R.: Some Properties of Boundary Layer Flow During the Transition From Laminar to Turbulent Motion. J. Fluid Mech., vol. 3, pt. 4, Jan. 1958, pp. 418-436.

78. Corrsin, Stanley; and Kistler, Alan L.: Free-Stream Boundaries of Turbulent Flows. NACA Rep. 1244, 1955. (Supersedes NACA TN 3133.)

79. Fiedler, H.: Intermittency Distributions in Turbulent Wall Boundary Layers With and Without Pressure Gradients. NASA TT F-11,326, 1967.

80. Young, C. H.; Reda, D. C.; and Roberge, A. M.: Hypersonic Transitional and Turbulent Flow Studies on a Lifting Entry Vehicle. AIAA Paper No. 71-100, Jan. 1971.

81. Smith, A. M. O.; and Cebeci, T.: Numerical Solution of the Turbulent-Boundary-Layer Equations. Rep. No. DAC 33735 (Contract NOw 66-0324-c), Douglas Aircraft Co., Inc., May 29, 1967.

82. Keller, Herbert B.; and Cebeci, Tuncer: Accurate Numerical Methods for Boundary Layer Flows. II. Two-Dimensional Turbulent Flows. AIAA Paper No. 71-164, Jan. 1971.

83. Cebeci, Tuncer; Smith, A. M. O.; and Mosinkis, G.: Calculation of Compressible Adiabatic Turbulent Boundary Layers. AIAA Paper No. 69-687, June 1969.

84. Beckwith, Ivan E.; and Bushnell, Dennis M. (With appendix C by Carolyn C. Thomas): Detailed Description and Results of a Method for Computing Mean and Fluctuating Quantities in Turbulent Boundary Layers. NASA TN D-4815, 1968.

85. McLafferty, George H.; and Barber, Robert E.: Turbulent Boundary Layer Characteristics in Supersonic Streams Having Adverse Pressure Gradients. Rep. R-1285-11 (Contract No. NOa(s) 55-133-c), Res. Dep., United Aircraft Corp., Sept. 1959.

86. Moore, D. R.; and Harkness, J.: Experimental Investigation of the Compressible Turbulent Boundary Layer at Very High Reynolds Numbers, M = 2.8. Rep. No. 0-71000/4R-9, LTV Res. Center, Apr. 1964.

87. Coles, Donald: Measurements in the Boundary Layer on a Smooth Flat Plate in Supersonic Flow. Jet Propulsion Lab., California Inst. Technol. III. Measurements in a Flat-Plate Boundary Layer at the Jet Propulsion Laboratory. Rep. No. 20-71 (Contract No. DA-04-495-Ord 18), June 1, 1953.

88. Marvin, Joseph G.; and Akin, Clifford M.: Combined Effects of Mass Addition and Nose Bluntness of Boundary-Layer Transition. AIAA Paper No. 69-706, June 1969.

89. Marvin, Joseph G.; and Sheaffer, Yvonne S.: A Method for Solving the Nonsimilar Laminar Boundary-Layer Equations Including Foreign Gas Injection. NASA TN D-5516, 1969.

90. Clutter, Darwin W.; and Smith, A. M. O.: Solution of the General Boundary-Layer Equations for Compressible Laminar Flow, Including Transverse Curvature. Rep. No. LB 31088 (Contract NOw 60-0553c), Douglas Aircraft Co., Inc., Feb. 15, 1963.

91. Bushnell, Dennis M.; Jones, Robert A.; and Huffman, Jarrett K.: Heat-Transfer and Pressure Distributions on Spherically Blunted 25° Half-Angle Cone at Mach 8 and Angles of Attack up to 90°. NASA TN D-4792, 1968.

92. Lomax, Harvard; and Inouye, Mamoru: Numerical Analysis of Flow Properties About Blunt Bodies Moving at Supersonic Speeds in an Equilibrium Gas. NASA TR R-204, 1964.

93. Winter, K. G.; Rotta, J. C.; and Smith, K. G.: Untersuchungen der turbulenten Grenzschicht an einem taillierten Drehkörper bel Unter- und Überschallströmung, DLR FR 65-52, Nov. 1965.

94. Herring, H. James; and Mellor, George L.: A Method of Calculating Compressible Turbulent Boundary Layers. NASA CR-1144, 1968.

95. Sims, Joseph L.: Tables for Supersonic Flow Around Right Circular Cones at Zero Angle of Attack. NASA SP-3004, 1964.

96. O'Donnell, Robert M.: Experimental Investigation at a Mach Number of 2.41 of Average Skin-Friction Coefficients and Velocity Profiles for Laminar and Turbulent Boundary Layers and an Assessment of Probe Effects. NACA TN 3122, 1954.

97. Johnson, Charles B.: Pressure and Flow-Field Study at Mach Number 8 of Flow Separation on a Flat Plate With Deflected Trailing-Edge Flap. NASA TN D-4308, 1968.

**FIRST CLASS MAIL**

```
021 001 C1 U   12 710813 S00903DS
DEPT OF THE AIR FORCE
AF SYSTEMS COMMAND
AF WEAPONS LAB (WLOL)
ATTN: E LOU BOWMAN, CHIEF TECH LIBRARY
KIRTLAND AFB NM 87117
```

"The aeronautical and space activities of the United States shall be
conducted so as to contribute . . . to the expansion of human knowl-
edge of phenomena in the atmosphere and space. The Administration
shall provide for the widest practicable and appropriate dissemination
of information concerning its activities and the results thereof."

— NATIONAL AERONAUTICS AND SPACE ACT OF 1958

# NASA SCIENTIFIC AND TECHNICAL PUBLICATIONS

**TECHNICAL REPORTS:** Scientific and technical information considered important, complete, and a lasting contribution to existing knowledge.

**TECHNICAL NOTES:** Information less broad in scope but nevertheless of importance as a contribution to existing knowledge.

**TECHNICAL MEMORANDUMS:** Information receiving limited distribution because of preliminary data, security classification, or other reasons.

**CONTRACTOR REPORTS:** Scientific and technical information generated under a NASA contract or grant and considered an important contribution to existing knowledge.

**TECHNICAL TRANSLATIONS:** Information published in a foreign language considered to merit NASA distribution in English.

**SPECIAL PUBLICATIONS:** Information derived from or of value to NASA activities. Publications include conference proceedings, monographs, data compilations, handbooks, sourcebooks, and special bibliographies.

**TECHNOLOGY UTILIZATION PUBLICATIONS:** Information on technology used by NASA that may be of particular interest in commercial and other non-aerospace applications. Publications include Tech Briefs, Technology Utilization Reports and Technology Surveys.

*Details on the availability of these publications may be obtained from:*

## SCIENTIFIC AND TECHNICAL INFORMATION OFFICE

# NATIONAL AERONAUTICS AND SPACE ADMINISTRATION
### Washington, D.C. 20546